# Laboratory Study of the Effect of Sea Walls on Beach Erosion

by

Paul Markert Moody

S.B., Massachusetts Institute of Technology (1994)

Submitted to the Department of Civil and Environmental Engineering
in partial fulfillment of the requirements for the degree of

Master of Science in Civil and Environmental Engineering

at the

MASSACHUSETTS INSTITUTE OF TECHNOLOGY

February 1996



Author .....
Department of Civil and Environmental Engineering
October 16, 1995

Certified by .....
Ole S. Madsen
Professor of Civil and Environmental Engineering
Thesis Supervisor

Accepted by .....
Joseph M. Sussman
Chairman, Departmental Committee on Graduate Students

# Laboratory Study of the Effect of Sea Walls on Beach Erosion

by

Paul Markert Moody

Submitted to the Department of Civil and Environmental Engineering
on October 16, 1995, in partial fulfillment of the
requirements for the degree of
Master of Science in Civil and Environmental Engineering

## Abstract

This thesis presents the results of a laboratory study of beach erosion. The study compares the erosion and accretion on an unprotected dune beach with a beach protected with a rubble mound sea wall. There has been considerable debate in the coastal engineering community about the effects of sea walls on beaches. Accurate, controlled experiments are required to compare how sea walls and natural beaches interact with waves. This experiment was conducted in the J. Robert Gunther Family Ocean Wave Facility in the Parsons Laboratory at MIT. The experiment used a 4 meter wide by 11 meter long section of the basin. The beach is split in two sections, one with an unprotected dune and the other with a 1:1.5 sloping rubble mound sea wall. A probe that uses reflected light to measure the sand or water surface is used to measure the sand elevation. This is mounted on a square X-Y plotter capable of moving the probe anywhere within a 4 meter by 4 meter area. Using the probe on the X-Y plotter, the surface could be mapped out as a series of X, Y and Z values. The beaches were subjected to various normally incident spectral and monochromatic waves. The experiment was run iteratively, alternating waves and beach measurement to determine beach morphology as a function of time and wave condition.

The experiment showed remarkable agreement between the profiles of the natural beach and the beach protected by the sea wall over a wide range of wave conditions. For normally incident waves and all but the most extreme conditions, there was no significant difference in the behavior of unprotected and protected beaches seaward of the waterline. The beaches eroded and recovered to the same extent and at the same rate when subject to the same wave conditions. The experiments also demonstrated that spectral waves and changing water depths are important to accurately model beach behavior. This experiment did not look at the effects of non-normally incident waves and induced longshore currents. They are topics for further study.

Thesis Supervisor: Ole S. Madsen
Title: Professor of Civil and Environmental Engineering

# Acknowledgments

The research presented in this thesis was sponsored by the MIT Sea Grant College Program under grant numbers NA90AA-D-SG424 and NA46RG0434 from the Office of Sea Grant, National Oceanic and Atmospheric Administration, U. S. Department of Commerce, and by the AASERT Program under grant number DAAH04-93-G-0091 from the Department of Defense. The Sea Grant funding supported the author as a graduate student. The AASERT funding supported the author as an Undergraduate Research Opportunity (UROP) student, Susan Brown as a graduate student, Armen Vartanian as a UROP student and John Gambino as a UROP student during the course of the investigation. The Masatoyo Bed Profiler was provided by the Pittsburg Foundation under grant number R8683 through the generosity of Lewis W. Hicks III.

I would like to thank the U. S. Army Corps of Engineers for allowing me the opportunity to remain an extra year at MIT to pursue a Science Masters before fulfilling my service commitment.

I am especially grateful to my advisor, mentor and friend, Professor Ole Madsen. He saw potential in as an undergraduate and took me on first as a UROP and eventually as a graduate student. He continually pushed me to work harder and reach that potential. His classes were excellent while his advice and insight always helpful. I feel truly fortunate to have had the opportunity of working with him.

Additionally, I would like to thank other students I have worked with while in the lab. Susan Brown has been a good friend and research associate. She worked on the wavemaker calibration, wave generation and wave analysis and she helped run many of the initial experiments. Armen Vartanian was involved in the X-Y plotter construction and development. John Gambino helped run many of the later experiments and worked on software development. Hoang Tran taught me more about electronics, computers and software than I ever thought I would need to know to get an environmental engineering degree.

Many other people provided me with the support and assistance to successfully complete this project and the thesis. Jack Crocker was indispensable in the shop during the planning and construction of the X-Y plotter. Analia Barrantes-de Karma was very helpful getting me started in the lab and was always available for assistance and advice. Dr. Eng Soon

Chan's input into planning and running the experiment was very insightful. Mike Ernst, Peter Zeeb and Phil Trowbridge all helped me to understand my way around the shop and the electronics lab. Glenn Moglen and Lynn Reid helped me to understand LaTeX and athena. Additionally, I would like to thank all my friends who provided a distraction from the lab and my work in order to preserve my sanity and sense of humor.

Finally, I would like to thank my family for the many years of support that they have given me. I wish my father could have seen me graduate, I know he would be proud. I especially would like to thank my mother who has done so much for me over the years.

# Contents

# List of Figures

# List of Tables

# List of Variables

$A$ Integration constant.

$A_{bm}$ Wave excursion amplitude.

$a$ Wave amplitude.

$B$ Constant.

$b$ Wave amplitude, cm of wave maker motion per cm of wave amplitude.

$C$ Complex form of water surface, $\eta$.

$c$ Form speed for wave, $[L/T]$.

$c_g$ Wave celerity.

$d$ Wave gauge seperation length. Also sand grain diameter.

$E$ Variable proportional to wave energy, the wave spectrum, $[L^2T]$.

$E_p$ Potential energy.

$e$ Base of natural logarithm, ($\sim 2.71$).

$F_D$ Drag force.

$f_w$ Wave friction factor.

$g$ Acceleration due to gravity, $9.8m/s^2$.

$H$ Wave height, root mean square wave height for spectral waves. Also transfer function for wavemaker, $[V/cm]$.

$H_s$ Significant wave height, $\sqrt{2}H$.

$h$ Water depth.

$j$ Complex number, $\sqrt{-1}$.

$K_s$ Shoaling coefficient.

$k$ Wave number, $2\pi/L$.

$k_n$ Nikuradse equivalent sand grain roughness.

$L$ Wavelength.

$m$ Static paddle calibration for wave maker, $[cm/V]$.

$ns$ Number of samples during wave data analysis.

$P_{\eta\eta}$ Spectrum generated from wave data.

$p_\delta$ Fluid pressure at the outer edge of the wave boundary layer.

$R$ Reflection coefficient.

$S_{\eta\eta}$ Surface spectrum.

$S_\star$ Sediment-fluid parameter.

$s$ Relative sediment density, $\rho_s/\rho$.

$T$ Wave period.

$T_M$ Length of wave data record.

$t$ Time.

$u$ Velocity in the positve $x$ direction.

$u_\star$ Shear velocity, $\sqrt{\tau/\rho}$.

$V$ Voltage in Volts.

$W_b$ Submerged weight.

$w_f$ Sediment fall velocity.

$x$ Coordinate parallel to bottom, in the direction of wave propagation and in the cross-shore direction.

$y$ Coordinate parallel to bottom and in the longshore direction.

$z$ Coordinate normal to bottom, positive upwards.

## Greek variables:

$\alpha$ Phillips constant.

$\beta$ Suspended sediment concentration.

$\gamma$ Peak enhancement factor.

$\delta_w$ Thickness of wave boundary layer.

$\zeta$ Wave maker paddle position.

$\eta$ Surface profile, vertical distance from mean water level.

$\kappa$ von Karmen's constant, 0.4.

$\nu$ Kinematic viscosity of fluid, $10^{-6} m^2/s$ for seawater.

$\nu_t$ Turbulent eddy viscosity.

$\pi$ Mathematic constant, ($\sim 3.14$).

$\rho$ Fluid density.

$\sigma$ Spectral width factor.

$\tau$ Shear stress.

$\Phi$ Velocity potential for linear wave theory.

$\phi$ Phase angle.

$\varphi(\omega)$ Finite depth correction to JONSWAP sepctrum.

$\chi$ Component of the finite depth correction to JONSWAP spectrum.

$\psi$ Shields parameter.

$\omega$ Radian frequency, $2\pi f$.

## Subscripts and special notation:

$(\,)_b$ Bottom condition.

$(\,)_{cr}$ Critical condition.

$(\,)_{eq}$ Equivalent, pertaining to spectral waves.

$(\,)_i$ Incident.

$(\,)_{inp}$ Input.

$(\,)_J$ Related to the JONSWAP spectrum.

$(\,)_{mes}$ Measured.

$(\,)_{nom}$ Nominal condition.

$(\,)_{PM}$ Related to the Pierson-Moskowitz spectrum.

$(\,)_p$ Peak quantity.

$(\,)_r$ Reflected.

$(\,)_s$ Sediment.

$(\,)_w$ Wave condition.

$(\,)_{wm}$ Maximum wave condition.

$(\,)_0$ Deep water condition.

$\bar{a}$ Overbar signifies average or steady state of $a$.

$\tilde{a}$ Nomdimensional $a$ or time varient $a$.

$|a|$ Magnitude of $a$.

$f(a)$ A function of $a$.

### Nondimensional Numbers

$D_0 = H_0/d$, parameter introduced by Iwagaki and Noda (1962).

$Fr = w_f/\sqrt{gH_0}$, Sediment parameter in the form of a Froude number.

$G_0 = \pi w_f/gT$, parameter introduced by Dean (1973).

$N_0 = H_0/w_f T$, Dean number or fall speed parameter.

$P_0 = \frac{gH_0^2}{w_f{}^3 T}$, profile parameter.

$Re = lu/\nu$, Reynolds number.

$S_0 = H_0/L_0$, wave steepness.

# Chapter 1

# Introduction

The extensive development and even over-development of coastal areas has created controversy in coastal zone management. Coastal property owners seek to protect their property and possessions from storm induced erosion by building sea walls, revetments, off shore breakwaters or other engineering means used to protect the shoreline. As a result, large parts of the shoreline, especially on the heavily developed East Coast are armored against storm wave attacks. The public agencies that regulate shore protection often have inconsistent or outdated criteria for permitting shore protection, therefore regulations need to be updated and improved. Since the regulations are based on coastal science and engineering which are not fully understood, there needs to be more research into wave and beach interaction.

Coastal erosion in an area can be the result of increased sea levels, a reduced sediment supply, the influence from other coastal structures, a change in local wave and current conditions or an increase in storm frequency and severity. Whatever the cause of coastal erosion, one thing remains constant. When people see that their house is in danger of washing away during a big storm, they fight to protect their property, with the use of various coastal protective structures. The Shore Protection Manual (1984) contains detailed discussion on the causes of beach erosion and various forms of engineering response. Controversy arises when other groups, which see beach protection as a problem related to over-development, fight to keep the beaches in their natural state.

When coastal resources are threatened, there are three main courses of action that can be taken. The shoreline can be armored which involves protecting the shore with

sea walls, groins, revetments, offshore breakwaters or a combination of those protective structures. The beaches can be nourished with sand to resupply what is eroded away. The third option is retreat, which involves scaling development back from the shoreline. There are many factors which go into deciding which option is employed for a given area. Local regulations, politics, economics and engineering feasibility all contribute to the final decision. Unfortunately, coastal engineering is a complex field with many questions that remain unanswered. The coastal engineering community has some ability to predict beach response to a structure based on field experience and laboratory studies, but in general it can be very difficult to predict how the immediate and adjacent beaches will respond to coastal structures. The coastal zone is the net result of many different physical processes at many different scales and is sensitive to perturbations. The interactions are poorly understood so it is difficult to say with any certainty how a structure will affect a given beach. Since understanding the physics and engineering is necessary for making informed decisions, it is important that the interactions between waves, beaches and coastal structures are better understood.

This investigation focuses on the interaction between sea walls and beaches in order to qualify sea wall and beach interaction. Due to scale problems involved with small-scale laboratory studies, this study does not claim to provide definitive quantitative conclusions. Sea walls have been a successful means of armoring the shore for many years. Sea walls are built to protect buildings and resources from beach erosion or inundation during a storm, they are not built to protect beaches. They are often placed on beaches that have a net erosion or on beaches that have a seasonal sand migration large enough to threaten buildings or other permanent resources. As more shoreline property is developed for private and commercial use, there is an increasing pressure to protect the beaches, and hence an increasing requirement for a better understanding of the mechanics of beach and sea wall interaction.

With so much interest in coastal structures, there has been much research in the field of sea walls recently. Nick Kraus has written several comprehensive reviews of the research into sea walls and their interaction with beaches. Kraus (1987) is a complete review of the relevant literature and research through 1987. The paper looks at the relevant laboratory and field investigations as well as reviews theoretical and conceptual work.

Kraus (1988) extends the review from 1987 and offers a more thorough look into several

of the past studies. The paper looks a little more in depth at coastal zone management in terms of strategies for management and interactions between beaches and coastal structures. He makes several key conclusions which have directed the focus of recent research. He considers whether sea walls accelerate or enhance erosion and considers data from field monitoring studies as well as data from laboratory studies at several scales. It is difficult to separate "passive erosion", or erosion on a net eroding shoreline that would have occurred without the structure, and "active erosion", or excess erosion in response to the structure, as defined later by Griggs et. al (1991), which makes it difficult to quantify the sea wall's effect on the beach. By looking at beach response on a protected and unprotected beach subject to the same wave conditions, we hope to be able to distinguish how much of a factor active erosion is.

Kraus is able to say that beaches with sea walls behave similarly to beaches without sea walls when there is a sufficiently wide surf zone and an adequate sediment supply. There is evidence of "flanking", which is increased local erosion at the edges of a sea wall. Flanking, when it appears, is usually proportional to the length of the sea wall. According to the available data, protected and unprotected beaches have similar recovery patterns when there is a sufficient sediment supply and accretional conditions. Kraus (1988) also says that the evidence available suggests that "softer" sea walls, with lower reflection coefficients due to greater permeability and gentler slopes, are better in that they prevent local scour and allow the beaches to recover faster.

The most recent review is Kraus and McDougal (1995) which provides comprehensive coverage of the research since the 1988 review. They question the validity of small-scale physical model tests, where small-scale is defined as using fine or very find sand with wave heights of less than 15 cm, due to the scale distortion extrapolating to prototype conditions. They allow that small scale laboratory studies can be useful, but one should be careful when interpreting the results.

They find the key parameter in sea wall and beach interaction is the location of the sea wall relative to the shoreline. As the sea wall is set further from the shoreline, the behavior is more like the behavior of a natural beach. Overall, they find throughout the studies that erosion is not increased in front of sea walls or revetments. The data examined supports Dean's "approximate principle" (Dean, 1986) which states,

> In a two-dimensional situation in nature with wave and sediment conditions

> conducive to formation of a longshore bar, the additional volumetric scour immediately fronting the armoring will be less than or equal to that volume that would have been provided through erosion by that portion of the profile upland of the armoring if that armoring were not present.

This principle has been verified in the field and in the laboratory. There are a few cases which seem to provide an exception to this principle, with the exceptions being attributed to significant longshore transport, which violates the assumption of two dimensional conditions. According to this principle, the beach in front of the sea wall could potentially erode as much as the dune so that there could be significant scour in front of the sea wall for the more extensive erosion events. We looked into this behavior during the experiment.

There have been several important field monitoring programs that have yielded important results. Griggs et. al (1990) present their results from four years of beach monitoring in Monterey Bay, CA. The monitoring sites include unprotected beaches, beaches with sea walls and beaches with riprap revetments. Their measurements demonstrate that there is a very similar response from protected and unprotected beaches during both erosion and recovery. Tait and Griggs (1990) show that the method of erosion is parallel retreat for beaches with or without a sea wall resulting in general profile deflation, with very similar results for protected and unprotected beaches. There is evidence of significant flanking, downdrift erosion due to longshore transport. They state that the downdrift erosion is due to the impoundment of sand behind sea walls. Constructing a sea wall results in a permanent removal of sand from the beach system. If there is insufficient sand in front of the sea wall, there will be a deficit in the longshore sand transport downdrift from the sea wall resulting in the flanking pattern seen. If the sea wall projects far enough into the surf zone, then it can even begin to act as a groin by blocking longshore transport and trapping sand updrift from the structure. They find that the sea wall position is an important parameter determining beach response. In their study, the sea wall protruding farthest into the surf zone was the first to lose its beach during storms, experienced the most scour and was the last to recover. They recommend that sea walls be built as far landward as feasible so that they only interact with waves during the largest storms.

McDougal et. al (1987) combine the results from a field monitoring program with laboratory studies to help determine beach response. Their study is motivated by the Oregon State Parks Division, which reviews sea wall permit applications. The most frequent con-

cerns are what the impact on adjacent unprotected beaches will be and how the sediment supply to the beaches will be affected. They find that the cross shore sand transport is very similar between protected and unprotected beaches. In regions with significant longshore transport, they observed significant downdrift erosion for up to 70% of the sea wall length, which indicates a large potential impact on adjacent unprotected beaches.

This study looks at the beach and sea wall interaction using normally incident irregular waves in a small-scale experiment. The first experiments look at beach response for an unprotected and a protected beach subjected to the same erosional and accretional conditions while separated by a dividing wall to isolate the cross shore transport. The last experiments continue to use normally incident irregular waves, but with the dividing wall removed so that the beaches can interact.

The second chapter explains the relevant theory for the experiments. In the section on wave theory, linear wave theory is presented and developed to include spectral waves, wave reflection and wave shoaling. The basic equations governing sediment transport are outlined followed by a summary of several erosion-accretion predictors. Finally, the parameters relating experimental scaling are presented. The third chapter presents the experimental setup, starting with the overall wave basin configuration. The beach measurement system, consisting of a large X-Y plotter and a beach profiling device, is described in detail. Wave generation and measurement are also covered in this chapter.

The fourth chapter contains a selection of the experimental results. The existence of a repeatable equilibrium profile generated by accretional waves is discussed. The equilibrium profile is used throughout the chapter because it provides a consistent reference profile. The equilibrium profile is a repeatable profile generated by standard accretional waves used during the experiment. After severe erosion the equilibrium profile may shift shoreward, but the shape remains the same. Some experiments were conducted to look at the difference in beach response for regular and irregular waves, with irregular waves producing smoother beaches with less influence from non-linear effects such as circulation currents in the experimental section. The erosion and accretion predictors presented in Chapter 3 were used to examine the erosion and accretion criteria for this experiment. It was found that the scale distortion was large enough that several predictors differed from the published values by an order of magnitude. An experiment with a small simulated storm surge was conducted with the beaches separated by a dividing wall. After the dividing wall was removed,

the sea wall and dune beach interaction was studied. Interaction was examined using limited, extensive and storm surge erosion and accretion wave sequences. The conclusions and recommendations for further research are presented in Chapter 5.

Two appendices are provided for further documentation of the X-Y plotter, constructed in the lab for use in this experiment. Appendix A presents the design and construction of the plotter system while Appendix B is essentially a users manual for operation and trouble-shooting when using the plotter.

# Chapter 2

# Summary of Basic Theory

## 2.1 Wave Theory

Since this study is about wave and sediment interaction at coastal structures, we need to look at wave theory. The linearized governing equations for fluid motion are a good starting point in wave theory and analysis. Good references for linear wave theory are Kinsman (1965), Whithan (1974) or Mei (1989). Linearizing the governing equations involves some approximations that do not hold for very steep waves or for breaking waves, but the results gained from linear theory are quite useful. The linearized governing equations can be expressed in terms of a velocity potential, $\Phi$, as

$$\nabla^2\Phi = \frac{\delta^2\Phi}{\delta x^2} + \frac{\delta^2\Phi}{\delta z^2} = 0 \qquad \text{in fluid} \tag{2.1}$$

$$\frac{\delta\Phi}{\delta z} = 0 \qquad \text{at the bottom, } z = -h \tag{2.2}$$

$$\frac{\delta^2\Phi}{\delta t^2} + g\frac{\delta\Phi}{\delta z} = 0 \qquad \text{at the surface, } z = 0 \tag{2.3}$$

where $x$ is the horizontal direction, $z$ is the vertical direction with the origin at the mean water level, $h$ is the water depth, $g$ is the acceleration due to gravity and $t$ is time. The physical coordinates are shown in Figure 2-1.

A solution of the linearized governing equation corresponding to a periodic progressive wave of permanent form can be expressed as

$$\Phi = A\cosh k(z+h)\sin(kx - \omega t) \tag{2.4}$$

where $A$ is a constant and $k$ is the wave number. The wave varies sinusoidally with a wave length of $L$ and a radian frequency of $\omega$. The wave number is related to the wavelength, $L$ by $k = 2\pi/L$. The wave number is obtained through the dispersion relationship given by

$$\omega^2 = gk \tanh(kh) \tag{2.5}$$

The surface profile, $\eta$, is obtained from

$$\eta = -\frac{1}{g}(\frac{\delta\Phi}{\delta t})_{z=0} = \frac{A\omega}{g} \cosh kh \cos(kx - \omega t) \tag{2.6}$$

Since the wave amplitude, $a$, is usually specified, the surface profile is usually expressed as

$$\eta = a \cos(kx - \omega t) \tag{2.7}$$

From here, we can solve for the the velocity potential of a linear progressive wave as

$$\Phi = \frac{ag}{\omega} \frac{\cosh k(z+h)}{\cosh kh} \sin(kx - \omega t) \tag{2.8}$$

One of the advantages of using linear wave theory is the principle of wave superposition. It is very useful in both the generation and analysis of multi-component wave forms. Since the governing equations are linear, any linear combination of two solutions, $\Phi_1$ and $\Phi_2$, is also a solution as shown by

$$\Phi = A_1\Phi_1 + A_2\Phi_2 \tag{2.9}$$

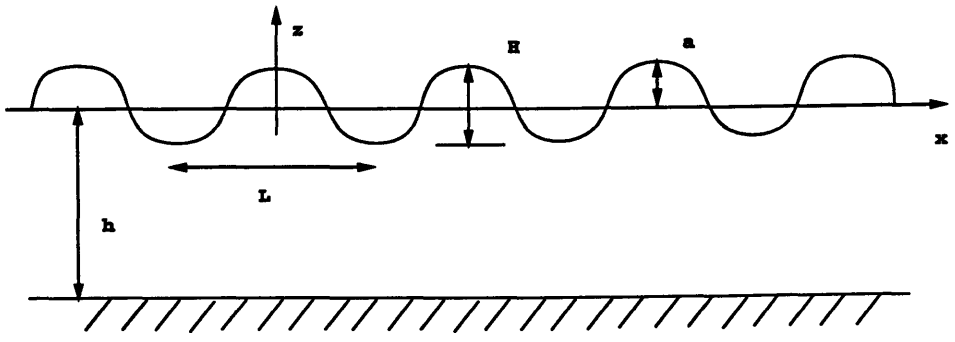


Figure 2-1: Physical Coordinates and Dimensions for Waves

By extension, it can be readily seen that the surface profile, $\eta$, is the same linear combination of component surface profiles

$$\eta = A_1\eta_1 + A_2\eta_2 \tag{2.10}$$

This result leads to spectral waves.

### 2.1.1 Spectral Waves

Linear theory leads to the principle of superposition. Superposition says that any linear combination of wave solutions is itself a solution to the governing equations. A motion consisting of $n$ contributions from $n$ frequencies can be represented by

$$\eta = \sum_{i=1}^{n} a_i \cos(\omega_i t + \phi_i) \tag{2.11}$$

where $\phi_i$ is the phase associated with the $i$th component. The potential energy, $E_P$, is given by

$$E_P = \frac{1}{2}\rho g\overline{\eta^2} = \frac{1}{2}\rho g \sum_{i=1}^{n} \frac{1}{2}{a_i}^2 \tag{2.12}$$

where $\overline{\eta^2}$ is the variance of the surface variation and $\rho$ is the fluid density. Assuming the total energy is equally divided between the potential energy and kinetic energy from linear wave theory, the total energy, $E_S$ is twice the potential energy. Since $\rho g$ is constant, this can be simplified further to define a variable proportional to wave energy with units of $[L^2T]$ called $E$ and defined by

$$E = \overline{\eta^2} = \sum_{i=1}^{n} \frac{1}{2}{a_i}^2 \tag{2.13}$$

The wave spectrum, $S_{\eta\eta}(\omega)$, is a continuous function of $\omega$ defined such that

$$\frac{1}{2}{a_n}^2 = S_{\eta\eta}(\omega_n)\Delta\omega \tag{2.14}$$

The spectrum represents the distribution of wave energy within radian frequency space. Letting $\Delta\omega \to 0$, we obtain a continuous distribution of wave energy in radian frequency space

$$E = \int_0^\infty S_{\eta\eta}(\omega)\delta\omega \tag{2.15}$$

With the definition of the spectrum in hand, we can now do two important things. We

can, given wave measurements, obtain a spectrum and, given a spectrum, produce spectral waves.

A convenient way to express a spectral wave condition is stating the equivalent monochromatic wave conditions in terms of an equivalent period and amplitude. The equivalent amplitude is the amplitude of a simple periodic wave with the same total wave energy as the spectral wave. It is given by

$$a_{eq} = \sqrt{\int_0^\infty 2S_{\eta\eta}(\omega)\delta\omega} \tag{2.16}$$

The equivalent radian frequency is given by the weighted average of the spectrum as given by

$$\omega_{eq} = \frac{\int_0^\infty \omega S_{\eta\eta}\delta\omega}{\int_0^\infty S_{\eta\eta}\delta\omega} \tag{2.17}$$

Then the equivalent period, $T_{eq}$, is given by

$$T_{eq} = 2\pi/\omega_{eq} \tag{2.18}$$

### Spectral Wave Analysis

Spectral wave analysis starts with a discrete wave record of finite length, $T_M$. Assuming the signal is periodic with period $T_M$, we can take the Fourier series representation of $\eta(t)$

$$\eta(t) = A_0 + \sum_{n=1}^{\infty} A_n \cos(\frac{2\pi n}{T_M}t) + \sum_{n=1}^{\infty} B_n \sin(\frac{2\pi n}{T_M}t) \tag{2.19}$$

where

$$A_0 = \frac{1}{T_M}\int_0^{T_M} \eta(t)\delta t \tag{2.20}$$

$$A_n = \frac{2}{T_M}\int_0^{T_M} \eta(t)\cos(\frac{2\pi n}{T_M}t)\delta t \tag{2.21}$$

$$B_n = \frac{2}{T_M}\int_0^{T_M} \eta(t)\sin(\frac{2\pi n}{T_M}t)\delta t \tag{2.22}$$

Since we only know $\eta$ at discrete times, we cannot calculate infinitely many unknown amplitudes.

With a sampling interval of $\Delta t$, there will be $2N+1$ measurements where $T_M = 2N\Delta t$

and (2.19) becomes

$$\eta(t) = A_0 + \sum_{n=1}^{N} A_n \cos(\frac{2\pi n}{T_M} t) + \sum_{n=1}^{N} B_n \sin(\frac{2\pi n}{T_M} t) \tag{2.23}$$

where $A_n$ and $B_n$ are now defined as

$$A_0 = \frac{1}{2N} \sum_{i=0}^{2N} \eta_i = \overline{\eta} \equiv 0 \tag{2.24}$$

$$A_n = \frac{1}{N} \sum_{i=0}^{2N} \eta_i \cos(\frac{\pi n}{N} i) \tag{2.25}$$

$$B_n = \frac{1}{N} \sum_{i=0}^{2N} \eta_i \sin(\frac{\pi n}{N} i) \tag{2.26}$$

The highest frequency that can be resolved is the Nyquist Frequency, $f_{max} = 1/(2\Delta t)$ and the lowest frequency is $f_{min} = 1/T_M$. Then the spectrum, $S_{\eta\eta}$, is given by

$$S_{\eta\eta}(\omega_n) = \frac{\frac{1}{2}({A_n}^2 + {B_n}^2)}{\Delta\omega} \tag{2.27}$$

where $\Delta\omega = 2\pi/T_M$, which is the frequency increment.

Alternatively, the spectrum could be represented as a cosine series with a phase component

$$\eta = \sum_{n=1}^{N} \sqrt{({A_n}^2 + {B_n}^2)} \cos(\frac{2\pi n}{T_M} t - \phi_n) \tag{2.28}$$

where the phase, $\phi_n$ is given by

$$\tan\phi_n = \frac{B_n}{A_n} \tag{2.29}$$

Section 3.5.2 contains more detail about how spectral analysis is used in this experiment.

### Spectral Wave Generation

The spectrum can be broken down into a discrete number of frequency intervals with a wave component from each interval. Using this method, the free surface equation becomes

$$\eta(t) = \sum_{i=1}^{n} \sqrt{2 S_{\eta\eta}(\omega_i)\Delta\omega} \cos(\omega_i t + \phi_i) \tag{2.30}$$

where $\phi_i$ is the phase associated with component $i$ and is randomly and uniformly distributed between 0 and $2\pi$. There are several ways to divide the spectrum including dividing it with a constant frequency interval or dividing it so that the energy per interval is constant. Since amplitude is proportional to the square root of the energy, intervals with equal energy would create components with equal amplitudes.

### 2.1.2 Pierson-Moskowitz and JONSWAP Spectra

Pierson and Moskowitz (1964) studied spectral waves and empirically determined the spectrum, $E_{PM}$, defined by:

$$E_{PM}(\omega) = \frac{2\pi\alpha g^2}{\omega^5} \exp\{-\frac{5}{4}(\frac{\omega_p}{\omega})^4\} \tag{2.31}$$

where $\alpha$ is the Phillips constant and $\omega_p$ is the peak frequency. Following their work, Hasselman et al. (1973) performed an extensive study of wind generated waves in the North Sea. The project was known as the Joint North Sea Wave Project, or JONSWAP. They measured the wave spectra of wind waves and determined the JONSWAP spectrum, $E_J$. This is defined as:

$$E_J(\omega) = \frac{2\pi\alpha g^2}{\omega^5} \exp\{-\frac{5}{4}(\frac{\omega_p}{\omega})^4\}\gamma^{\exp\{-\frac{[\omega/\omega_p-1]^2}{2\sigma^2}\}} \tag{2.32}$$

where $\gamma$ is the peak enhancement factor and $\sigma$ is the spectral width factor. The JONSWAP spectrum is really the Pierson-Moskowitz spectrum multiplied by a peak enhancement factor:

$$E_J = E_{PM}\gamma^{\exp\{-\frac{[\omega/\omega_p-1]^2}{2\sigma^2}\}} \tag{2.33}$$

The spectral width factor, $\sigma$ is defined as:

$$\sigma = \begin{cases} \sigma_a & \text{for } \omega \leq \omega_p, \\ \sigma_b & \text{for } \omega > \omega_p \end{cases} \tag{2.34}$$

so that there are five free parameters defining the JONSWAP spectrum: $\omega_p$, $\alpha$, $\gamma$, $\sigma_a$ and $\sigma_b$.

Hasselmann et al. (1973) fitted the parameters to wind generated, deep water, spectral waves. They found that both $\omega_p$ and $\alpha$ were functions of the nondimensional fetch, $\tilde{x} = gx/u_\star^2$, where x is the (dimensional) fetch and $u_\star$ is the wind friction velocity. The peak

frequency is given by

$$\omega_p = \frac{3.5}{2\pi}\tilde{x}^{-0.33} \tag{2.35}$$

and the Phillips parameter is given by

$$\alpha = 0.076\tilde{x}^{-0.22} \tag{2.36}$$

Hasselmann fit the peak enhancement parameters to the values of $\gamma = 3.3$, $\sigma_a = 0.07$ and $\sigma_b = 0.09$ as a first approximation.

Since not all waves are deep water, Kitaigorodskii (1975) determined a finite depth correction, $\varphi(\omega)$, to the spectrum:

$$S_{\eta\eta}(\omega) = \varphi(\omega)E_J(\omega) \tag{2.37}$$

where $\varphi$ is the finite depth correction obtained from:

$$\varphi(\omega) = \chi^{-2}[1 + \omega_h^2(\chi^2 - 1)]^{-1} \tag{2.38}$$

For this equation, $\omega_h$ is defined as

$$\omega_h = \omega\sqrt{\frac{h}{g}} \tag{2.39}$$

and $\chi$ is obtained from

$$\chi \tanh \omega_h^2 \chi = 1 \tag{2.40}$$

Mathisen and Madsen (1993) use the values $\alpha = 0.0015$, $\gamma = 3.3$ and $\sigma_a = \sigma_b = 0.08$. The peak frequency, $\omega_p$, is dependent on the representative wave frequency. They select the parameters such that the spectral wave is equivalent to a 6 cm amplitude monochromatic wave with a frequency of 2.39 rad/sec in 60 cm water depth. A single value for $\sigma$ is used as a simplification. $\alpha$ is a scaling factor controlling the amount of energy present in the wave but not the shape of the spectrum. More details on the generation of spectral waves are given in Section 3.4.3.

### 2.1.3 Wave Reflection

The preceding sections have considered linear progressive waves, without any consideration of wave propagation direction. Wave basin or flume experiments typically have a wave paddle at one end and some form of beach to absorb the wave energy at the other. Some percentage of the energy of the incident wave will be reflected and the remainder will form the reflected wave. If the incident wave has an amplitude $a_i$ and the reflected wave has an amplitude $a_r$, then the reflection coefficient, $R$, is defined as

$$R = \frac{a_r}{a_i} \tag{2.41}$$

To measure this reflection coefficient and determine what the actual incident wave amplitude is, a minimum of two wave gauges are required.

The wave data from the two wave gauges can be referred to as $\eta_1$ and $\eta_2$. Looking at frequency $\omega$ with associated wave number $k$, the wave data at the wave gauges will be

$$\eta_1 = a_i \cos(-\omega t + \phi_i) + a_r \cos(-\omega t + \phi_r) \tag{2.42}$$

$$\eta_2 = a_i \cos(kd - \omega t + \phi_i) + a_r \cos(-kd - \omega t + \phi_r) \tag{2.43}$$

with the first gauge being taken as the origin of the $x$ axis and the wave gauges separated by a distance $d$. In complex notation, the wave gauge data is the real part of

$$C_1 = a_i e^{j(-\omega t + \phi_i)} + a_r e^{j(-\omega t + \phi_r)} \tag{2.44}$$

$$C_2 = a_i e^{j(kd - \omega t + \phi_i)} + a_r e^{j(-kd - \omega t + \phi_r)} \tag{2.45}$$

where $j = \sqrt{-1}$. This can be simplified with the following identities

$$C_i = a_i e^{j(-\omega t + \phi_i)} \tag{2.46}$$

$$C_r = a_r e^{j(-\omega t + \phi_r)} \tag{2.47}$$

The complex form of the wave gauge data becomes

$$C_1 = C_i + C_r \tag{2.48}$$

$$C_2 = C_i e^{jkd} + C_r e^{-jkd} \tag{2.49}$$

Solving for $C_i$ and $C_r$ with a little algebraic manipulation yields

$$C_i = \frac{C_2 - C_1 e^{-jkd}}{e^{jkd} - e^{-jkd}} \tag{2.50}$$

$$C_r = \frac{-C_2 + C_1 e^{jkd}}{e^{jkd} - e^{-jkd}} \tag{2.51}$$

The incident and reflected wave amplitudes are equivalent to the magnitude of their complex forms

$$a_i = |C_i| \tag{2.52}$$

$$a_r = |C_r| \tag{2.53}$$

This method of determining the incident and reflected wave amplitudes does not work when $kd = n\pi$ where $n$ is an integer as shown in (2.51). The specifics of the wave analysis for this experiment are expanded upon in Section 3.5.2

### 2.1.4 Wave Shoaling

Any form of measurement needs a reference condition or state, including wave measurements. The reference condition for wave measurements and for erosion criteria is the deep water condition. In deep water, the depth is great enough that the wave does not "feel" the bottom, or the wave-induced velocity in the vicinity of the bottom is zero. By the conservation of wave principle, the radian frequency for a shoaling wave remains constant while the wave height and wave length vary with changes in depth.

The shoaling coefficient is obtained by looking at the energy flux between two stations, one in deep water and the other in shallow. Neglecting bottom friction and wave reflection, the energy flux will remain constant. With $a$ as the wave amplitude and $c_g$ as the group velocity, the energy flux balance for the two stations is

$$\frac{1}{2}\rho g a_1^2 c_{g,1} = \frac{1}{2}\rho g a_2^2 c_{g,2} \tag{2.54}$$

this can be rearranged to yield

$$\frac{a_2}{a_1} = \sqrt{\frac{c_{g,1}}{c_{g,2}}} \tag{2.55}$$

For deep water, $c_{g,1} = \frac{1}{2}c_0$ so the wave height is given as

$$\frac{H}{H_O} = \sqrt{\frac{c_0}{2c_g}} = K_s \tag{2.56}$$

where $K_s$ is the shoaling coefficient. $c_g$ is a function of $h/L$ where $L$ is the wavelength and $h$ is the depth, so it is also a function of $h/L_0$ where $L_0$ is the deep water wavelength.

The deep water wavelength is given by $L_0 = T^2 g/2\pi$ where $T$ is the period. Using the wave table for sinusoidal waves developed by Skovgaard et al. (1974), one can determine the wavelength, amplitude, celerity and other useful factors as a function of $h/L_0$.

## 2.2 Sediment and Wave Interaction

Beach erosion and accretion are examples of sediment and wave interaction on the large scale. This section is designed to look at the interaction on the smaller scale.

### 2.2.1 Initiation of Motion, Force Considerations

Sand grain motion occurs when the forces that are attempting to move the particle exceed the forces that hold the particle in place. These forces are complex and poorly understood so there is no way to obtain a good theoretical initiation of motion criteria. A simple force balance on the particle does determine the appropriate nondimensional parameters to look for in an empirical study of the initiation of motion.

The force attempting to dislodge the particle, $F_D$, is proportional to the bottom shear stress, $\tau_b$, and acts on the cross section of the particle which is proportional to $d^2$ where $d$ is the particle diameter.

$$F_D \propto \tau_b d^2 \tag{2.57}$$

The force holding the particle in place is the submerged weight, $W_b$ of the particle. This force is given by

$$W_b \propto (\rho_s - \rho) g d^3 = (s-1)\rho g d^3 \tag{2.58}$$

where $\rho_s$ is the sediment density, $\rho$ is the fluid density and $s = \rho_s/\rho$ is density of sediment relative to water. Since the initiation of motion involves the dislodging force overcoming the stabilizing force, the ratio of these forces provides an indicator of stability called the

Shields parameter (Shields 1936), $\psi$. It is defined as

$$\psi = \frac{\tau_b}{\rho(s-1)gd} = \frac{u_*^2}{(s-1)gd} \tag{2.59}$$

where $u_* = \sqrt{\tau_b/\rho}$ is the shear velocity.

The parameter that determines the near-bottom flow conditions is the boundary Reynolds number, $Re_*$, defined as

$$Re_* = \frac{u_* k_n}{\nu} \tag{2.60}$$

where $k_n$ is the equivalent Nikuradse sand grain roughness and $\nu$ is the kinematic fluid viscosity ($\nu \approx 10^{-6}$ m$^2$/s for seawater). For turbulent flow over a flat bed, the Nikuradse sand grain roughness will be the sediment diameter, $k_n = d$. For a given flow condition, there will be a critical Shields parameter value, $\psi_{cr}$, where motion is incipient.

$$\psi_{cr} = \frac{u_{*cr}^2}{(s-1)gd} = f(Re_*) \tag{2.61}$$

For values of $\psi > \psi_{cr}$ sediment motion occurs. The critical Shields parameter has been experimentally determined as a function of the boundary Reynolds number, e. g. Shields (1936) for pure current and Madsen and Grant (1976) for pure waves.

Since the shear velocity is in both parameters, determining the critical flow conditions for a particular sediment is cumbersome. This problem is avoided if a new parameter, the sediment-fluid parameter, $S_*$ is used. It is defined as

$$S_* = \frac{d}{4\nu}\sqrt{(s-1)gd} = \frac{Re_*}{4\sqrt{\psi_{cr}}} \tag{2.62}$$

The sediment-fluid parameter is determined from sediment and fluid properties and is independent of the fluid flow. The critical Shields parameter is a function of the sediment-fluid parameter and the dependence is given in Madsen and Grant (1976).

The sediment fall velocity, $w_f$ is also found to be a function of the sediment-fluid parameter. This is easily seen since the fall velocity is a force balance between the submerged weight and the drag force acting on a freely falling particle. The non-dimensional fall velocity is

$$\frac{w_f}{\sqrt{(s-1)gd}} = f(S_*) \tag{2.63}$$

The empirical relation is given in Madsen and Grant (1976).

### 2.2.2 Sediment-Wave Interaction

We now know the initiation of motion conditions in terms of a shear velocity, $u_\star$, but want to be able to determine the initiation of motion criteria for a given wave form. The procedure is documented in more detail in Madsen and Wikramanayake (1991).

The linearized boundary layer equation can be written as

$$\rho\frac{\delta u}{\delta t} = -\frac{\delta p_\delta}{\delta x} + \frac{\delta \tau}{\delta z} \tag{2.64}$$

where $x$ is the horizontal direction, $z$ is the vertical coordinate chosen to be zero at the bottom and positive upwards, $\rho$ is the fluid density, $\tau$ is the shear stress, $t$ is time, $u$ is the horizontal velocity and $p_\delta$ is the pressure at the outer edge of the boundary layer. In the case of waves, the oscillating bottom flow causes the boundary layer thickness, $\delta_w$, to remain small so the outer edge of the boundary layer may be predicted by linear wave theory. In this case, the shear stress vanishes and the linearized boundary layer equation becomes

$$-\frac{\delta p_\delta}{\delta x} = \rho\frac{\delta u_b}{\delta t} \tag{2.65}$$

where $u_b$ is the horizontal velocity predicted by linear wave theory. The boundary layer equation can be written as

$$\frac{\delta(u_w - u_b)}{\delta t} = \frac{\delta}{\delta z}[\frac{\tau_w}{\rho}] \tag{2.66}$$

where $u_w$ is the horizontal velocity in the boundary layer, $u_w = u_b$ at $z > \delta_w$ and $u_w = 0$ at $z = 0$.

Since the flow is unsteady, the shear stress will vary with time. The time-variant shear stress is given by $u_\star = \sqrt{|\tau_b|/\rho} = u_\star(t)$. A time-varying sheer velocity complicates the solution to the boundary layer equation but only has a small effect when compared to the solution obtained using a time-invariant model where $u_\star = u_{\star wm} = \sqrt{\tau_{wm}/\rho}$ based on the maximum bottom shear stress, $\tau_{wm}$ (Trowbridge and Madsen, 1984). Using the simple eddy viscosity model for turbulent flow, we obtain

$$\frac{\tau_w}{\rho} = \nu_t\frac{\delta u_w}{\delta z} = \kappa u_{\star wm} z\frac{\delta u_w}{\delta z} \tag{2.67}$$

where $\nu_t$ is the turbulent eddy viscosity and $\kappa = 0.4$ is von Karman's constant.

For a linear periodic wave, the near bottom velocity can be expressed as

$$u_b = u_{bm} \cos \omega t \tag{2.68}$$

where $u_{bm}$ is the maximum orbital velocity. The bottom excursion amplitude, a length scale of the bottom fluid motion, is given by

$$A_{bm} = \frac{u_{bm}}{\omega} = \frac{H/2}{\sinh(2\pi h/L)} \tag{2.69}$$

where h is the water depth. For simple periodic waves, $H$ is the wave height, $\omega$ is the radian frequency and $L$ is the wavelength. Madsen (1994) shows that the theory for simple periodic waves can be extended to spectral waves if the equivalent periodic wave conditions are used.

The bottom shear stress and the maximum bottom orbital velocity are related through the wave friction factor, $f_w$ defined by Jonsson (1966) as

$$\tau_{wm} = \frac{1}{2} f_w \rho u_{bm}^2 \tag{2.70}$$

or equivalently as

$$u_{*wm} = \sqrt{f_w/2}\, u_{bm} \tag{2.71}$$

For rough turbulent flow, the wave friction factor is a function of the ratio of bottom excursion amplitude to the Nikuradse equivalent sand grain roughness

$$f_w = f(\frac{A_{bm}}{k_n}) \tag{2.72}$$

For smooth turbulent flow, the wave friction factor is given as a function of the wave Reynolds number

$$f_w = f(RE) = f(\frac{u_{bm} A_{bm}}{\nu}) \tag{2.73}$$

It is beyond the scope of this text to solve the friction factor equations, a more complete solution is given in Madsen and Wikramanayke (1991).

## 2.3 Erosion and Accretion Criteria

There have been many attempts to determine simple methods of predicting beach erosion and accretion. Laboratory studies which determine good laboratory criteria do not necessarily scale to prototype beaches while prototype studies are uncontrolled and are subject to greater measurement error. Also, the criteria predict erosion or accretion but are unable to predict how much a beach will erode or accrete under a given condition. Several proposed criteria are presented here. The criteria are presented as equations, but they are really inequalities separating regions of erosion and accretion.

Kraus et al. (1991) evaluated several parameters for predictive capabilities and compared criteria based on laboratory experiments in large wave tanks with criteria from beach data from around the world. The large wave tank criteria correspond to natural beach criteria when the root mean square, or equivalent, wave height is used. The criteria examined by Kraus et al. (1991) are based on five nondimensional parameters:

$D_0 = H_0/d$, a parameter defined by Iwagaki and Noda (1962).

$G_0 = \pi w_f/gT$, a parameter defined by Dean (1973).

$N_0 = H_0/w_f T$, the fall speed parameter or the Dean number.

$S_0 = H_0/L_0$, the wave steepness.

$F_0 = w_f/\sqrt{gH_0}$, a Froude-type number.

where $H_0$ is the deep water wave height, $d$ is the sediment diameter, $w_f$ is the sediment fall velocity, $T$ is the wave period, and $L_0$ is the deep water wavelength. Kraus et al. does not look at the beach slope due to the ambiguity of its definition. They also argue that the beach slope is not an independent parameter, but it is a function of the sediment diameter.

### $S_0$ and $N_0$ Criteria

Larson and Kraus (1989) look at the criteria obtained looking at the parameters $S_0$ and $N_0$. They consider data taken from wave tank experiments and found the criteria

$$S_0 = 0.00070{N_0}^3 \tag{2.74}$$

with erosion occurring when $S_0 < 0.00070{N_0}^3$. Kraus et al. (1991) look at this relationship using field data and find that it holds when the average, or root mean square wave height is used as opposed to the significant wave height. The single criteria

$$N_0 = 2.0 \tag{2.75}$$

is a decent estimator, though not as good as using two parameters. In this case, erosion occurs when $N_0 > 2.0$. The two most influential factors are the wave height and the sediment fall velocity so criteria that look at these variables either in separate parameters or in the same parameter will be able to provide some predictive capability.

### $N_0$ and $F_0$ Criteria

Kraus et al. propose a new criteria based on $N_0$ and $F_0$. The criteria is

$$N_0 = 8980{F_0}^2 \tag{2.76}$$

with erosion occurring when $N_0 > 8980{F_0}^2$. This criteria does a good job predicting erosion and accretion for both the large wave tank and the field data sets available. Kraus et al. argue that the parameters even have some physical meaning based on arguments of the energy dissipated in the surf zone and the energy input required to keep the particles in suspension.

### The Profile Parameter

Dalrymple (1992) examines the criteria stated by Kraus and Larson (1988) and by Larson and Kraus (1989) and determines a better criteria for the given data set. The erosion criteria given by Kraus and Larson (1988) is

$$S_0 = 5.5G_0 \tag{2.77}$$

Reexamining the data leads to a better criteria of

$$S_0 = 115{G_0}^{3/2} \tag{2.78}$$

This can be written as

$$\frac{H_0}{L_0} = 115(\frac{\pi w_f}{gT})^{3/2} \tag{2.79}$$

The deep water wavelength is a function of the period and is given by $L_0 = gT^2/2\pi$. Substituting the $L_0$ expression into (2.79) and solving for a single dimensionless variable leads to a new criteria based on the profile parameter, $P_0$, defined as

$$P_0 \equiv \frac{g{H_0}^2}{w_f^3 T} = 10400 \tag{2.80}$$

With the single parameter proposed by Dalrymple, a single parameter can be calculated in order to determine if conditions will be erosional or accretional. Erosion occurs when $P_0 > 10400$.

## 2.4 Experimental Scaling

Beach profile change is the net result of a complicated system of sediment, current and wave interaction. It is impossible for an experiment to preserve all hydrodynamic and sediment transport laws without being full size, so laboratory experiments inherently introduce a scale distortion from what is experienced in the field. Kraus and McDougal (1995) state concern over the scale distortion involved in "small scale" experiments, or experiments with fine to very fine sand and with wave heights less than 15 cm, which puts this experiment into the small scale category. At different scales, different physical processes can be dominant with the end result being errant predictions from the laboratory model. They suggest that experiments involving longshore and cross shore transport would be particularly effected due to the difficulty of scaling suspended load and bed load sediment transport simultaneously. They go on to say,

> Physical model experiments that include both longshore and cross-shore transport are rare and important for their realism, but they may also produce greater spurious results than two-dimensional (cross-shore only) experiments because of greater limitations on wave height and period in basins, as well as because of the presence of artificial circulation in the basin.

This experiment is primarily concerned with cross shore sand transport, but there is some longshore sand movement which occurs during the experiments while studying the interac-

tion between the dune beach and the sea wall beach using normally incident waves. We are studying the phenomenon of beach and sea wall interaction rather than modeling a specific case. Some scale distortion affects the quantitative results, but the qualitative results will still be valid.

Ito and Tsuchiya (1984) look at the scale-model relationship for two dimensional equilibrium beach profiles to determine which scaling relationships lead to model-prototype similitude. By comparing the results from large wave tank experiments with results from medium to small wave tank experiments, they establish scaling relations for similitude. This is especially useful when using a laboratory model to simulate field conditions. They find that, in additon to geometric similitude, the experiment must satisfy Froude scaling as well. Ito and Tsuchiya (1986) discusses the time scale of beach change, for dynamic modeling of coastal changes. They say that the time scale for beach change is equal to the time scale for the wave period. This study is not based on a specific prototype beach or storm, it is concerned with how the beach changes under different wave conditions and how it responds to the presence of a sea wall. Hence, the scale relationships were considered to insure that the experimental conditions are realistic but they are not used extensively.

# Chapter 3

# Experimental Setup

The experiments took place in the J. Robert Gunther Family Three Dimensional Ocean Wave Facility in the Parsons Laboratory. The basin is 11.5 m by 17 m and equipped with a 47 paddle, piston-type wave maker along the long wall. The basin was divided into three subsections during this investigation. Separate research projects were conducted in the three subsections. Section 3.1 describes the general wave basin configuration and the specific layout for the sea wall experiment.

The experiment can be broken down into two major areas: the beach measurement system and the wave generation and measurement system. The beach measuring system consists of a surface elevation profiler mounted on a X-Y plotter. The X-Y plotter is a two axis plotter driven by servo motors. It is described in Section 3.2. The surface profiler uses reflected light to measure the sand surface elevation. It is described in more detail in Section 3.3. Wave generation is discussed in Section 3.4 while wave measurements and analysis are discussed in Section 3.5.

## 3.1 Experimental Section

The 11.5 by 17 m wave basin is shown in Figure 3-1 . One wall of the basin consists of a bank of 47 paddles that are each 30 cm wide and individually computer controlled. The facing wall has a modular wave absorber beach which can be modified to serve an experiment's specific requirements. The paddles are numbered 1 to 47 with paddle 1 closest to the control room. The paddles are controlled from the control room by an IBM PS2 computer with a program called Atlantis written and developed by Hoang Tran and Dr. Eng Soon Chan.

The system is capable of generating waves in either real time or from data files. In real time mode the system is limited by the processor speed and is only capable of relatively simple waves. It is capable of generating an oblique monochromatic wave or a normally incident five component spectral wave in the real time mode at 20 Hz. When the waves are generated from a data file, the system is limited by the memory. The system can generate a 5 minute wave packet at 20 Hz when the waves are generated from a data file. Atlantis was written with a module to generate monochromatic waves in real time mode. It was modified for this project to be able to generate a five component, normally incident spectral wave in real time. Section 3.4 describes wave generation in greater detail.

Three experiments were being conducted in the basin at the same time. This created both a space and time constraint on basin utilization. Each of the projects took approximately a third of the space in the basin and a third of the time as the primary users. The sea wall study ran in the area labeled "experimental section" in Figure 3-1. This section is 4 meter wide and on the far end of the basin from the control room. The physical dimensions of the experimental section are shown in Figure 3-2. The experimental section consisted of the paddles 28 through 40, an open water section with wave gauges, and a sloping beach. The beach was built in a sloping sandbox constructed of varnished marine plywood built onto the absorber beach frame. The bottom of the sandbox has a 1:10 slope and extends out to the basin floor.

The sea wall side used in the experiment was a 1:1.5 sloping sheet of plywood with a double layer of coarse gravel glued to the surface with "Goop" brand glue. The gravel is assorted railroad gravel with diameters ranging from 2 to 5 cm. The gravel used is black, which affects the bottom profiler used to measure the beach. Hence, the sea wall was covered by a layer of white gauze during beach measurements. Experiments were conducted both with the gauze permanently attached and with the gauze added before measuring the beach but removed during the wave events in case the gauze acted as a filter in terms of sand transport.

The project looked at how the two beaches reacted differently when separated by a dividing wall and subjected to equivalent wave conditions and then how the beaches interacted when the dividing wall was removed. The 4 meter wide sandbox was divided into two sections with a plywood divider wall extending 4 m from the back wall. The divider wall extended past the point of net sand movement during any of the experiments so that

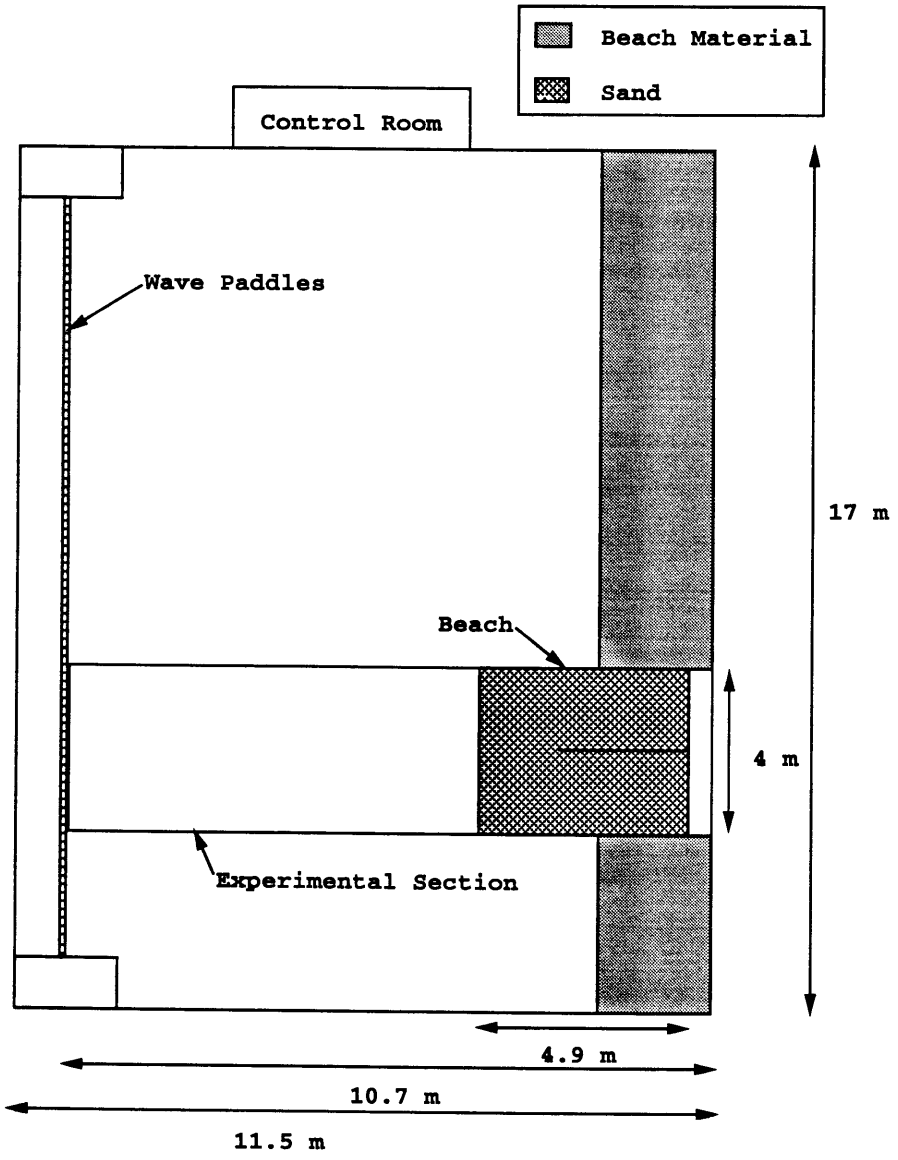


Figure 3-1: Plan view of wave basin.

there was no direct influence of one side on the other while the wall was present. Just past the divider wall on both sides was a set of wave gauges 55 cm apart to measure the wave conditions on both beaches.

The beach was filled in on top of the sand box described above. The two sides were filled in evenly so that the beach conditions seaward of the sea wall were identical, with initial slopes of 1:6, as shown in Figure 3-3. The figure shows a profile of the sea wall side. The dune side is essentially the same, just without the sea wall. The dune begins at the base of the sea wall and follows the slope of the sea wall.

The sand used for the beach is 0.2 mm white Ottawa silica sand sold commercially as F-75 sand. Approximately half of the sand in use was left over from movable bed experiments conducted by Rosengaus (1987). An additional 4000 pounds of F-75 sand was bought in Rhode Island from Tackard Sand and Gravel to complete the beach. It is nearly pure (99.75%) $SiO_2$. The sand is well sorted with a representative diameter of 0.2 mm and with a density $\rho_s = 2.65$ g/cm$^3$. For the sand we can estimate the sediment parameter, $S_\star = 2.845$ from (2.62), and the critical Shield's parameter, $\psi_c = 0.052$ from (2.61). The fall velocity is 2.53 cm/s obtained from the sediment parameter and fall velocity relationship.

Experiments began with approximately identical uniform profiles on the beach and sea wall sections. To obtain these initial profiles the sand surface was smoothed with a rake to make the beaches look, at least visually, similar before experiments. Once the beaches look similar, they were measured using the beach measurement system to see where they differed. This information was used iteratively to smooth out any lumps or differences that were not apparent to the eye but could be measured with the probe.

## 3.2 The X-Y Plotter

The X-Y plotter is a rectangular plotter designed to move a beach profiler within the experimental area. It is a key element in the beach measurement system and is shown in Figure 3-4. It is designed to move a sensor, in this case a surface profiler, anywhere within a large rectangular area with a high degree of accuracy.

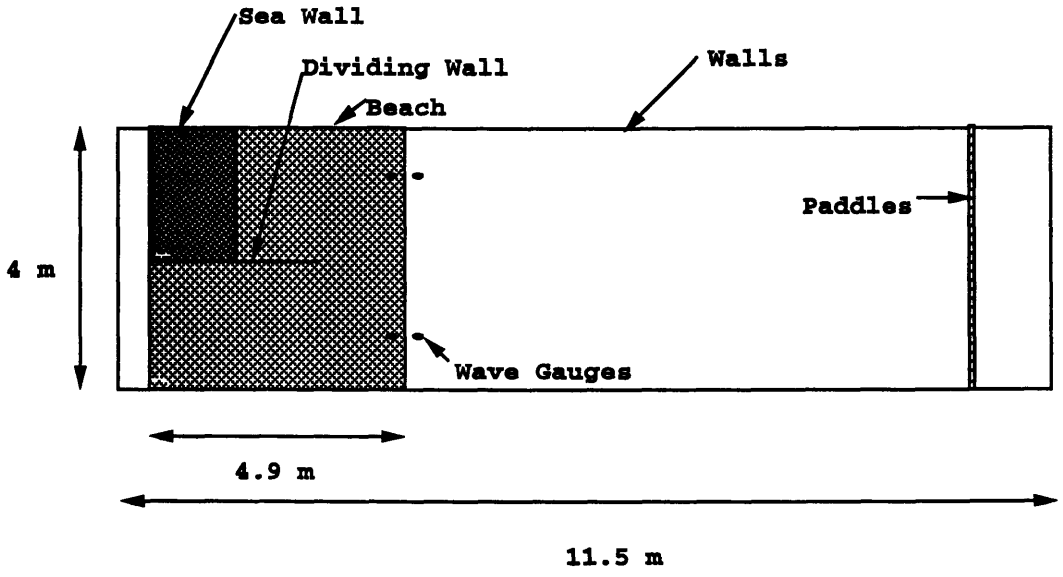


Figure 3-2: Plan view of experimental section.

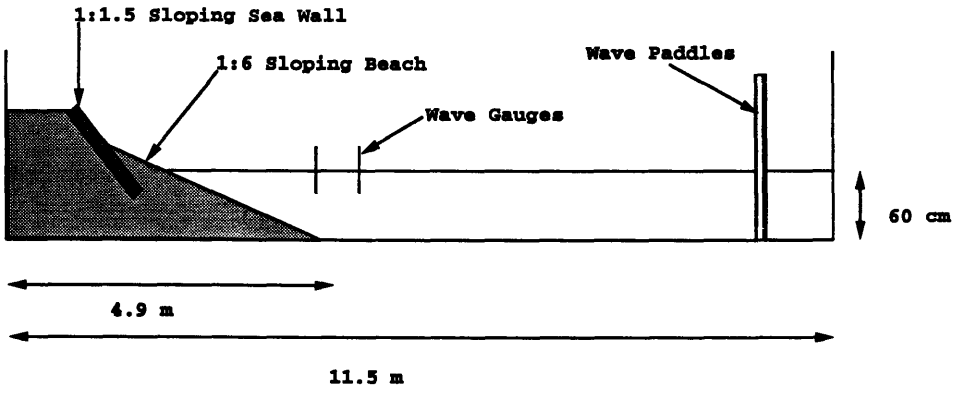


Figure 3-3: Side view of experimental section.

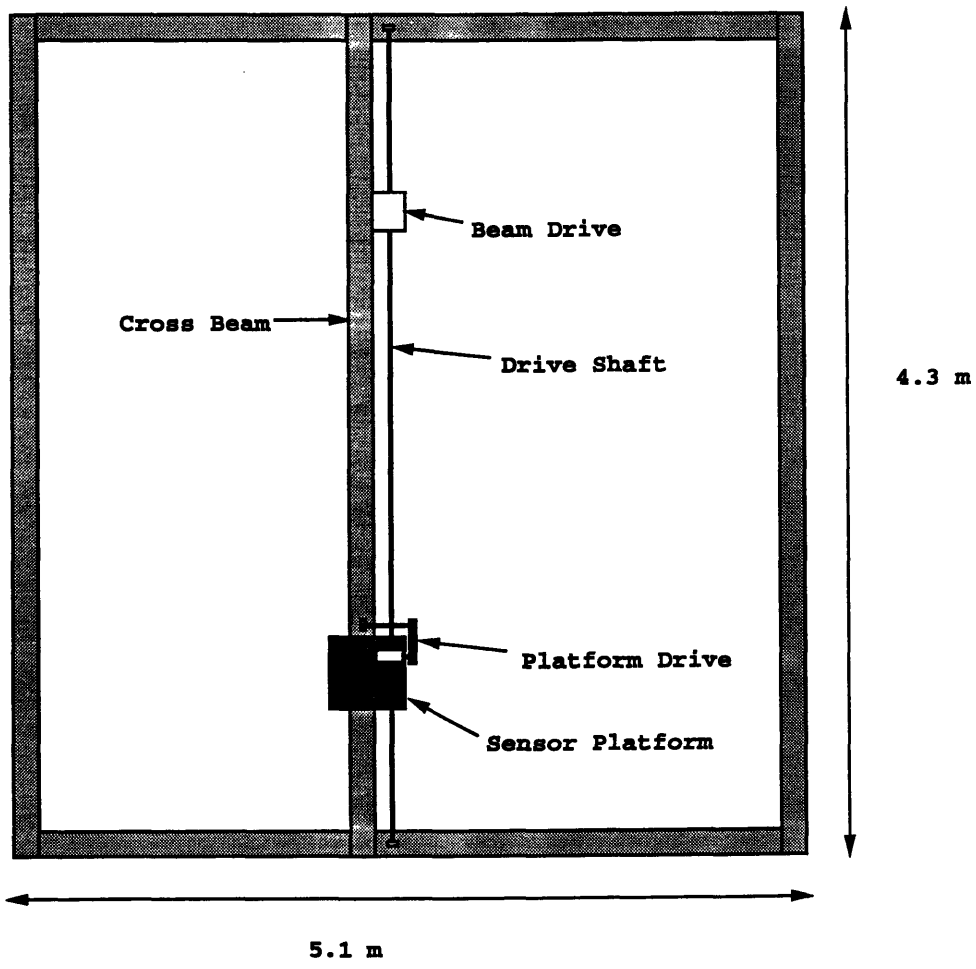


Figure 3-4: Overhead view of X-Y plotter.

### 3.2.1 Design and Construction

The plotter consists of a large rectangular frame with a movable cross beam on which is mounted a movable platform. The frame measures 5.1 m by 4.3 m (16 ft, 8 in by 14 ft) and is made of aluminum beams with a square 10.16 cm (4 inch) cross section and 0.9525 cm (3/8 inch) thick walls. The aluminum was supplied by Industrial Aluminum of Waltham, MA. There is a rail and gear rack mounted on each of the two 5.1 m beams. A cross beam rides on these rails and is driven by a spur gear on the gear rack. The spur gear is driven by a servo motor mounted on the cross beam. The cross beam has a pair of parallel rails with a gear rack between them. The sensor platform rides on the rails mounted on the cross beam, and is driven by a stepper motor mounted on the sensor platform. The detailed design is presented in Appendix A.

### 3.2.2 Plotter Development

The plotter was completed during August of 1994. The following months were used to test and develop the plotter system. The first step involved getting a proper power supply for the motors. Figure 3-5 has a diagram of the Galil motion controller system. The system consists of a motion controller card, a motion controller amplifier board and a power supply. The card inserts into a ISA slot of a IBM compatible PC and is used to communicate with the board. The board, a DMC-1020, has its own processor, so once instructions are sent to the board from the card, they are processed and carried out by the board in the background. The power supply is a separate component so that it can be sized according to the application. By using a variable power supply with a current meter, the power requirements for both motors of the plotter were determined. The X axis, or the platform, needs 2.5 amps at 24 volts while the Y axis needs 3.5 amps at 24 volts. The Y axis has a greater power requirement due to the greater load and inertia. Based on these requirements and a small safety factor, a 7 amp, 24 volt power supply was selected. The motors are connected to the amplifier with a control feedback loop from the digital encoders.

The plotter is controlled by a language written by Galil for its motion control applications. It is designed to use two letter instructions, or Opcodes, for programming. It is a fairly straightforward language that is relatively easy to understand once the basics are understood. Appendix B and "DMC-1000 Technical Reference Guide" (1994) both provide

further detail on programming and using the motion controller.

### 3.2.3 Plotter Calibrations and Accuracy

The plotter uses servo motors equipped with digital encoders for feedback. Each motor has two encoder channels, A and B, with 1000 counts per revolution each. The two channels are offset by a quarter of a count, so that together the encoder has 4000 quadrature counts per revolution with an accuracy of $\pm 1$ count. The quadrature counts are shown in Figure 3-6. Channel A is 0 V from 0 to 2 counts and is 1 V from 2 to 4 counts while channel B is 0 V from -1 to 1 counts and is 1 V from 1 to 3 counts. This way, one count on a channel is 4 quadrature counts for the plotter. The two channels being offset allows 4 times the accuracy, but also allows for directional determination. With channel B leading, the motor is rotating in the positive direction, and while channel A is leading, the motor is rotating in the negative direction.

The motors are connected to a 4:1 gearbelt drive that drives a 8.255 mm ($3\frac{1}{4}$ in) spur gear. As a result, the plotter motion is 0.000748 cm per count. This was experimentally verified by measurement along a steel measuring tape attached to the plotter. The plotter was moved to a specific count and then the plotter position was measured. The plotter has a range of 500,000 counts over the 3.8 meter range of motion which is well within the motion controller range in excess of $\pm$ 2 billion counts. Since the motion controller is not limiting the size of the plotter, the plotter system would be relatively easy to expand. The beams are bolted together through aluminum plates so that the system can be taken apart and either stored or modified. It was built to measure a specific area, but the two 4.9 m (16 ft) beams could be replaced with longer beams with a new set of rack and rails. It could be expanded to cover the entire beach along the back wall if needed. The velocity range is up to 8,000,000 counts/s, which corresponds to nearly 6000 cm/s for this system. The highest velocity we have used is 50,000 count/s, which corresponds to 37 cm/s, while the normal running speed is 10,000 counts/s, or 7.5 cm/s.

Electronically, the position accuracy is $\pm 1$ count, but the system is limited in its accuracy mechanically. There is a small amount of mechanical looseness, similar to play in a steering wheel, this looseness is estimated to amount to less than 1 mm. Hence, the plotter can be returned to make a measurement at the same spot again and again within an accuracy of better than than 1 mm.

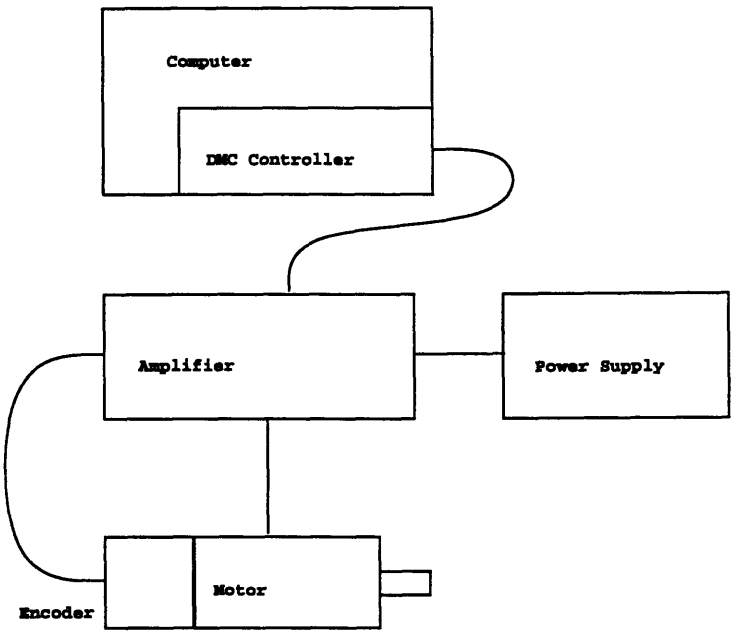


Figure 3-5: Component diagram for Galil motion controller.

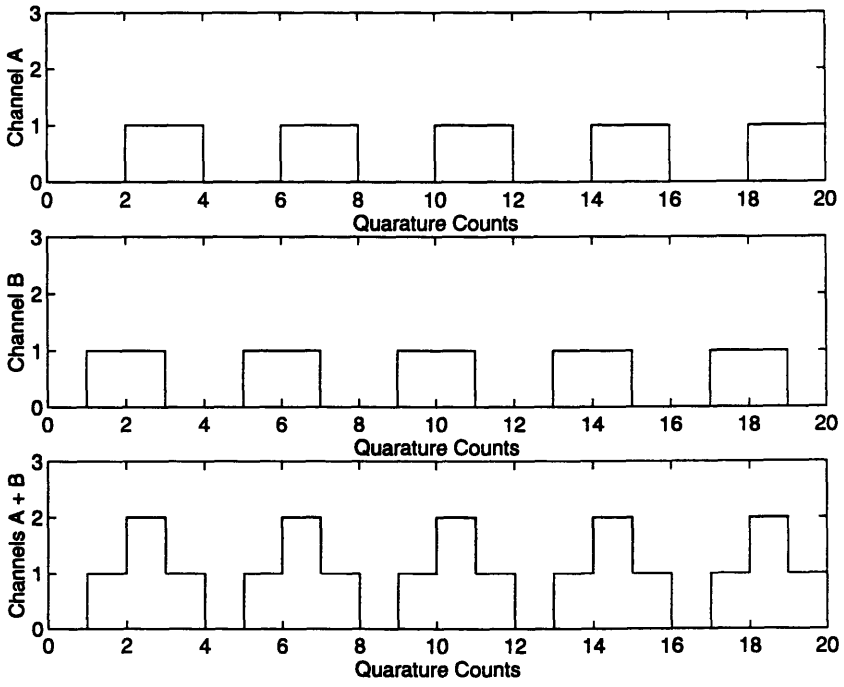


Figure 3-6: Motion control counters: quadrature counts vs. channel output.

The system needs a method of self-calibration. When the board is reset or a mechanical error causes the counter to drift, the position counter needs to be reset. Mechanical errors can occur when the bearings that keep the spur gear properly aligned in the gear racks are not adjusted properly or when the set screw that holds the bearings on the drive shafts are not tight and allow the motor to spin without moving the axis. These have both happened, but these events are rare and easily remedied. The original design included either mechanical or magnetic switches to allow each axis to be electronically reset. These have not been implemented, but could quite easily be by using the extra digital inputs that are not being used. Currently, the system is manually reset by moving the plotter to a known position at the edge of the range of motion and resetting the position. This works well though, so the electronic switch is a low priority.

Galil supplied an installation and calibration program, called "SDK1000", the servo design kit, to help set up and analyze the motors. "SDK1000" walks through the installation and verification of all the elements of the motion control system and includes accessories to tune the motors. The motors are tuned by adjusting the integrator, proportional and derivative gains. An under-damped system demonstrates excessive vibration, while an over-damped system responds poorly. The servo design kit analyzes the system for stability and recommends values for the different gains. These are suggested, but not necessarily optimal, values. After the system had been running for several months, it developed an excessive vibration in the Y axis motion. After trying several different solutions without success, we tweaked the gains until the plotter demonstrated stable behavior again. As of this writing, the plotter has been stable at the current settings for several months with the settings given in Appendix B.

## 3.3 The Beach Profiler

The beach profiler is the second component of the beach measurement system. The profiler is made in Japan by the Masatoyo Company and is available for about $10,000 with spare probes costing about $1000 each. The profiler is shown in Figure 3-7. It uses reflected light to maintain a constant height over any reflective surface.

The profiler has three main components, including the probe, the sleeve and the control box. The probe is a stainless steel tube 135 cm long and 6 mm in diameter. The probe

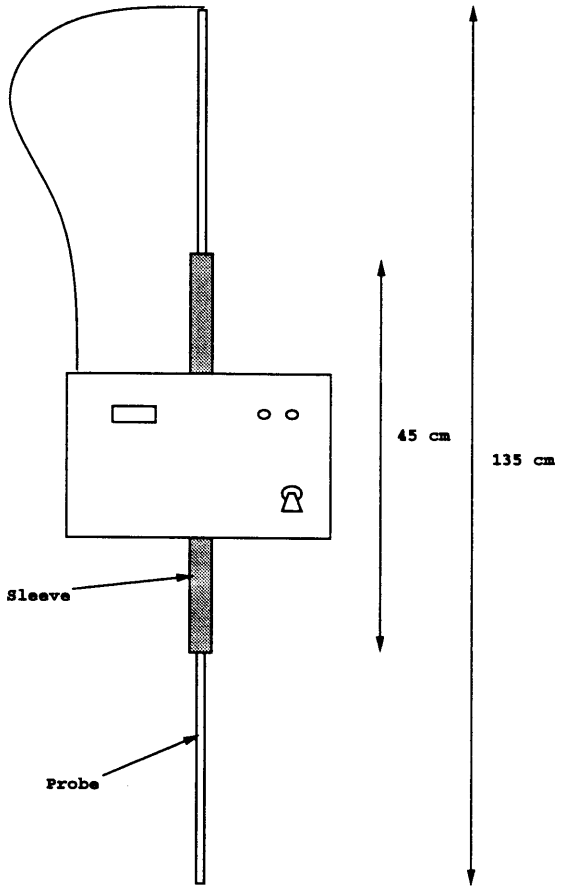


Figure 3-7: Masatoyo bed profiler.

contains fiber optics to transmit the light used for the height measurements. The probe is connected to the control box with a cable and is set in the sleeve with a set screw. The sleeve is a square aluminum tube 65 cm long with a gear rack on one side. It has a 40 cm range of motion. The sleeve is connected by a gear system to the servo mechanism in the control box. The servo mechanism is controlled by a feedback loop from the probe tip. Non-coherent light is emitted from the probe tip and strikes the reflective surface. A receptor on the probe receives the light and then causes the servo motor to move the probe closer to the measured surface if the intensity is below a certain threshold or further away if the intensity is greater. The servo motor sends a voltage to the output which is proportional to the relative position of the sleeve. A close-up of the probe tip is given in Figure 3-8 . Since the sleeve has a range of 40 cm, the profiler can measure up to 40 cm of vertical relief for a given probe setting. To measure more than a 40 cm range, the probe can be set at a different height in the sleeve so that there are two separate but overlapping 40 cm ranges. The maximum vertical speed of the probe is 40 cm/s so the profiler can follow most surface changes. The probe tip is maintained a constant distance of approximately 1 cm over the measured surface. It there is a vertical or over-hanging wall that is greater than 1 cm in height, the probe will not be able to sense it and will run into the obstruction.

The probe maintains a near constant height over a reflective surface of approximately 1 cm. With different materials and different conditions this height does vary, but not by much. The distance over dry sand is 16 mm, the distance over wet sand is 15 mm and the distance over water is 9 mm. If the sand is dirty the probe is affected. If it is only mildly dirty, the probe may close in towards the surface by approximately 2-4 mm, which is within the measurement error. If the sand is very dirty, i. e. if there is a large black smudge of grease, the probe will not see the surface and plunge through into the sand, in which case the probe will not be measuring the surface properly anyway. The discrepancy between the sand and water measurement distances is not a problem. The water level is measured during the experiment, but only for a reference elevation, so it does not matter that the measurement of the water surface is 6 mm different from the sand measurement. The profiler is dicussed in more detail in the next section.

Since the profiler measurements are relative, a reference point must be selected. The water surface is a convenient reference point for several reasons. The water surface elevation is not entirely constant though. It is measured using a yardstick for a daily record of the

depth during the experiments. Water is lost due to evaporation and is periodically added to maintain a generally constant water depth. The loss rate is about 1 mm per day.

### 3.3.1 Profiler Usage

To measure a full profile, the profiler is moved to a specified location where the water surface is measured with the probe set in the sleeve for above the water surface measurements. After measuring the water surface for a reference elevation, the X-Y plotter moves the profiler in a grid search pattern over the above water portion of the beach surface. When complete, the profiler returns to the point where it measured the water surface. Here, the probe is reset to allow it to measure the underwater profile. The water surface is measured again for a new reference elevation for the probe setting before the probe measures the underwater sand surface. A sample grid search pattern is given in Figure 3-9. The profiler takes measurements at discrete points in a rectangular grid. The longshore spacing, or the distance between shore-normal transects, is 14.96 cm. The cross shore spacing is 3.74 cm. The cross shore spacing is smaller because the variation in the cross shore direction is greater than the generally uniform longshore direction. We measured a grid for several reasons. With a grid, the same $x$ and $y$ are measured each time. The data can be in a regular rectangular grid of $z$ values. Also, the profiler output needs to be filtered through averaging, so the profiler stops at each grid point long enough to take measurements.

The profiler measures above the water surface first in order to resolve where the still water line is. That way, when the probe returns along the same transect, but underwater, it does not go past the water surface, a problem that will be discussed shortly. Several attempts were made to get the plotter to recognize the water line automatically, but the easiest and most effective means was the manual approach. This requires the operator to use a joystick button wired into one of the digital inputs to signal the plotter controller that the probe was above the water surface. This signal meant that the plotter should turn around or continue to the next phase of the data collection program. The cross shore position for each transect is stored by the motion controller so the plotter knows the water line location during the below water measurement. The plotter should be stopped 2 or 3 measurements past the water line. When the profiler returns along the below water measurement, it stops where the last measurement was made above water. Within a few measurement iterations, the operator will be able to determine where the plotter is stopped to minimize

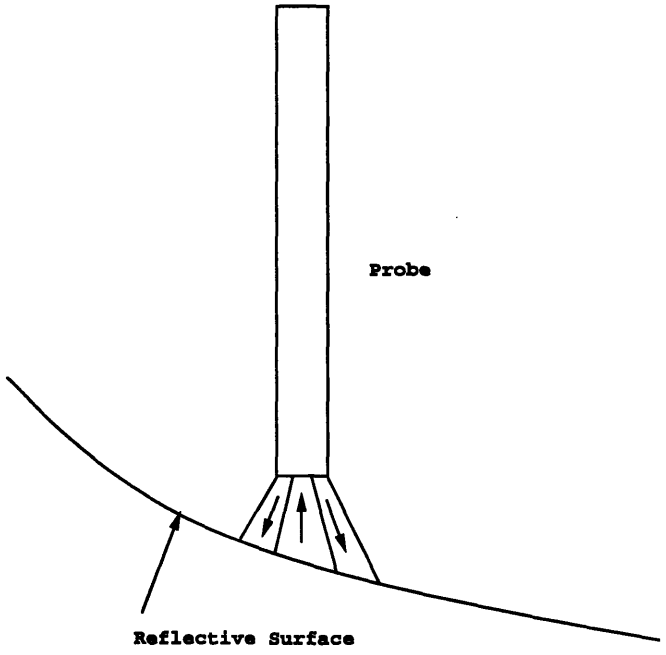


Figure 3-8: Probe tip for Masatoyo profiler.

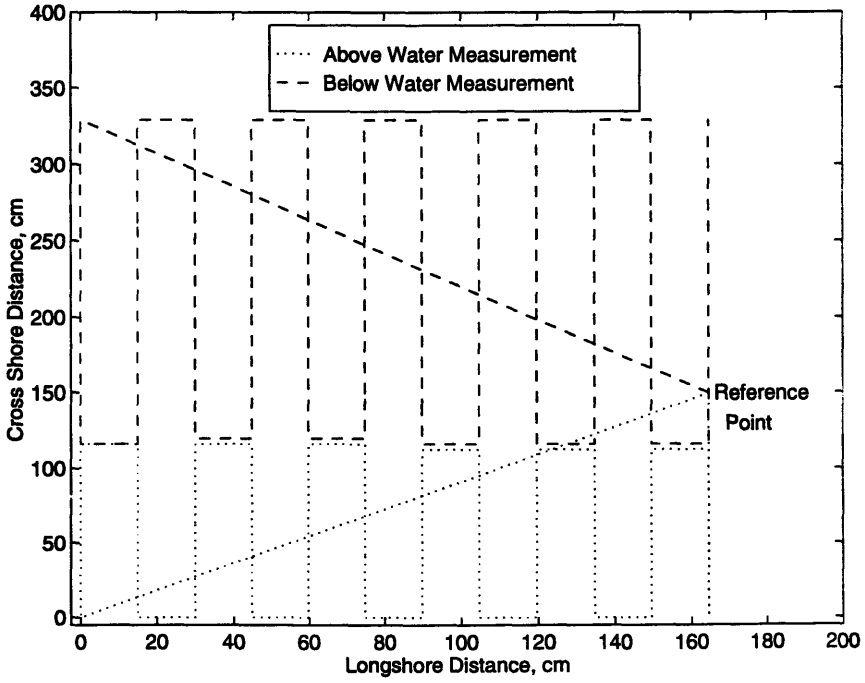


Figure 3-9: Sample grid search pattern for beach profiling system.

lost measurements and to avoid having the probe exit the water. The supervision required is a minor inconvenience, but the profiler requires a certain level of supervision anyway so it is not a problem.

The profiler is able to work both above and below the water surface but there is some difficulty at the interface. Since the water surface is reflective, the probe will not pass through the water surface. If the probe is moving from the sand out over the water, it will not break the water surface, as seen in Figure 3-10.

When the probe is under water and moving towards the interface there is a different problem. Since the probe maintains a 1 cm separation between the tip and the measured surface, at a water depth of less than 1 cm, the probe tip will begin to exit the water, as shown in Figure 3-11. As the probe rises through the water surface, a small bubble of water forms on the tip of the probe. Sometimes when this occurs, the probe "sense" the water bubble as a surface and the probe will shoot up to avoid what it perceives as an obstacle. Other times, the bubble will be smaller and merely cause the optics to get confused and the probe to jitter up and down. This is why the probe tip must be dry for the above water measurements. If the probe exits the water completely, it has to be manually returned under water to continue sampling, which is part of the reason why supervision is required. The other consequence is that the probe cannot measure the 1 cm below the water surface without changing the water elevation in the basin. There is some information lost this way, but the data points that are lost can be extrapolated during the analysis.

Since the profiler works with reflected light, the profiler cannot measure an unreflective surface. When the profiler passes over a black rock on the sea wall or over a dark piece of debris on the sand surface, the probe will be unable to "sense" the surface. The simple feed back loop for the profiler moves the probe down when the probe receives insufficient reflected light. If the object is a rock, the probe will hit the rock and stop. If the object is debris on the sand, the probe will hit the object and continue to punch down through the sand. In either case, the plotter does not know the probe is stuck and will continue to move. If the operator is alert, the plotter can be stopped before any damage is done. If not, the probe can snag and bend. The probe is actually fairly tough, we bent the first probe at least a dozen times, sometimes at a right angle, before it no longer worked. When bent, the probe is bent back as straight as possible and used again. Since the probe cannot be bent back to be perfectly straight, there is a residual bend in the probe. While the probe

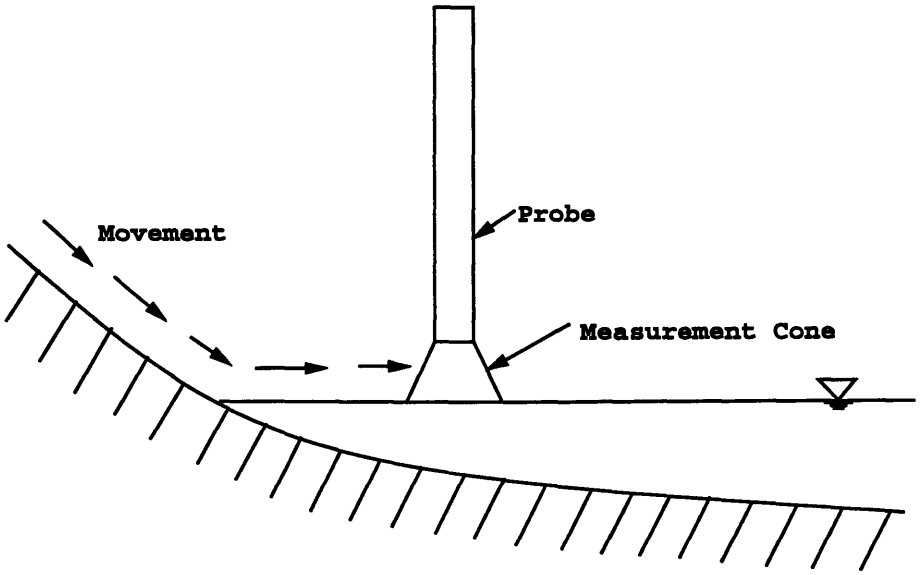


Figure 3-10: Profiler moving out to over the water surface.

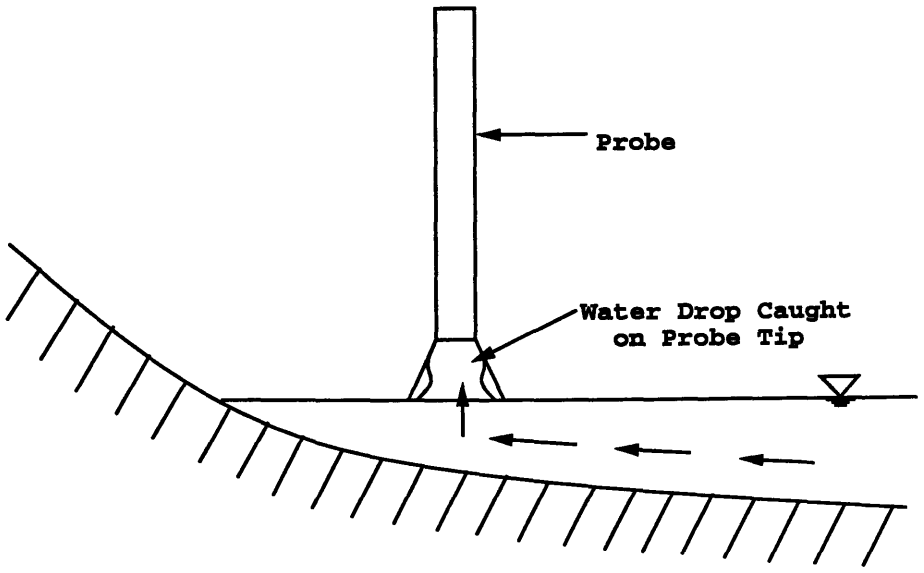


Figure 3-11: Profiler moving from underwater to over water surface.

is straight, it does not matter how the probe is oriented in the sleeve. When the probe is slightly bent, the measurements on a slope will be off if the orientation is not kept constant. This is why the probe orientation must be kept constant throughout the experiments.

Before purchasing the Masatoyo beach profiler, we were considering a Dutch probe which operated on an electric field principle. The Dutch profiler has the distinct disadvantage of only working under water, it cannot be used in the air.

### 3.3.2 Calibration and Accuracy

The profiler returns a voltage corresponding to the relative probe position. The specifications provided through Masatoyo states that the probe has a linear output conversion of 3.33 cm/V. When the probe was calibrated, we learned that the profiler did not have a completely linear output conversion. In order to calibrate the probe, we needed to measure the probe position and compare it to the profiler output. The probe position was taken by measuring how far the probe sleeve extended up past the top of the profiler box. The profiler output was measured with the sampling routine used on the plotter. The measurements were coordinated with the joystick button that is part of the plotter system. To calibrate the entire range of motion, the profiler was set, the height was measured by hand and then the joystick button was pressed so that the plotter system would measure the profiler output. When the full range was finished, the two data sets were combined and analyzed. Figure 3-12 shows the profiler data compared to the linear correlation given by Masatoyo. As one can see from Figure 3-12, the linear fit is not too bad in the middle range, but deviates by more than 5 cm at each extreme. The calibration is improved dramatically when a quadratic equation is used. Using Matlab for data analysis, the following quadratic equation results:

$$z = 0.1696V^2 + 2.061V + 4.790 \tag{3.1}$$

where $z$ is the relative height in cm and $V$ is the output voltage in volts. This fit is shown in Figure 3-13. During the data analysis, the profiler data can be run through the calibration equation to obtain relative heights for the measured points.

A major developmental hurdle in probe accuracy was with electronic noise. The profiler is located in the basin with about 30 m of cable running back to the computer. The cable is in a bundle with the power to the servo motors, the encoder feedback from the

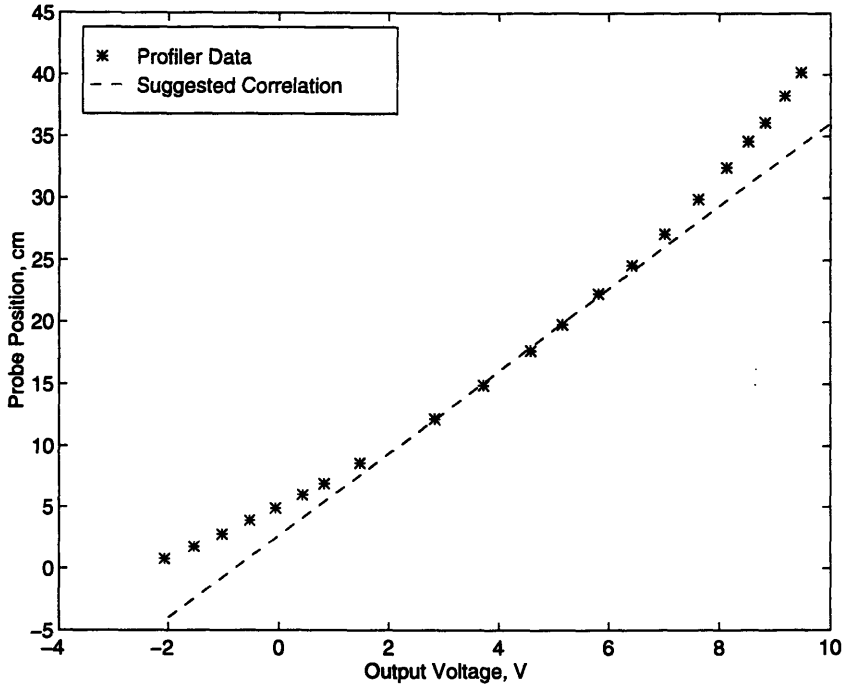


Figure 3-12: Profiler calibration with suggested correlation.

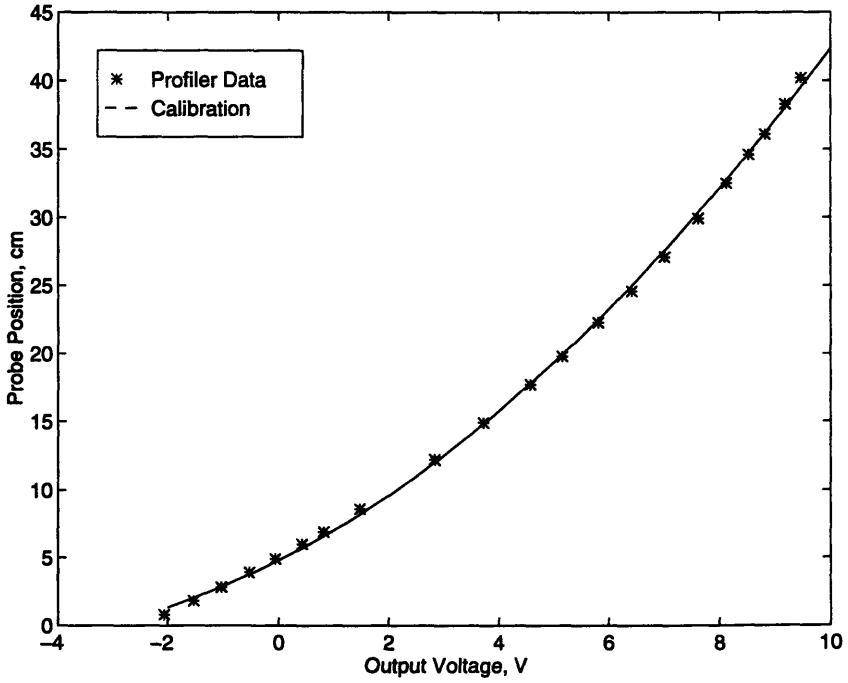


Figure 3-13: Profiler calibration with quadratic fit.

motors and the joystick signal. Even with a shielded BNC cable, the signal is still noisy from background radiation and from the close proximity to the other cables, especially the cables that power the servo motors. The amplitude of the signal noise is 0.5 Volts, which corresponds to over 2.5 cm in surface height variation. Several attempts were made to filter the noise out with the most successful being signal averaging. The sampling routine on the plotter system samples the probe output 200 times and averages the results. The choice of 200 was a compromise between the time required to sample and the accuracy desired. The motion controller clock is used for velocity and acceleration calculations. This clock cannot be accessed for data acquisition, so the motion controller sample rate for the profiler data is determined by how quickly the program can tell the board to sample the input channel. We never explicitly tried to determine the sample rate, but it is of the order of 1000 Hz. Without the motors on, averaging 200 samples gives an accuracy of better than 1 mV, which corresponds to 0.0033 cm. With the motors on, the system has an accuracy of 6 mV or 0.02 cm. The specifications provided by Masatoyo state a system accuracy of 0.2 mm which we are able to reproduce.

The beach measurement system, if it is to be useful, must be accurate. The system is complex, so it required some tuning before we were able to achieve an acceptable accuracy. Some of the tuning is described above, while the rest is described in Appendix B. One measure of system accuracy is sand conservation. Figure 3-14 shows the calculated sand volume for both the sea wall side and the dune side during the March experiments. The sand volume was calculated using the simplest method, summing the volume contribution from each measurement. The sand elevation from the profiler is relative to the water surface, so the water depth was used to translate the height relative to the water surface to the height relative to the floor of the basin. These heights were multiplied by the measurement area, $\Delta x \Delta y$, and summed to obtain the volume. As mentioned earlier, $\Delta y = 3.74$ cm and $\Delta x = 14.96$ cm. The variation in sand volume measured as a standard deviation, corresponds to a layer of sand 0.2 cm thick over the entire measurement area. This measurement error is of the same order of magnitude as the water elevation measurement accuracy. Also, the measurement grid is very large, so the fine detail such as the ripple geometry is lost. If one measurement hit a majority of ripple crests and the next hit a majority of ripple troughs, there would be a significant apparent change in sand volume without a real change in sand volume.

Another important feature of the plotter is its resolution. The grid we are using for the plotter is large, so the fine detail is lost. The plotter system can be used to capture much finer detail with very little adjustment. To test the resolution, we used the plotter to scan a foot print in the sand on the test beach. A three dimensional rendition of this foot print is given in Figure 3-15. The measurement interval for this scan was 0.374 cm by 0.374 cm or 500 by 500 counts. More detail is possible with a finer resolution, but the point is that the plotter system is able to measure the fine detail of a foot print and reproduce a known geometry. Therefore, it has no trouble with larger scale phenomena such as ripples or berms.

## 3.4 Wave Generation

The wavemaker was run using the software developed by Hoang Tran known as Atlantis. Atlantis is documented in Tran (1994). It is written in C using the Microsoft C compiler, version 6.0. The program is set up with a command line user interface. It is semi-modular in that new functions can be added to the code as needed. For instance, Atlantis was written with a function called "signal" to generate monochromatic waves in real time. The code for "signal" was modified into a function called "spectrum" to generate 5 component spectral waves that were used for the spectral waves in this experiment. This is described in more detail in Section 3.4.3. Atlantis is a stable program that works well, but it is limited due to the IBM PS2 and the DOS operating system, as discussed earlier.

### 3.4.1 Wavemaker Calibration

The wave maker was never calibrated when installed, so a wave maker calibration was necessary. The first phase was a static calibration of the wave paddles. Atlantis accepts paddle positions as voltages with 0 Volts being fully recessed and 10.24 Volts being fully extended. For the static calibration, the paddles were moved to a given location and the paddle positions were marked on the basin floor and the voltage read by the transducer for each paddle was recorded. The transducer voltage matched the input voltage, a fact which is used later for the dynamic calibration. The paddles were measured at 0, 1, 4, 6, 8 and 10 Volts. Figure 3-16 shows the results of the static calibration for a single paddle. The other paddles have similar results. The static calibration is given by:

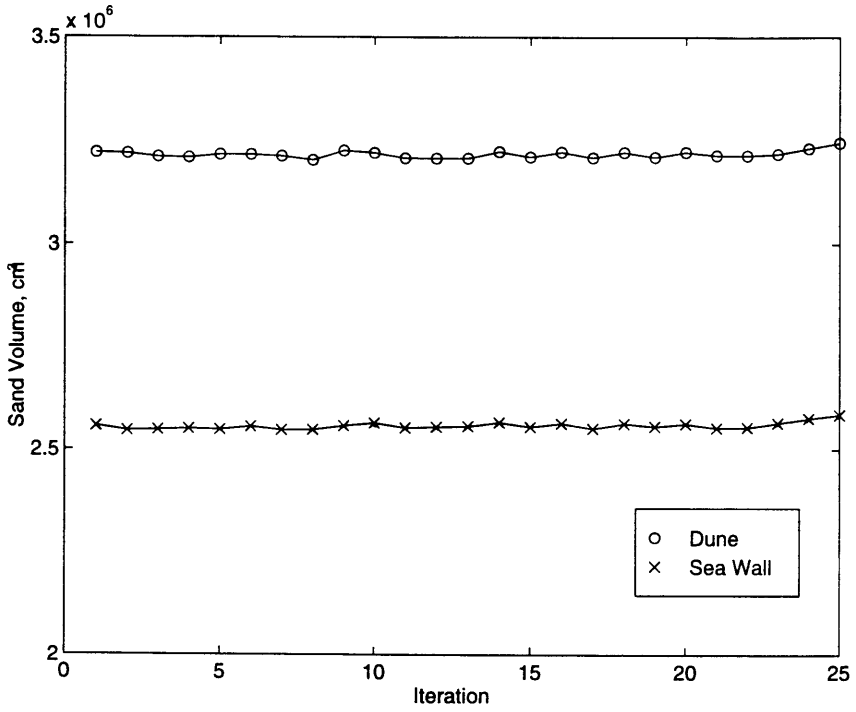


Figure 3-14: Measured sand volume conservation for March experiment.

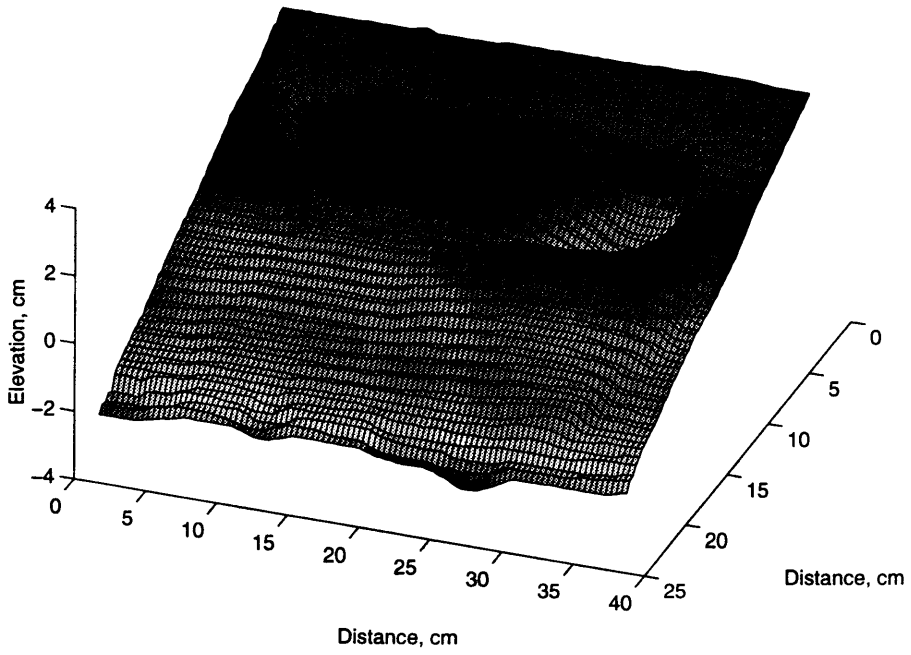


Figure 3-15: Three dimensional plot of foot print on sloping beach as measured by plotter system.

$$\zeta = mV_{inp} \tag{3.2}$$

where $\zeta$ is the paddle position in cm, $V_{inp}$ is the voltage input to the computer and $m$ was measured to be 6.00 cm/V.

The second stage was the dynamic calibration of the wave paddles. The dynamic calibration was run by sending a monochromatic wave signal with a known input amplitude and measuring the transducer voltage from the paddle. The wave paddle motion is given by

$$\zeta = \bar{\zeta} + \tilde{\zeta} \tag{3.3}$$

where $\bar{\zeta}$ is the steady state term and $\tilde{\zeta}$ is the time-variant term. The transfer function, $H$, relates the time variant wavemaker input voltage to the wavemaker output and has the units of Volts per cm of wavemaker motion. $H(\omega)$ is defined by the equation:

$$H(\omega) = \frac{\tilde{V}_{inp}}{\tilde{\zeta}} \tag{3.4}$$

Since we measured the transducer output, the transfer function was obtained from the equation:

$$H(\omega) = \frac{\tilde{V}_{inp}}{m\tilde{V}_{mes}} \tag{3.5}$$

where $m$ is from the static paddle calibration determined above and $V_{mes}$ is the voltage measured from the transducer.

The transfer function, $H(\omega)$, has two components, a magnitude and a phase as shown:

$$H(\omega) = He^{j\phi(\omega)} \tag{3.6}$$

where $H$ is the magnitude of the transfer function and $\phi(\omega)$ is the phase lag, for a given frequency. For spectral waves, we do not need the phase lag and did not calculate it. Each component of the spectral wave is generated with a random phase, and an extra phase lag will not make a difference in the wave that is generated. If we were interested in generating Stokes Second Order Waves, where the frequencies have to be in phase, we would have to calculate the phase lag for the wavemaker.

Several different factors were looked at for the dynamic calibration. Single paddle motion was compared with three paddle and fifteen paddle motion. The calibration was not affected

by the number of paddles running, water depth changes or changes in hydraulic temperature. The paddle motion was frequency dependent though. For three different frequencies and four different amplitudes, the paddle displacement was measured as the paddle transducer voltage.

The results of the dynamic calibration of paddle 40 are given in Figure 3-17. The rest of the paddles had the same results, with the best fit given by

$$H = \frac{1}{6.24 - 0.207\omega} \tag{3.7}$$

where $\omega$ is the radian frequency or

$$H = \frac{1}{6.24 - 1.30f} \tag{3.8}$$

where $f$ is the frequency in Hz. The experiment uses a range of frequencies from 0.32 Hz to 1.37 Hz, which is a range reasonably covered by the calibration.

### 3.4.2 Monochromatic Waves

The original version of "Atlantis" comes with a real time monochromatic wave generator function, called "signal." The "signal" function generates a wave with given amplitude, frequency and direction. The direction can be adjusted by changing the relative phases of the paddles. The first experiments, in October of 1994, used monochromatic waves generated using the "signal" wave generator function. There were some problems with the wave data collection and beach data collection during the October experiments, so it was mainly used to work the kinks out of the experimental procedures. Later, in the January of 1995 experiments, spectral waves were used, but a few experiments were run comparing the effects of spectral waves with the equivalent monochromatic waves. The results of the experiments comparing monochromatic and spectral waves is discussed in Section 4.2.

### 3.4.3 Spectral Waves

Waves in the real world are not monochromatic. We seek to simulate real world effects, so we need a way to generate spectral waves. There are several approaches to generating spectral waves, but they all begin from the same point, the spectrum. This project uses the

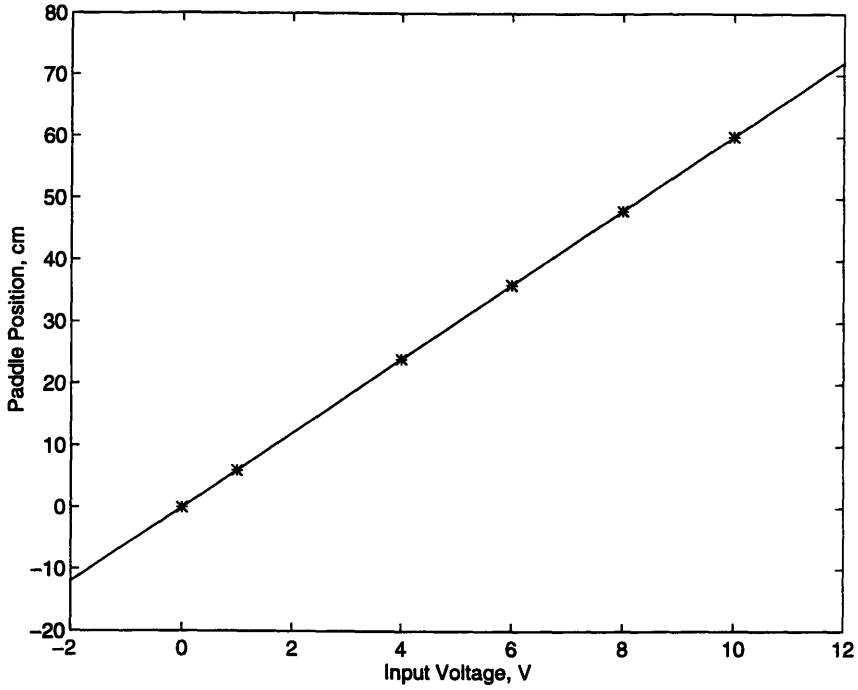


Figure 3-16: Static calibration results for paddle number 40.

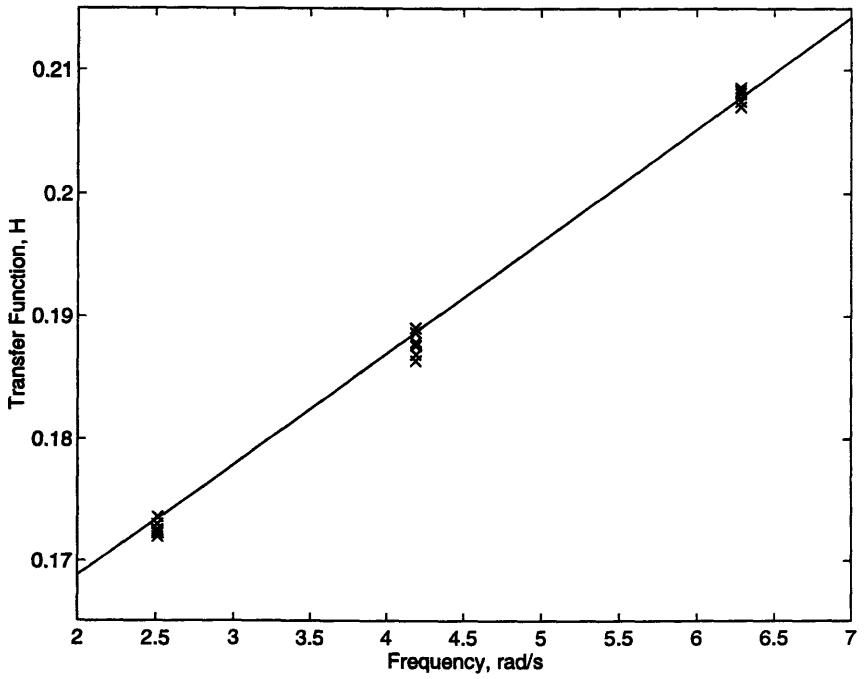


Figure 3-17: Dynamic calibration of paddle 40: $H$ in V/cm vs. $\omega$ in rad/s.

finite depth attenuated JONSWAP spectrum defined by (2.32). The peak frequency, $\omega_p$, is one of the five free parameters defining the JONSWAP spectrum. Normally, the equivalent or average frequency, $\omega_{eq}$, is given or desired. The peak frequency cannot be solved for as a function of the equivalent frequency. Hence, the spectrum must be calculated iteratively to find the peak frequency that yields the desired equivalent frequency which is defined by (2.17).

Given the JONSWAP spectrum we divide the spectrum into regions of equal area, and hence equal energies. Within the frequency range, a representative frequency, either the mean or weighted mean, is chosen. The representative frequencies can be adjusted so that any non-linear interactions such as second harmonic and direct interference frequencies do not correspond to the chosen frequencies. Since the spectral partitions have equal areas, and hence equal energy, they also will have equal amplitudes. To scale the energy by a factor of 2, all of the amplitudes are scaled by a factor of $\sqrt{2}$. From this, the n component wave maker motion, $\zeta$, is given by

$$\zeta = a \sum_{i=1}^{n} b_i \sin(\omega_i t + \phi_i) \tag{3.9}$$

where $a$ is the wave amplitude in cm, $b_i$ is the amplitude for component $i$ in cm of wave maker motion per cm of wave amplitude, $\omega_i$ is the radian frequency of component $i$ and $\phi_i$ is the random phase associated with component $i$. The component wave amplitudes are given by

$$b_i = \frac{1 + \frac{2k_i h}{\sinh k_i h}}{2 \tanh k_i h} \tag{3.10}$$

where $h$ is the water depth and $k$ is the wave number. This term is due to wave maker theory (e. g. Madsen 1971), relating the wavemaker displacement to wave amplitude for a finite depth wave basin.

The calibration from Section 3.4.1 is used to relate the wavemaker motion to the input voltage from the computer. This voltage $V_{in}$ has a steady term and a time variant term as shown in the equation:

$$V_{in} = \bar{V} + \tilde{V} \tag{3.11}$$

As a result the input to the wavemaker is given by the equation:

$$V_{in} = \bar{V} + a\sum_{i=1}^{n} H_i b_i \sin(\omega_i t + \phi_i) \tag{3.12}$$

where $H_i$ is the transfer function value for the component with frequency $\omega_i$.

The wave generation outlined above is a general method for a $n$ component wave for a given spectrum. To generate spectral waves, one needs to select the appropriate spectrum and then decide how many components one wants and how they are selected. Rosengaus (1987) and Mathisen and Madsen (1993) looked at spectral waves in the large flume in the Parsons Laboratory using a five component spectral wave based on the finite depth JONSWAP spectrum with each component having equal energy, and hence equal amplitude. Because an equal wave energy distribution allows for simple linear scaling of the amplitudes, it was chosen for the spectral generation method. With five components, one gets a decent spectral approximation and the frequencies are far enough apart to allow for good resolution during analysis.

The study looks at three different spectral equivalent wave periods: 1, 1.5 and 2 seconds. The frequencies, wave numbers and wave lengths for each component of the 1, 1.5, and 2 second waves and 60 cm water depth are given in Tables 3.1, 3.2, and 3.3 respectively. The wave length is given because the wavelength is important for wave gauge spacing and reflection coefficient determination.

## 3.5 Wave Data Collection and Analysis

Wave maker theory predicts the wave conditions for a given wave maker output, but the wave conditions must be measured to determine the wave conditions actually present. Several data collection and analysis methods were tried before the final methods were selected.

### 3.5.1 Data Collection

The data collection program that was used during the October experiments was developed by Rosengaus (1987). It was written in Fortran programming language and used a Kiethley-Metrobyte DAS16 data acquisition card. One of the problems with the October experiment data is due to this acquisition program. The program appears to have been corrupted from

Table 3.1: Wave parameters for 1 s spectral waves.

| Frequency ($Hz$) | Wave Number ($cm^{-1}$) | Wave Length ($cm$) |
|---|---|---|
| 0.72 | 0.0235 | 267 |
| 0.80 | 0.0277 | 227 |
| 0.88 | 0.0325 | 193 |
| 1.03 | 0.0432 | 145 |
| 1.37 | 0.0757 | 83 |

Table 3.2: Wave parameters for 1.5 s spectral waves.

| Frequency ($Hz$) | Wave Number ($cm^{-1}$) | Wave Length ($cm$) |
|---|---|---|
| 0.44 | 0.0124 | 506 |
| 0.52 | 0.0151 | 416 |
| 0.60 | 0.0182 | 345 |
| 0.74 | 0.0245 | 256 |
| 1.08 | 0.0437 | 132 |

Table 3.3: Wave parameters for 2 s spectral waves.

| Frequency ($Hz$) | Wave Number ($cm^{-1}$) | Wave Length ($cm$) |
|---|---|---|
| 0.32 | 0.0087 | 722 |
| 0.36 | 0.0098 | 641 |
| 0.45 | 0.0127 | 494 |
| 0.57 | 0.0170 | 369 |
| 0.97 | 0.0387 | 162 |

its original, working form. It was aliasing the data and was generally unreliable.

In the meantime, Hoang Tran had developed a data acquisition program in the same format as Atlantis called "Neptune". Neptune is written in the C++ programming language and runs in the DOS environment. This project moved to Neptune because Neptune was more reliable and it made more sense for the research groups in the wave basin to be using the same software rather than "reinventing the wheel" or having three different data acquisition programs in three different programming languages. Also, the data acquisition card was upgraded to the Cyber Research CYRDAS-1602 card which is 100% compatible with the Kiethley-Metrobyte DAS-1602 card used by the other groups in the basin.

Both sections of the experimental area had a pair of wave gauges separated by 55 cm as shown in Figure 3-2. The gauges are set perpendicular to the wave front to measure the incident and reflected waves on both beaches. At least two gauges are needed to resolve the incident and reflected waves. Ideally, the gauges should be set $\frac{1}{4}L$ apart where $L$ is the wave length of the wave component one is looking for. Gauges set at $\frac{1}{4}L$ convey the most information, while gauges set at an integer multiple of $\frac{1}{2}L$ carry no information. Given the 15 frequencies that we were generating for the three wave conditions we were using, we calculated the wavelengths to see if there was a gauge length that avoided $\frac{1}{2}L$ for all of the frequencies. The optimal placement for the wave gauges was 55 cm as can be seen from the wavelengths given in Tables 3.1 through 3.3.

### 3.5.2 Analysis

The data analysis and processing for the project was done using Matlab, version 4.2c for the workstation and version 4.0 for the PC. Matlab is highly flexible and has some excellent signal processing routines which make it a great tool for looking at wave data. We use a modified version of the function "Spectrum" in the Matlab signal processing toolbox. The source for the math for this function is Oppenheim (1975).

The main signal processing function is the Discrete Fourier Transform, called *FFT* in Matlab. If the length of the vector is a power of two, a fast radix-2 fast Fourier transform is used. The *FFT* converts the data from time-amplitude space to amplitude-phase space and returns the complex Fourier transform of the data. The wave spectrum is obtained by squaring the magnitude of the complex Fourier transform.

To obtain greater resolution than achieved by a single Fourier transform, the data is

sectioned, Hanning windowed, put through the *FFT* and accumulated. This sum is scaled by a factor based on the number of sections and the window used to get the spectrum. The resulting spectrum is called $P_{\eta\eta}$ and is related to the wave spectrum, $S_{\eta\eta}$ by

$$S_{\eta\eta} = \frac{P_{\eta\eta}}{ns\Delta\omega} \tag{3.13}$$

where $ns$ is the number of samples analyzed, $\Delta\omega = 2\pi/T_M$ is the frequency increment of the spectrum and $T_M$ is the time length of the sampling record. Then from (3.13) and (2.14), the component amplitude is given by

$$a_i = \sqrt{2P_{\eta\eta}(\omega_i)/ns} \tag{3.14}$$

The *FFT* does not hit the wave frequency exactly, some of the wave energy "leaks" into the adjacent frequencies. To determine the amplitude of a component, we first find the peaks in terms of wave energy. Then we window around the peak adding the energy contributions form the adjacent points. If the peak is at $\omega$, we look at the energy contribution from frequencies $\omega + \Delta\omega$ and $\omega - \Delta\omega$ and add the contribution if it is greater than 1% of the energy. The program continues to window around the peak adding the increment as long as the contribution is greater than 1% and the spectrum does not start rising towards the next peak. The real data we are looking at has several peaks that are close together and this was needed to prevent the program from taking two peaks at once. The amplitude is obtained from the square root of the energy, and the phase is obtained from the phase of the complex Fourier transform for the particular peak frequency. The incident and reflected amplitudes are obtained using the procedure described in Section 2.1.3.

To test the analysis program, we ran some synthesized data through it to make sure that it was running properly. If a program cannot accurately analyze the synthesized data, then the program will not be able to accurately analyze real data. Since the real conditions are unknown, real data cannot be used for program calibration. Synthesized data has controlled inputs so we can compare the analyzed output with the input. The data was created with the following equations

$$\eta_1 = \sum_{n=1}^{5} [a_{i,n} \sin(2\pi f_n t + \phi_{i,n}) + a_{r,n} \sin(2\pi f_n t + \phi_{r,n})] \tag{3.15}$$

Table 3.4: Wave analysis test case with synthesized data.

| Frequency, $f$, $Hz$ | $a_{i,inp}$, $cm$ | $a_{r,inp}$, $cm$ | $a_{i,mes}$, $cm$ | $a_{r,mes}$, $cm$ |
|---|---|---|---|---|
| 0.30 | 1.00 | 0.10 | 0.9992 | 0.0999 |
| 0.40 | 1.20 | 0.20 | 1.1996 | 0.2000 |
| 0.50 | 1.30 | 0.30 | 1.2992 | 0.2999 |
| 0.60 | 1.40 | 0.40 | 1.3996 | 0.3997 |
| 0.70 | 1.50 | 0.50 | 1.4992 | 0.4997 |

Table 3.5: Wave analysis of data from a nominal 2 s spectral wave with 1.2 cm wave components.

| Frequency, $f$, $Hz$ | $a_{i,dune}$, $cm$ | $R_{dune}$ | $a_{i,wall}$, $cm$ | $R_{wall}$ |
|---|---|---|---|---|
| 0.317 | 1.632 | 0.66 | 1.635 | 0.50 |
| 0.354 | 0.887 | 0.46 | 0.823 | 0.39 |
| 0.446 | 0.957 | 0.29 | 0.880 | 0.22 |
| 0.562 | 1.209 | 0.29 | 1.192 | 0.24 |
| 0.952 | 1.114 | 0.18 | 1.047 | 0.09 |

$$\eta_2 = \sum_{n=1}^{5} [a_{i,n} \sin(2\pi f_n t + \phi_{i,n} + k_n d) + a_{r,n} \sin(2\pi f_n t + \phi_{r,n} - k_n d)] \qquad (3.16)$$

where $d$ is the wave gauge separation, 55 cm. Table 3.4 shows the input data and the analysis results. As shown, the analysis matches the input at better than 0.1%, which is very good agreement.

The spectrum of the synthesized data is given in Figure 3-18 compared to a spectrum from real data shown in Figure 3-19. The real data is for the case of a nominal 2 s spectral wave with each component having a 1.2 cm amplitude. Table 3.5 shows the analysis results for the real data with the peak frequencies and the incident amplitudes and reflection coefficients for both the dune side of the experiment and for the sea wall side. The nominal amplitude of each component is 1.2 cm, but the actual amplitudes vary from this nominal value because of the the reflected wave. If the incident wave is reflected off the beach and then off the paddles, the wave amplitude will change as the reflected wave interferes with the incident wave off of the paddle. If the waves are out of phase, the wave amplitude could be as small as $a_{nom}/(1+R)$ and if the waves are in phase, the wave amplitudes could be as large as $a_{nom}/(1-R)$.

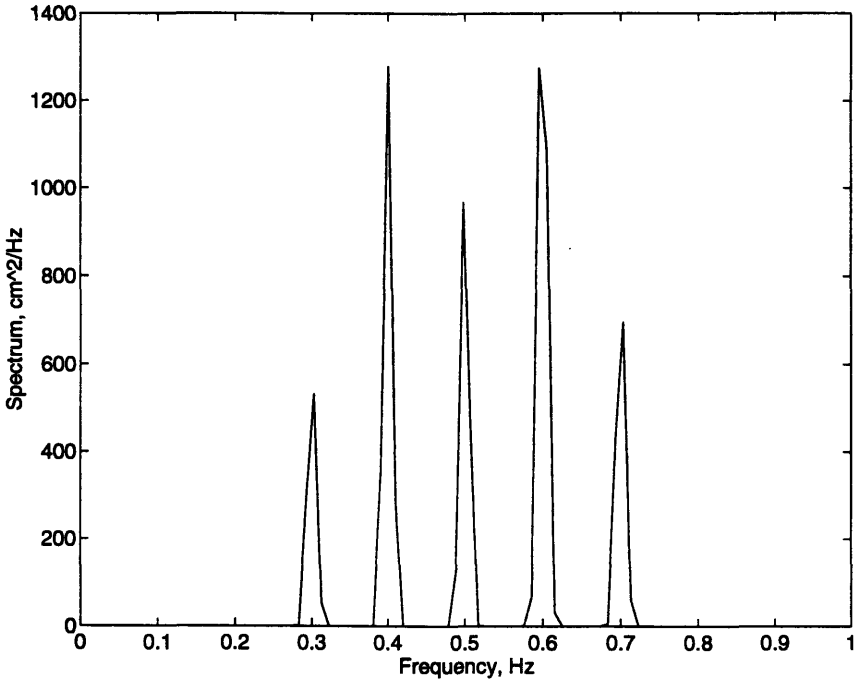


Figure 3-18: Wave spectrum of synthesized data.

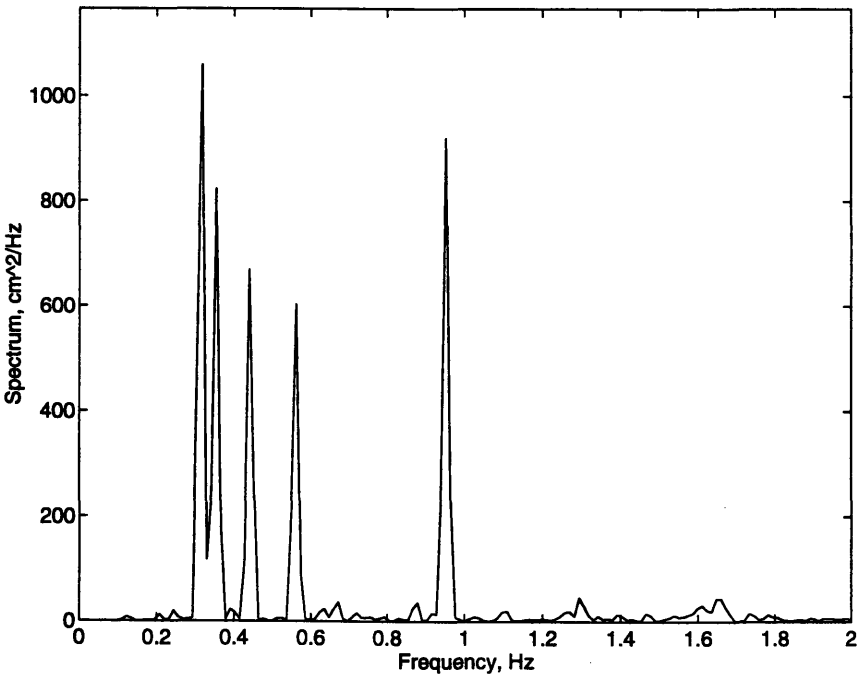


Figure 3-19: Wave spectrum of data for a nominal 2 s spectral wave with 1.2 cm components.

For the data presented in Table 3.5, the dune side has an equivalent wave condition of $T_{eq} = 2.00$ s and $H_{eq} = 5.3$ cm while the sea wall side has an equivalent wave condition of $T_{eq} = 2.03$ s and $H_{eq} = 5.2$ cm. The equivalent reflection coefficients are 0.47 for the dune side and 0.36 for the wall side. The wall side seems to have less reflection, and this is consistent throughout the data. The reflection coefficient is a measure of the reflected energy, which implies that the lab sea wall is a better wave energy absorber and dissipator than the dune formation. Lab studies of sea walls, including Sato et. al (1969) have shown that sloping sea walls, with lower reflection coefficients, produce less scour. With the sloping, rubble mound sea wall, we did not observe significant scour even under the harshest eroding conditions, possibly due to the high energy dissipation of the sea wall. As the waves hit the sea wall, the waves are broken up so the reflected wave is small. On the dune, the incident wave dissipates energy in the surf zone, just as in the case of the sea wall. The difference is that the wave on the dune side runs up the beach, and then washes back down. The back wash on the dune caused a measurably larger reflection coefficient on the dune side.

Throughout the paper, we refer to the equivalent incident wave conditions with an equivalent period and an equivalent wave height. Included in this simplification is the assumption that the wave conditions on the dune and on the sea wall are reasonably equivalent and reasonably time-invariant. This section demonstrates the validity of these simplifying assumptions, allowing us to use an average equivalent wave condition.

There are three different nominal wave conditions that we look at, waves with an equivalent period of 1, 1.5 and 2 s. The first case looked at is for a wave with an equivalent nominal period of $T_{eq,nom} = 1.5$ s and an equivalent nominal waveheight of $H_{eq,nom} = 8.0$ cm. This corresponds to a spectal wave with 1.8 cm incident wave amplitudes for each component. The calculated incident amplitudes for each component are plotted in Figure 3-20 for the dune beach and in Figure 3-21 for the sea wall during a 60 minute wave event. The equivalent wave heights for the dune and sea wall are given in Figure 3-21. The measured components are distributed about the nominal 1.8 cm amplitude with a range from 1.4 cm to 2.3 cm. The temporal variation of each component is significantly less than the variation between components, suggesting that the wave conditions are relatively constant. The equivalent wave conditions shown in Figure 3-22 with an average of $H_{eq} = 7.9$ cm on the dune side and $H_{eq} = 7.1$ cm on the sea wall side. This variation, though consistent over this set of waves, is only a difference of 10% of the average wave height. In the experimen-

tal results, this difference is negligible and the wave condition is reported as the average condition, $H_{eq} = 7.5$ cm for both sides and for the entire hour. This example has a typical variation in incident wave amplitudes, but a greater than normal difference in wave heights between the two beaches.

In addition to measuring the incident wave conditions, we measure the reflected wave amplitudes, from which we can calculate the reflection coefficients. The reflection coefficients are shown by component in Figure 3-23 for the dune beach and in Figure 3-24 for the sea wall. One expects that as the frequencies decrease and the wave lengths increase, the reflection coefficient should increase. Reflection is related to the relative steepness of the beach. The beach steepness can be normalized with the wavelength for a relative steepness. Essentially, longer waves "see" a steeper beach so reflection increases with increasing wavelength. For the most part, this is seen in Figures 3-23 and 3-24, though the 1.08 Hz component in both figures and the 0.52 Hz component in Figure 3-24 do not obey this trend. Using the incident and reflected wave components, we can define a equivalent reflection coefficient for the experiment, which is shown in Figure 3-25 for the two beaches over time. The equivalent wave reflection coefficient is defined as

$$R_{eq} = \frac{a_{r,eq}}{a_{i,eq}} = \sqrt{\frac{\sum_{n=1}^{5} {a_{r,n}}^2}{\sum_{m=1}^{5} {a_{i,m}}^2}} \tag{3.17}$$

Figure 3-25 shows the dune having a higher reflection coefficient than the sea wall. The dune reflection coefficient is consistently greater than the sea wall coefficient throughout the experiments. The equivalent periods are given by (2.18). The variation in wave height between the beaches is less than 10% and not consistently greater for either side. In contrast, the reflection coefficient for the sea wall is consistently 0.05 to 0.1 less than it is for the dune throughout the experiment.

Rather than show the $T_{eq,nom} = 1$ s and $T_{eq,nom} = 2$ s in full detail, we will show the equivalent wave height and reflection coefficients for these cases without showing the results by component. Figure 3-26 shows the incident equivalent wave heights and Figure 3-27 shows the equivalent reflection coefficients for the 1 s wave case. The nominal conditions for the wave were $T_{eq,nom} = 1$ s and $H_{eq,nom} = 7.1$ cm for 30 minutes. The equivalent wave heights are very constant during the wave set and equivalent for the two beaches. Again, the equivalent reflection coefficients show greater reflection on the dune side, consistant

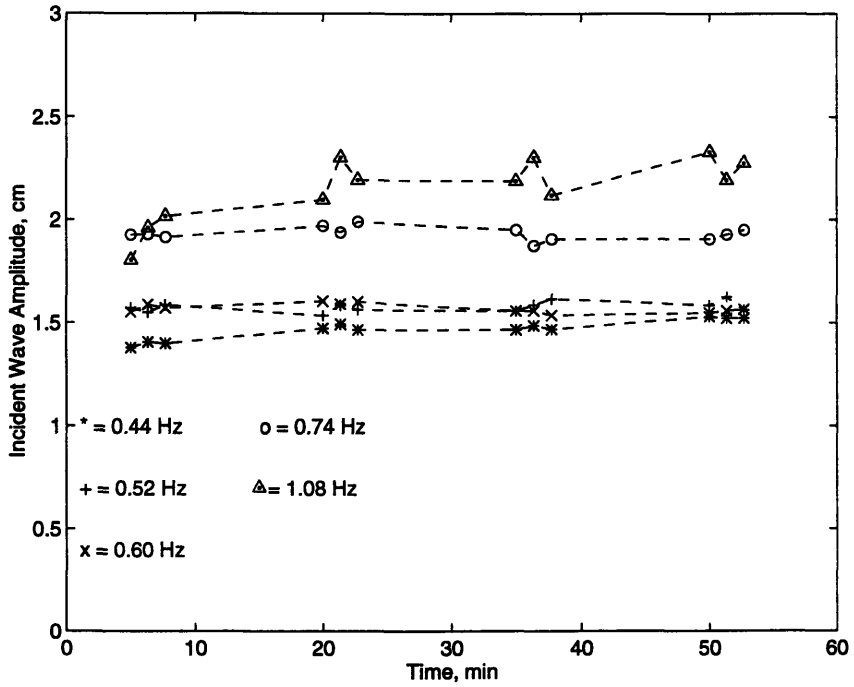


Figure 3-20: Incident ampiltudes by spectral wave component on the dune beach for a $T_{eq,nom} = 1.5$ s, $H_{eq,nom} = 8.0$ cm wave.

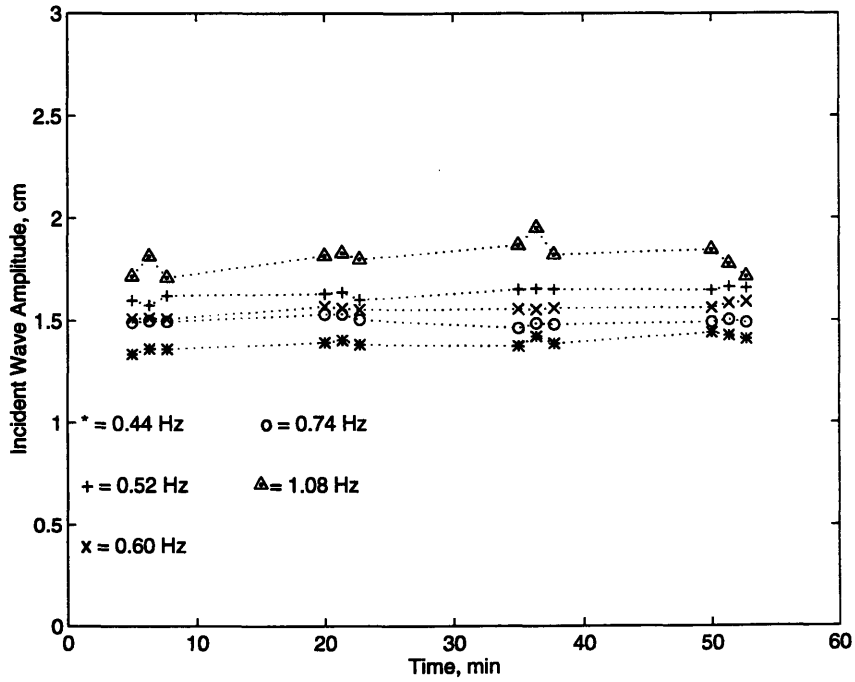


Figure 3-21: Incident ampiltudes by spectral wave component on the sea wall beach for a $T_{eq,nom} = 1.5$ s, $H_{eq,nom} = 8.0$ cm wave.

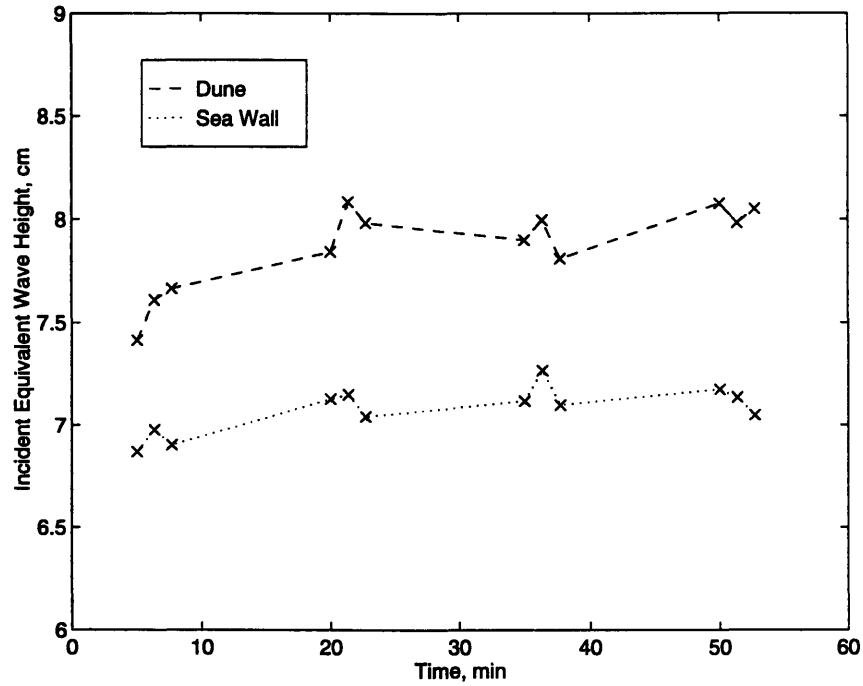


Figure 3-22: Equivalent incident wave heights on the dune and on the sea wall for a $T_{eq,nom} = 1.5$ s, $H_{eq,nom} = 8.0$ cm wave.

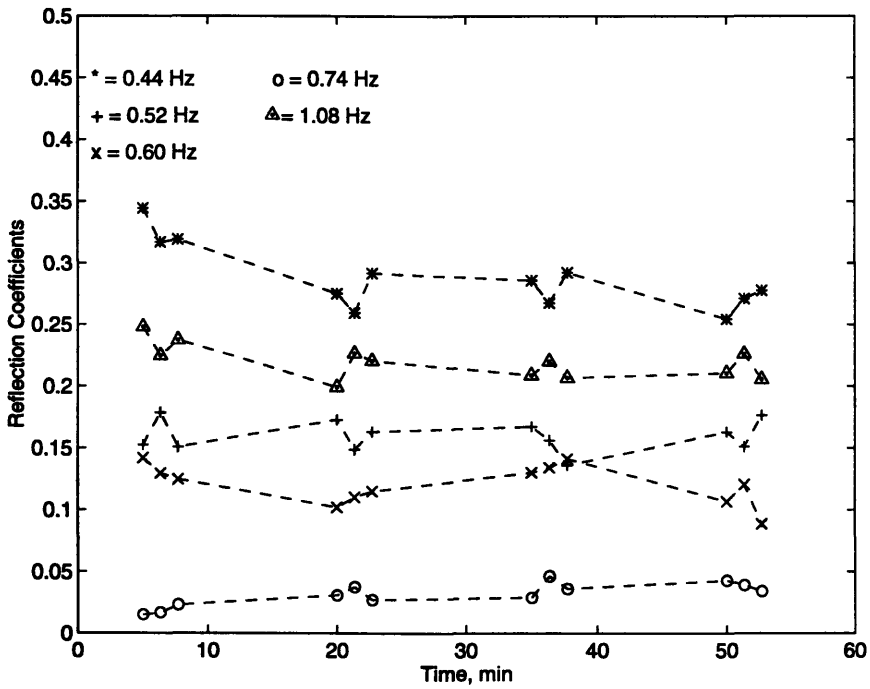


Figure 3-23: Reflection coefficients by spectral wave component on the dune beach for a $T_{eq} = 1.5$ s, $H_{eq} = 8.0$ cm wave.

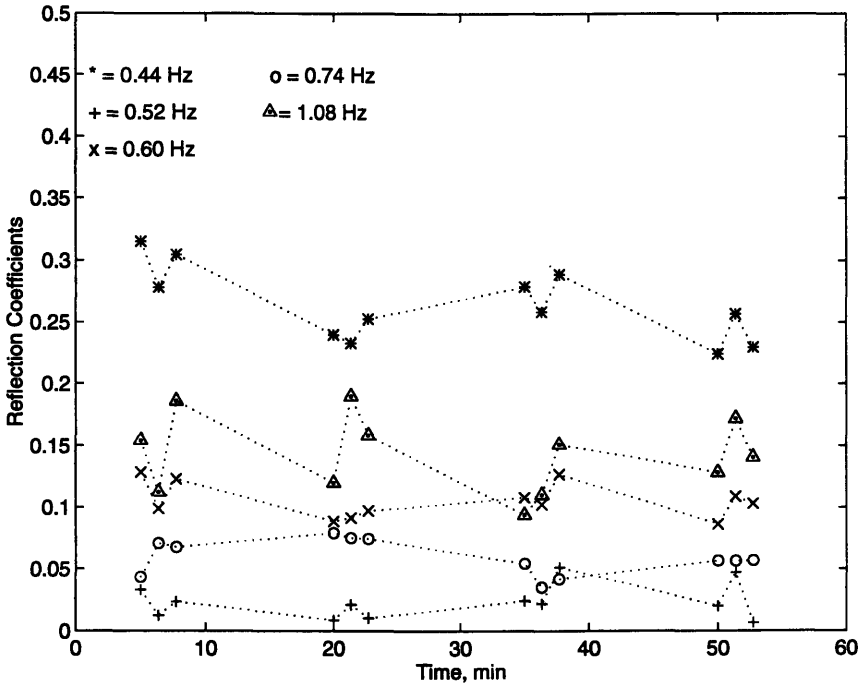


Figure 3-24: Reflection coefficients by spectral wave component on the sea wall beach for a $T_{eq} = 1.5$ s, $H_{eq} = 8.0$ cm wave.

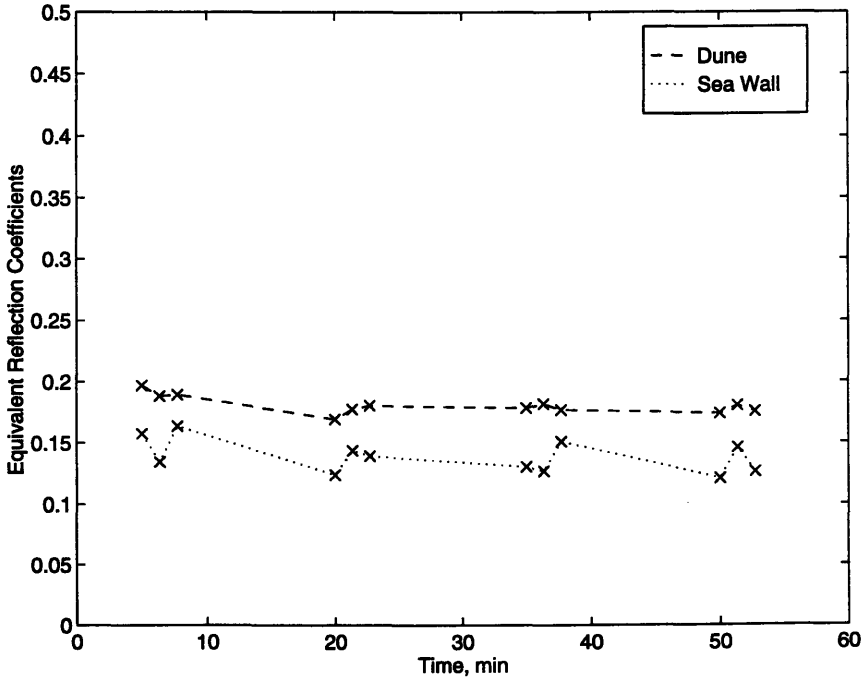


Figure 3-25: Equivalent reflection coefficients on the dune and on the sea wall for a $T_{eq} = 1.5$ s, $H_{eq} = 8.0$ cm wave.

with the results for the 1.5 s wave case. The results for a $T_{eq,nom} = 2$ s, $H_{eq,nom} = 5.4$ cm waves for 30 minutes are shown as equivalent wave heights in Figure 3-28 and as equivalent reflection coefficients in Figure 3-29. There is some temporal variation in the incident wave conditions, both the dune and sea wall incident wave heights start about 4.8 cm and end about 5.3 cm, with the two conditions following each other closely. The reflection coefficients fit the patterns of higher reflection on the dune and of higher reflection for longer waves.

This section shows the variability of the measured wave conditions during the experiment. For the rest of the paper, the equivalent wave period, wave height and reflection coefficient are given to represent the wave conditions. Unless otherwise noted, the variation in wave conditions over time and between beaches is of the same order of magnitude, i. e. of the order 10%, as the variation in wave conditions shown above.

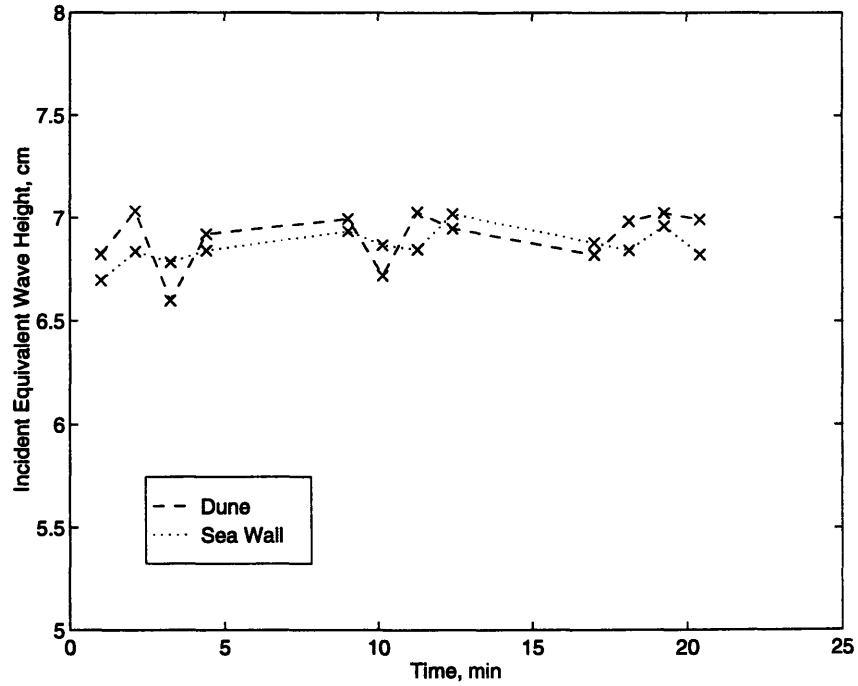


Figure 3-26: Equivalent incident wave heights on the dune and on the sea wall for a $T_{eq,nom} = 1.0$ s, $H_{eq,nom} = 7.1$ cm wave.

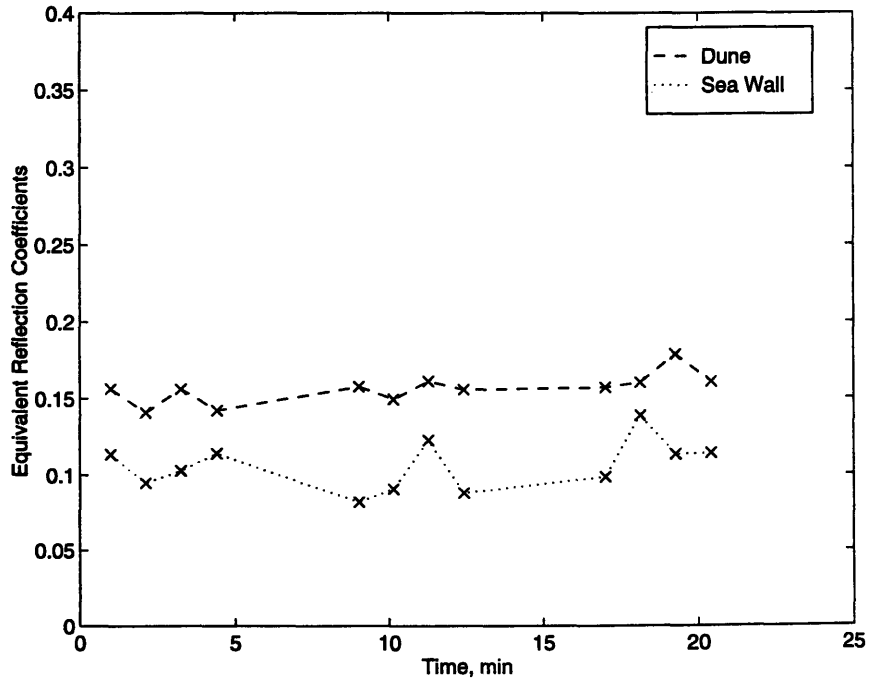


Figure 3-27: Equivalent reflection coefficients on the dune and on the sea wall for a $T_{eq} = 1.0$ s, $H_{eq} = 7.1$ cm wave.

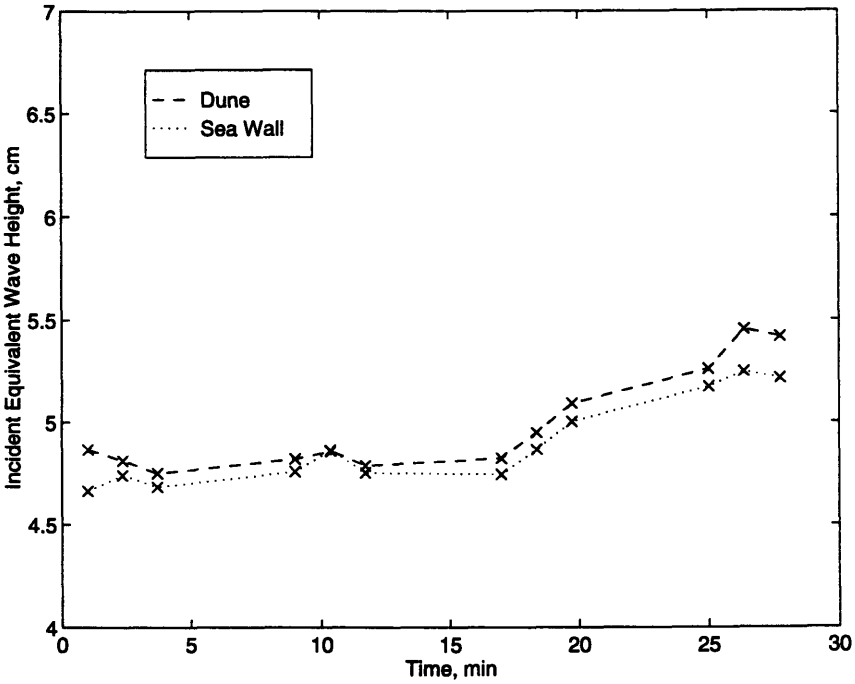


Figure 3-28: Equivalent incident wave heights on the dune and on the sea wall for a $T_{eq,nom} = 2.0$ s, $H_{eq,nom} = 5.4$ cm wave.

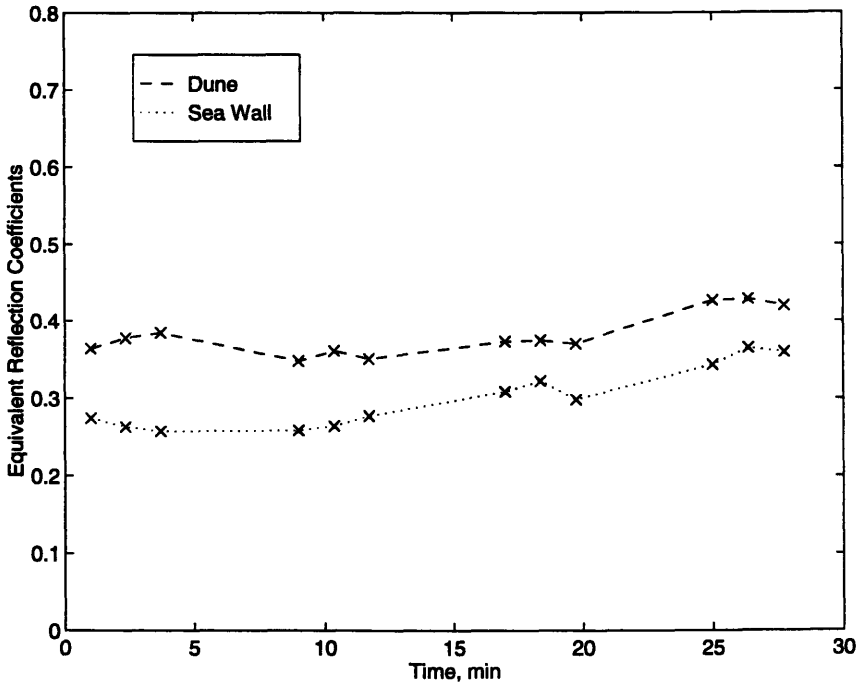


Figure 3-29: Equivalent reflection coefficients on the dune and on the sea wall for a $T_{eq} = 2.0$ s, $H_{eq} = 5.4$ cm wave.

# Chapter 4

# Experimental Results

This experiment was designed to look at how waves interact with sea walls compared to how they interact with dunes. To study this, we conducted several experiments with normally incident waves in a 4 meter wide section of our wave basin. The wave basin has the capability to generate oblique waves, but these were not used in this investigation due to space and time constraints. Within the section, there were two beaches. One beach had a rubble mound sea wall made of gravel and the other was unprotected, as discussed in Section 3.1. We conducted several experiments with the beaches separated by a dividing wall to simulate a sea wall and a dune without edge effects. Following this, the dividing wall was removed and additional experiments were conducted to study the edge effects.

Several different experiments were conducted to see how the beaches would respond under varying wave conditions. One of the initial studies looked at the difference in beach response for multi-component spectral waves and the equivalent monochromatic wave. The next experiments varied the wave conditions to determine if the two beaches had the same erosion criteria and if they eroded and accreted at the same rate. The beaches were also subjected to a simulated storm surge erosion with a subsequent recovery to determine if water level changes affected the beaches differently. After the dividing wall was removed we examined the interaction between the protected and unprotected beaches. Finally, we looked at the edge effects during a storm surge experiment with extensive erosion.

## 4.1 The Equilibrium Profile

In order to compare different experiments, we needed to start the experiments from the same or at least very similar, initial profiles. To reset the beaches to the same initial profile before each experimental iteration by hand would be tedious. Fortunately we did not have to. Early in the study, when we were testing the system, we noticed that accretional waves formed a very repeatable profile, which we refer to as the equilibrium profile. When this equilibrium profile is eroded, it recovers to nearly the identical profile when subjected to "standard" accretional waves. Both beaches are returned to their original state after running these accretional waves for a certain duration. Empirically, this time was found to be of the order of 30 minutes for limited erosion events, and longer for more extensive erosion using a "standard" accretional wave with a nominal period of 2 seconds and wave height of 5.4 cm. Two experiments demonstrating this equilibrium beach profile are given below.

The first experiment is for a limited erosional event. The initial profiles for the dune and sea wall are shown in Figure 4-1. Each profile shown is the elevation averaged over twelve equally spaced transects in the longshore direction. The beach measurement procedure is given in Section 3.3.1. The longshore variability is discussed in Section 4.2 which compares monochromatic and spectral wave conditions. For spectral wave conditions, the beaches were very uniform in the longshore direction, so the beach is well represented by an averaged profile. This "initial" profile is the post recovery profile from a previous experiment and was generated using the standard accretional waves mentioned above. The beach was then eroded for 25 minutes with a spectral wave with an equivalent wave height of 5.9 cm and an equivalent period of 1.06 seconds. The resulting beach profiles are shown in Figure 4-2. Since it is difficult to see the erosion on two plots, the eroded dune profile and the initial dune profile are given in Figure 4-3. This figure shows how much sand has been eroded from the dune and moved offshore to form a berm. The volume of sand eroded equals the volume of sand deposited within 5% of the volume of sand transported. This was calculated by dividing the total deposition minus the total erosion by the total deposition.

After the beach was eroded and measured, it was recovered with accretional waves for 25 minutes by a $T_{eq} = 2.08$ s, $H_{eq} = 5.0$ cm wave. The recovered profile is given in Figure 4-4. What should be noticed in the series of figures is that the two beaches, protected and unprotected, are very similar before erosion, after erosion and after recovery. Figure

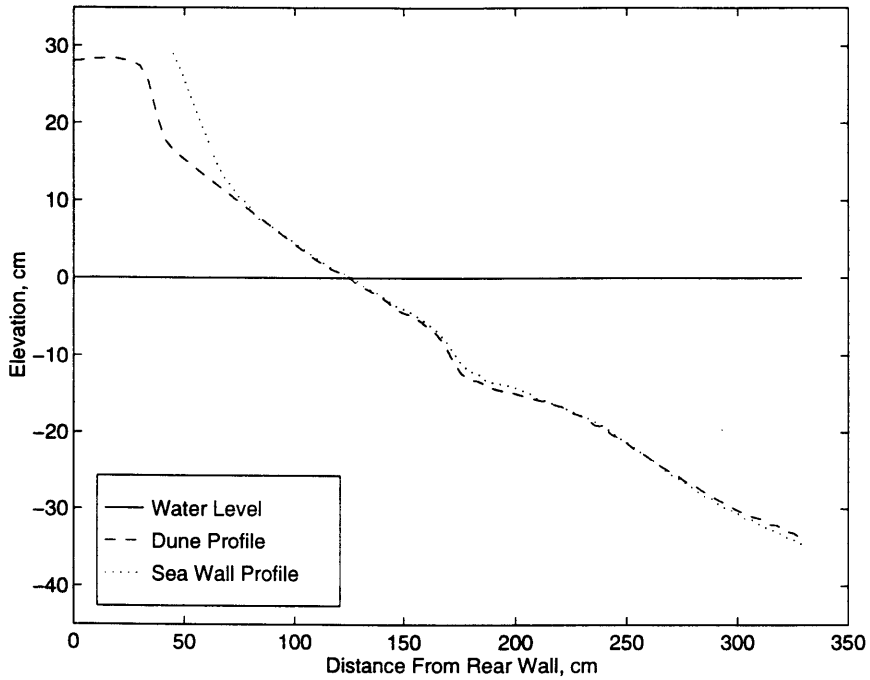


Figure 4-1: Averaged profiles of beaches before erosion by $T_{eq} = 1.06$ s, $H_{eq} = 5.9$ cm waves for 25 minutes.

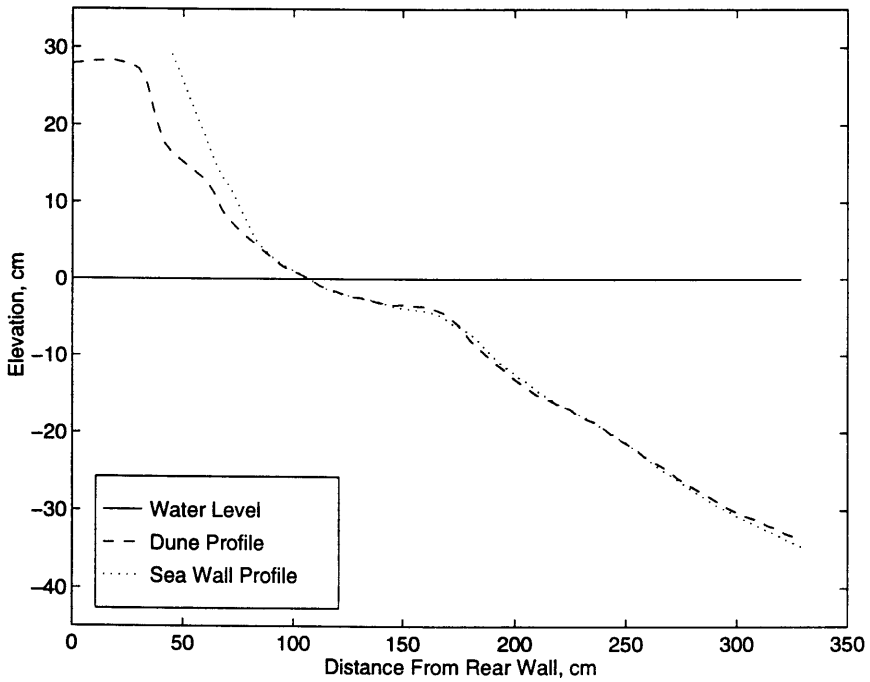


Figure 4-2: Averaged profiles of beaches shown in Figure 4-1 after erosion by $T_{eq} = 1.06$ s, $H_{eq} = 5.9$ cm waves for 25 minutes.

4-5 shows the average dune transects before erosion and after recovery. The two lines fall almost exactly on top of each other.

Another way to demonstrate that there was significant erosion and recovery is to plot the difference between two profiles. The maximum erosion and the net change for the beaches are shown in Figure 4-6. This figure has two plots, both following the convention of a dashed line for the dune profile and a dotted line for the sea wall profile. The top plot shows the extent of erosion by the $T_{eq} = 1.06$ s, $H_{eq} = 5.9$ cm waves. The plot was constructed by subtracting the initial profile in Figure 4-1 from the eroded profile in Figure 4-2. The bottom plot shows the net change from the initial profile to the final profile and was constructed by subtracting the initial profile, Figure 4-1, from the final profile, Figure 4-4. What should be noted in Figure 4-6 is that the magnitude of erosion and offshore deposition is very similar for both beaches. The dune eroded further than the sea wall because the waves could not dig into the sea wall. This excess erosion is balanced by the excess deposition in the offshore region between 150 and 175 cm. In the bottom plot, the net change after recovery is negligible for both profiles, demonstrating the validity of the equilibrium profile concept and the lack of a directly measurable sea wall effect.

The experiment described above had a relatively small erosional event. For an extensive erosional event there is some permanent offshore loss of sand that cannot be recovered with accretional waves. After extensive erosion, the beaches take longer to recover, but they eventually do recover in the nearshore region. The second experiment is with extensive erosion followed by recovery. Figure 4-7 shows the equilibrium beaches after recovery from a previous experiment and before a period of extensive erosion. The wave conditions for the extensive erosion sequence are given in Table 4.1 with the erosional events marked with an "E" and the accretional events with an "A". After each wave event, the beach was measured.

Figure 4-8 shows the beaches after over 4 hours of erosion, culminating with an hour of spectral waves with an equivalent period of 1.40 seconds and wave height of 7.5 cm. The intermediate beach conditions were measured, but are not given here. What should be noted in Figure 4-8 is how far the two beaches have eroded after over 4 hours of pounding by large waves. The beaches show more deviation here due to the greater erosion and offshore deposition on the dune beach than on the protected beach, which makes sense. The dune side has more sand accessible to the waves, therefore more sand will be moved into the offshore bar. However, in the nearshore region, the two beaches still have very

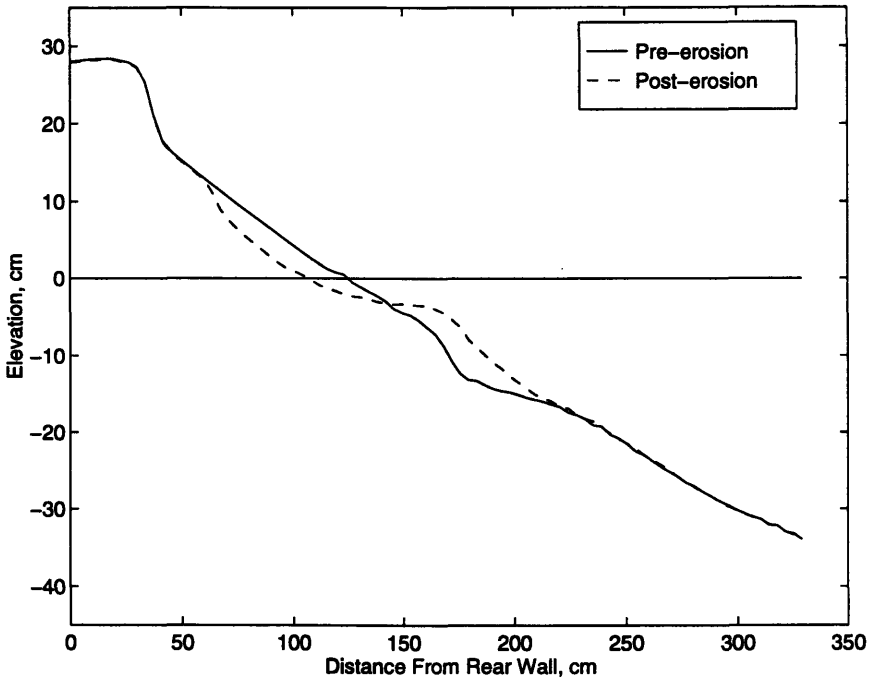


Figure 4-3: Averaged transects of dune profile before and after erosion by $T_{eq}$ = 1.06 s, $H_{eq}$ = 5.9 cm waves.

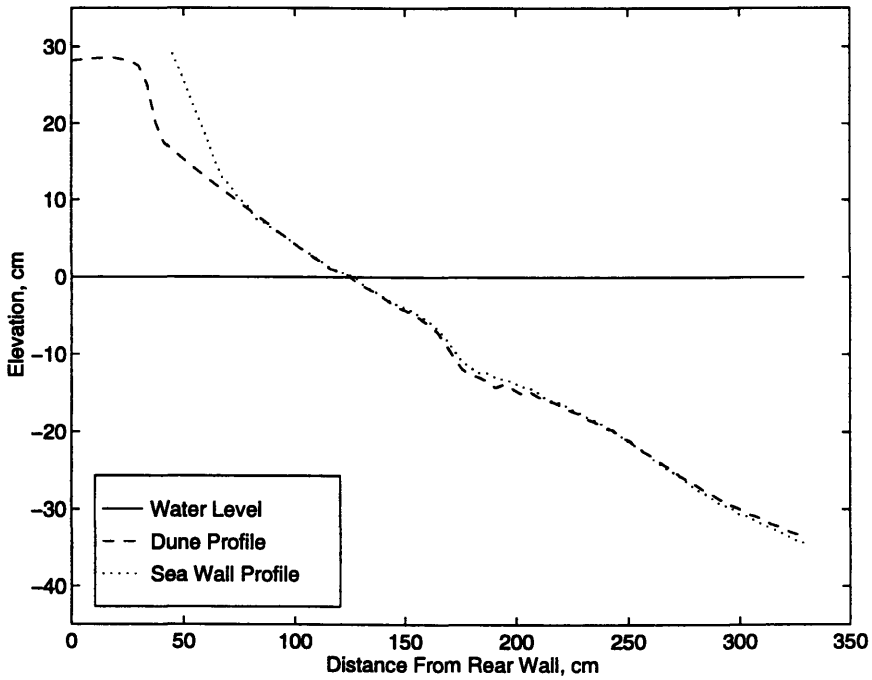


Figure 4-4: Averaged profiles of beaches shown in Figure 4-2 after recovery by $T_{eq}$ = 2.08 s, $H_{eq}$ = 5.0 cm waves for 25 minutes.

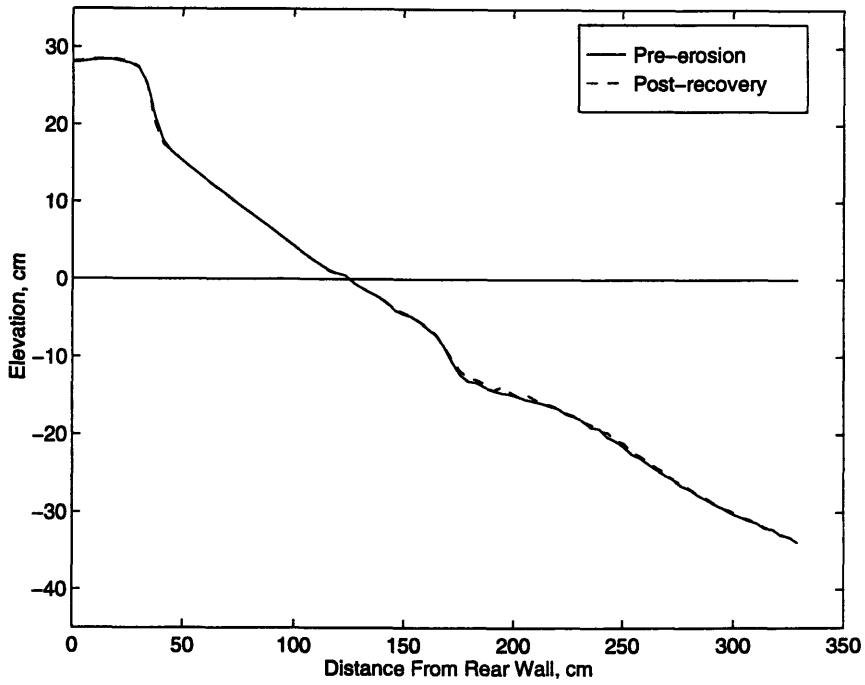


Figure 4-5: Averaged profiles of the dune beach before erosion, from Figure 4-1, and after recovery, from Figure 4-4.

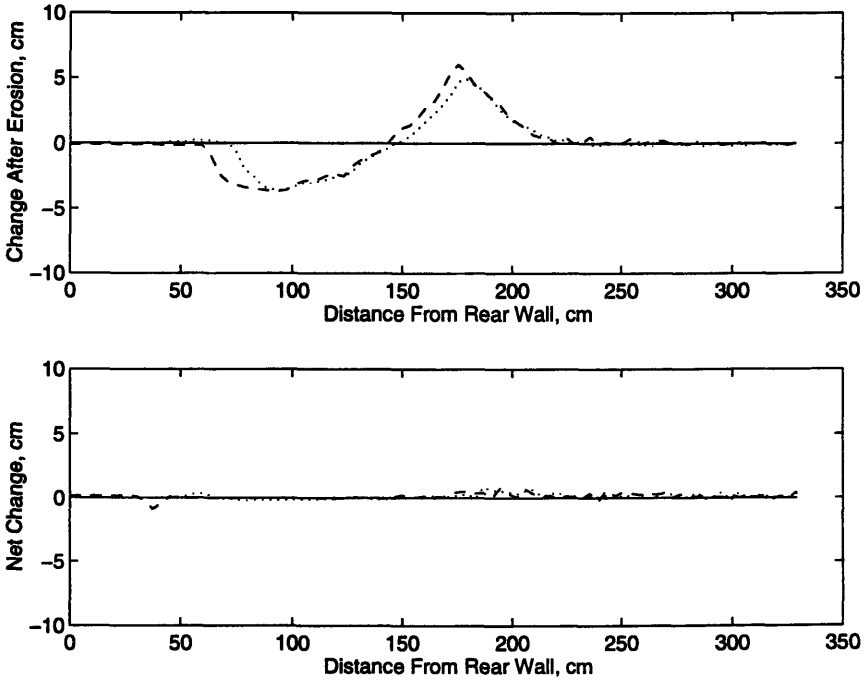


Figure 4-6: Maximum profile change due to erosion, Figure 4-2 minus Figure 4-1, and net profile change after recovery, Figure 4-4 minus Figure 4-1. (- - -) Dune, (...) Sea wall.

Table 4.1: Equivalent wave conditions for extensive erosion case.

| $T_{eq}$, (s) | $H_{eq}$, (cm) | Duration, (min) | E or A |
|---|---|---|---|
| 1.41 | 6.0 | 7.5 | E |
| 1.40 | 6.3 | 15 | E |
| 1.08 | 6.3 | 15 | E |
| 1.38 | 6.3 | 30 | E |
| 1.08 | 6.8 | 30 | E |
| 1.09 | 6.8 | 30 | E |
| 1.37 | 6.8 | 30 | E |
| 1.37 | 7.5 | 30 | E |
| 1.40 | 7.5 | 60 | E |
| 1.87 | 5.0 | 30 | A |
| 2.02 | 5.3 | 60 | A |

similar profiles.

The beaches were recovered by the accretional wave conditions shown in Table 4.1 and the recovered condition is shown in Figure 4-9. Again, the recovered profiles show very good agreement, especially in the region near the waterline, from about 75 to 160 cm from the rear wall. The recovered profile has the same slope and shape as the initial profile, so it is an equilibrium profile, as defined above. What is interesting though is the maximum and net erosion shown in Figure 4-10. Again, this is a double plot with the top plot showing the maximum erosion, obtained by subtracting Figure 4-7 from Figure 4-8, and the bottom plot showing the net erosion, obtained by subtracting Figure 4-7 from Figure 4-9. The dashed line is for the dune and the dotted is for the sea wall. The maximum erosion plot is qualitatively very similar to the maximum erosion plot given in Figure 4-6 for the limited erosion event, but the magnitude of erosion is much greater. In terms of net change, however, the two experiments differ. In the limited erosion case, the profile recovered to almost the initial profile, but after the extensive erosion sequence the recovery is not complete. There is some permanent sand loss from the dune to far offshore. The 6 cm erosion at 25 cm from the rear wall is the sand lost from the dune which has been deposited offshore in the region from 225 to 300 cm from the rear wall. The sand volume eroded equals the sand volume deposited within 11% for erosion and within 6% for erosion and recovery.

One might reasonably wonder, as we later did, whether 90 minutes of accretion is sufficient to consider the sand permanently lost since Figure 4-10 shows a small net erosion

from about 50 cm to 150 cm for both the dune and the sea wall beaches. In an experiment shown in Section 4.5, the beaches are subjected to a similar extensive erosion sequence and then recovered for 4 hours to see if there was a limit to the beaches' ability to recover or if the beach continued to recover at a slow rate. This experiment showed that even after extensive erosion, the majority of the beach recovery occurred in the first 60 minutes. Additional recovery after the first 60 minutes was negligible, so we are confident that the beach shown in Figure 4-9 is fully recovered.

These two experiments show that the beaches have an equilibrium profile that is reached when subjected to accretional waves, even after a case of extensive erosion. After extensive erosion, there may be a permanent beach change, but this change is evident for both the dune and the sea wall beaches. This shows the lack of a demonstrable sea wall effect. This section shows that the recovered beach is a consistent initial profile that can be used as a reference between experiments.

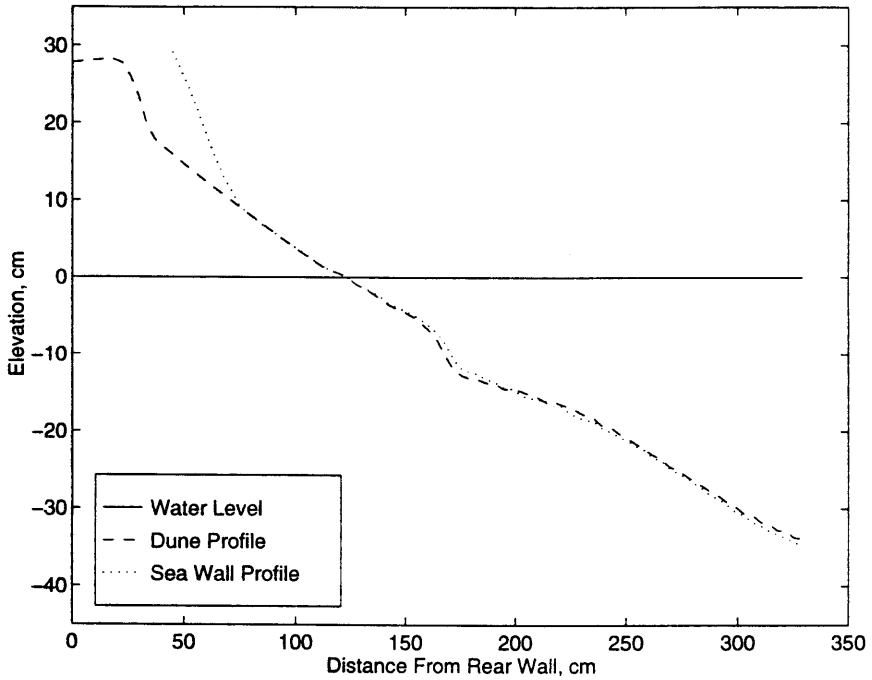


Figure 4-7: Profiles of beaches showing equilibrium profile before extensive erosion.

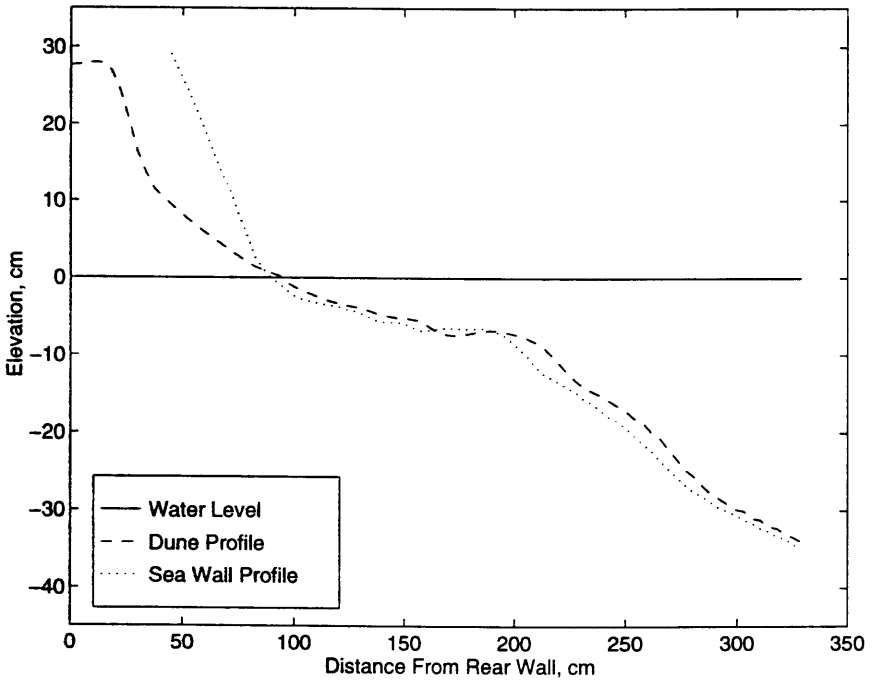


Figure 4-8: Profiles of beaches shown in Figure 4-7 shown after extensive erosion by the wave conditions listed in Table 4.1.

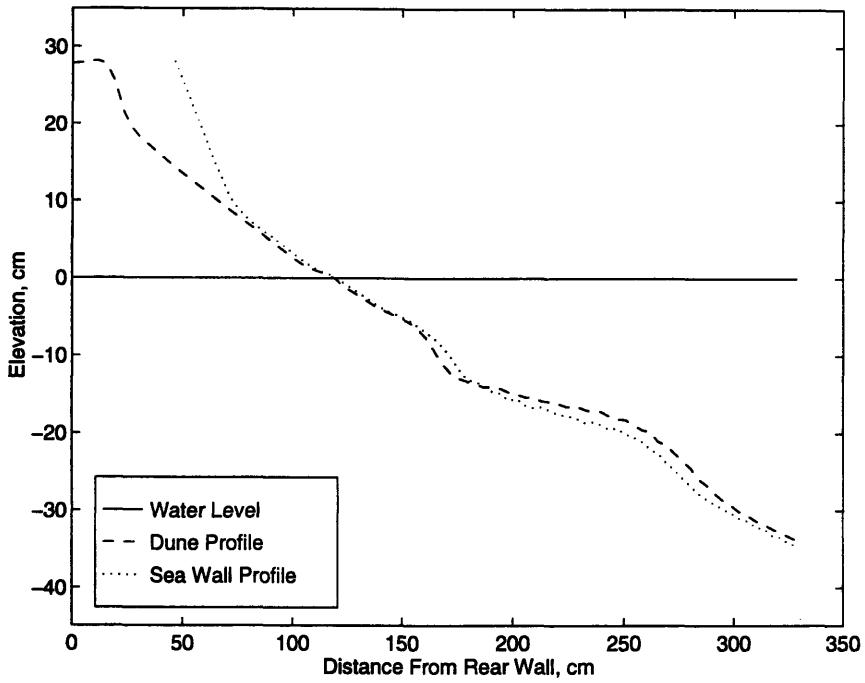


Figure 4-9: Beaches after recovery by the accretional waves in Table 4.1 from the profile shown in Figure 4-8.

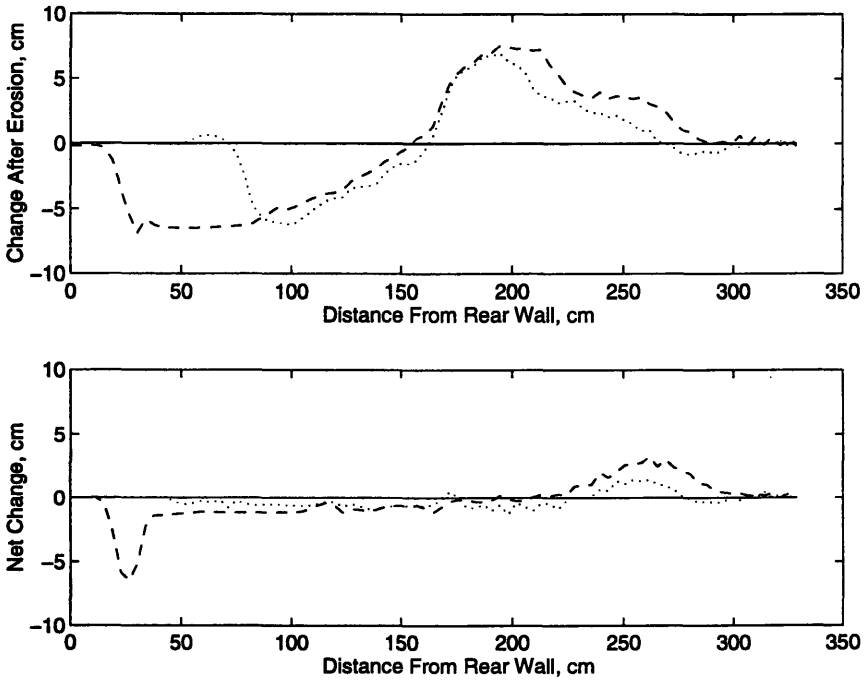


Figure 4-10: Maximum profile change due to erosion, Figure 4-8 minus Figure 4-7 and net profile change after recovery, Figure 4-9 minus Figure 4-7. (- - -) Dune, (...) Sea wall.

## 4.2 Monochromatic and Spectral Waves

One of the initial experiments that we ran compared the beach response to monochromatic waves with the response to spectral waves. Irie and Nadaoka (1985) show that irregular waves are superior to regular waves in reproducing prototype conditions during laboratory studies. We conducted two wave sequences to compare spectral and monochromatic waves. The sequences consisted of a spectral wave erosion and recovery followed by a monochromatic wave erosion and recovery. The monochromatic waves had the same equivalent period, wave height and duration as the spectral waves. The experiments were to validate the need for spectral waves and to test the experimental setup.

When computing the monochromatic wave condition, we used the design wave condition, not the measured wave condition. For instance, the first experiment has a five component spectral wave with each component having an amplitude of 1.3 cm, which translates to an equivalent nominal wave height of 5.8 cm. The measured equivalent wave height was 5.9 cm for the spectral wave but instead of attempting to generate a 5.9 cm monochromatic wave, we programed the wave maker to generate a wave with a nominal wave height of 5.8 cm. The measured monochromatic wave had an height of 6.7 cm. The measured monochromatic deviates significantly from its nominal value whereas this is not the case for the spectral waves. Each component of the spectral wave has approximately the same magnitude of deviationg from its nominal value, but the deivations are spread over five frequencies and are positive for some and negative for others. Hence, the measured equivalent wave condition is much closer to the theoretical condition for spectral waves. With only one frequency present, the error does not get averaged and the equivalent wave has a larger apparent error. This phenomena is related to the effect of the rereflected waves fromt he wave paddle and is discussed in more detail in Section 3.5.2.

The main difference in the beach response between spectral and monochromatic waves is the longshore variability. Two different types of graphs are used to show the longshore variability on the beach. The first is with a profile view of the beach showing the average profile as a solid line with the average plus and minus one standard deviation of the longshore measurement plotted as a dashed line for the dune and as a dotted line for the sea wall. Essentially the result is an average profile with error bars. The initial profile for the first spectral and monochromatic wave sequence is given in Figure 4-11. This profile is after a

Table 4.2: Measured wave conditions during erosion for first spectral and monochromatic wave sequence.

| Wave condition | $T_{eq}$, (s) | $H_{eq}$, (cm) | Reflection coefficient |
|---|---|---|---|
| Spectral erosion | 1.05 | 5.9 | 0.14 |
| Monochromatic erosion | 1.02 | 6.7 | 0.08 |
| Spectral recovery | 2.08 | 5.0 | 0.41 |
| Monochromatic recovery | 2.04 | 5.4 | 0.35 |

spectral wave recovery, so it is an equilibrium profile as defined above. The plot is typical of the profiles generated by spectral waves in that it is very smooth and uniform in the region of wave activity as evidenced by the very small standard deviation from 50 to 200 cm from the back wall. The bed contains ripples beyond 200 cm, so the variability of the measurements is greater because one measurement could hit a ripple crest while the next one may hit the trough.

The second method to present the longshore variability is with a contour plot. Figure 4-12 shows the contour plot of the initial profile for the dune while Figure 4-13 shows the contour for the sea wall. Both plots have a 2 cm contour interval. The uniformity is demonstrated by the straightness of the contour lines, especially between the 10 cm and -10 cm contours. Again, the raggedness for the contours past 175 cm and below the $z = -10$ cm contour is due to the presence of the ripples.

Table 4.2 shows the equivalent wave conditions for the first sequence. The nominal wave conditions were erosion for 25 minutes by 1 s, 5.8 cm waves followed by accretion for 25 minutes by 2 s, 4.9 cm waves.

Figure 4-14 shows the profile plot of the beaches after spectral erosion by $T_{eq} = 1.05$ s, $H_{eq} = 5.9$ cm waves. The profiles are smooth with a gentle berm and with good longshore uniformity. This can be seen in the profile plot by the standard deviation lines which fall right on top of the average profile lines. The contour plot for the dune is given in Figure 4-15 and for the sea wall in Figure 4-16. The uniformity is excellent, with straight contour lines along the uniform profiles.

In contrast, the results for the monochromatic case are significantly different. The monochromatic erosion begins from a spectral recovered initial or equilibrium profile, so it has an equivalent initial condition to the spectral erosion case, i. e. corresponding to Figure

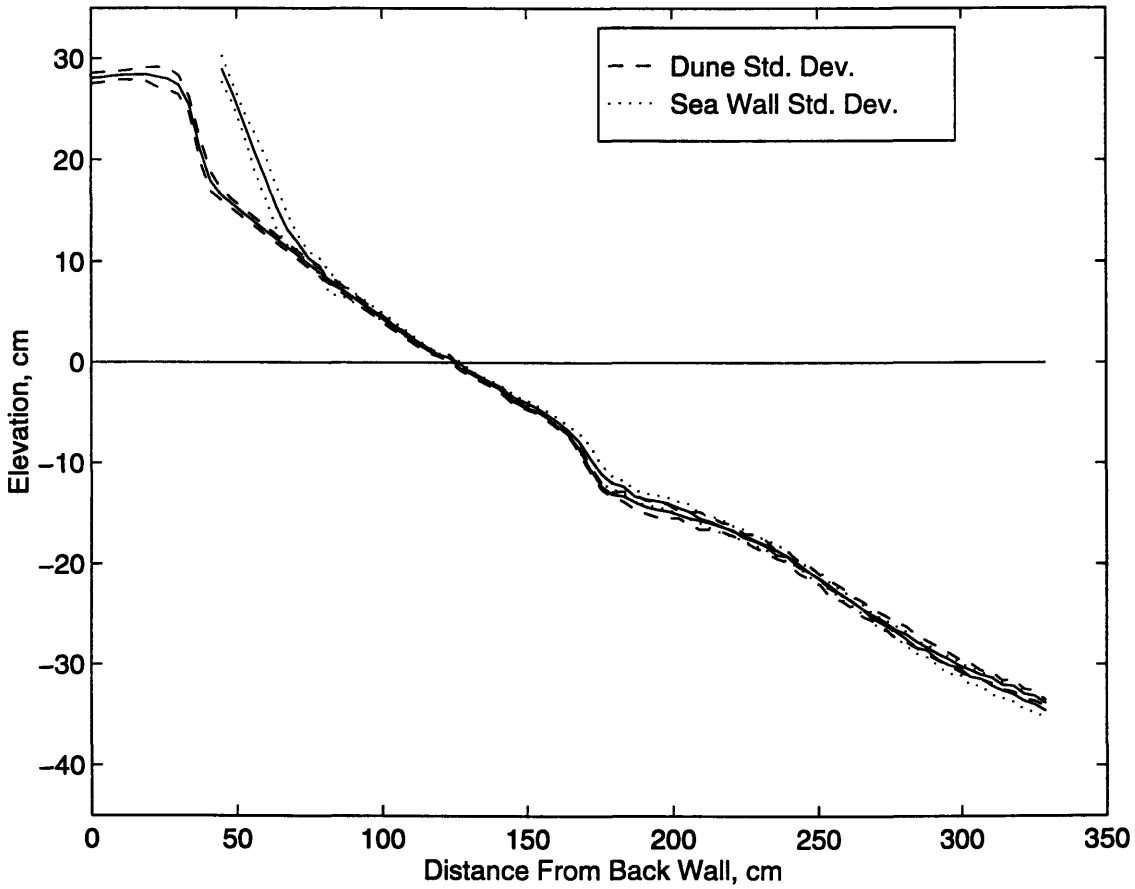


Figure 4-11: Initial profile for the spectral and monochromatic wave experiment showing the longshore variability as a standard deviation.

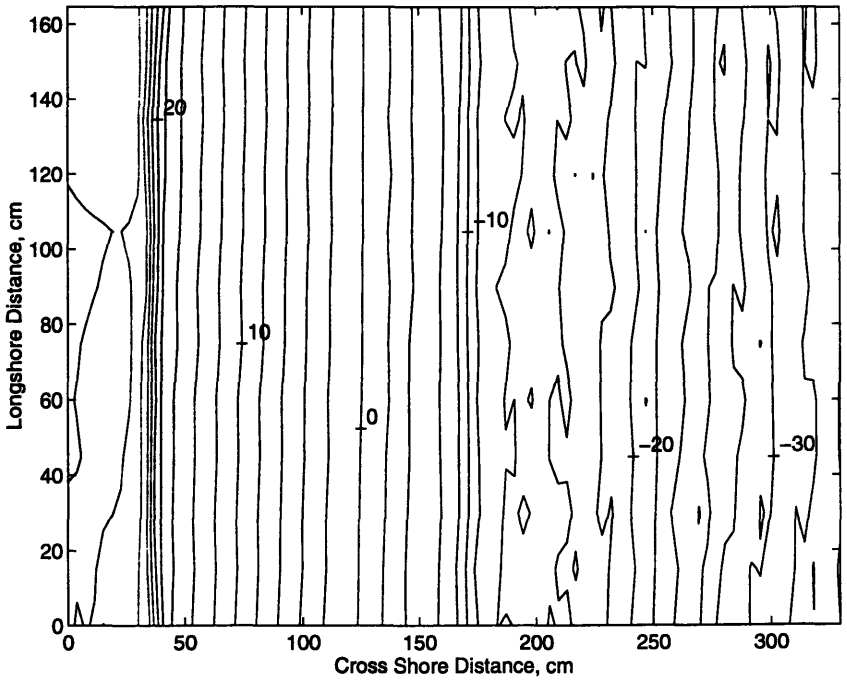


Figure 4-12: Contour plot of initial dune beach condition for the spectral and monochromatic wave experiment with a 2 cm contour.

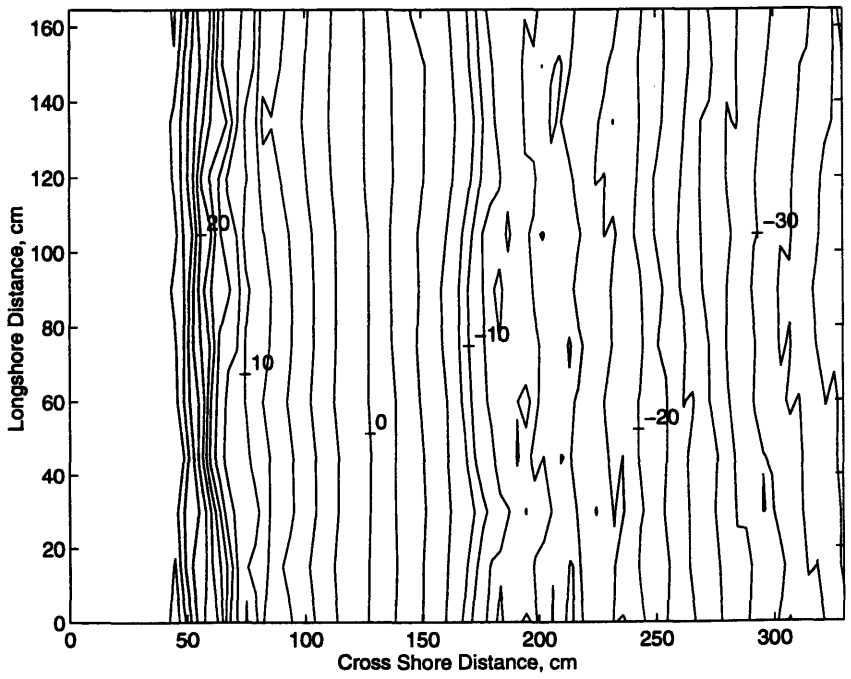


Figure 4-13: Contour plot of initial sea wall beach condition for the spectral and monochromatic wave experiment with a 2 cm contour.

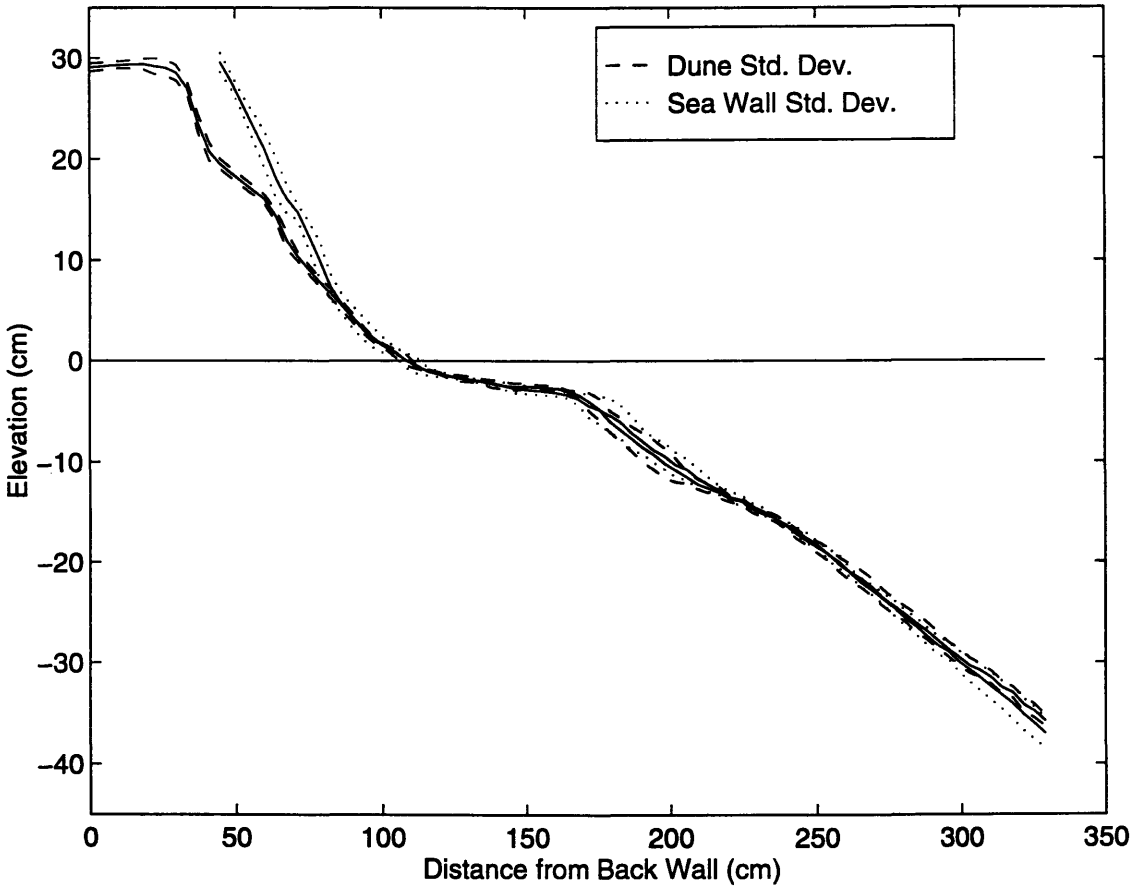


Figure 4-14: Profile after erosion from the profile in Figure 4-11 by spectral waves for 25 minutes with $T_{eq} = 1.05$ s and $H_{eq} = 5.9$ cm showing longshore variability.

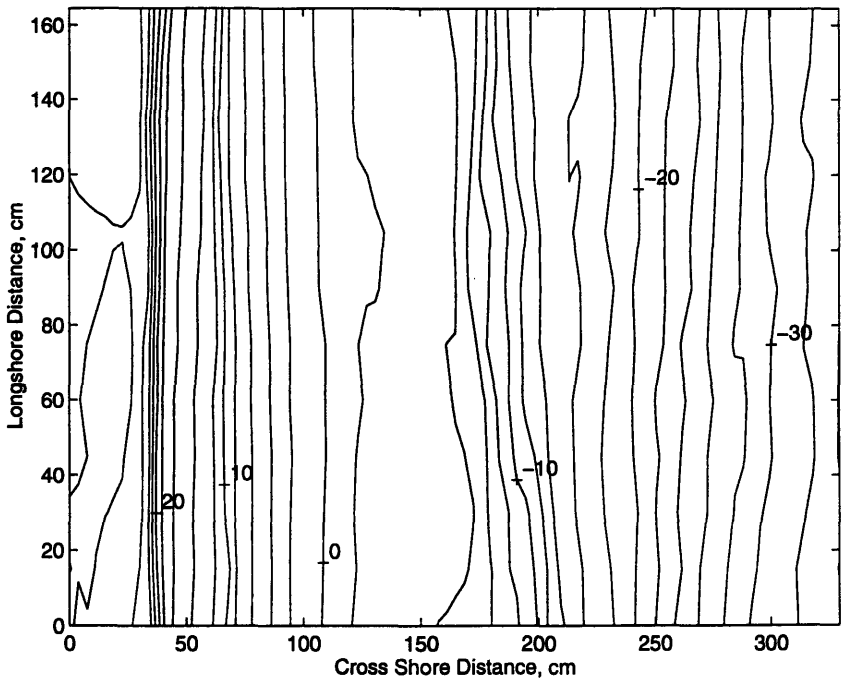


Figure 4-15: Contour plot of dune beach after erosion by spectral waves for 25 minutes with $T_{eq} = 1.05$ s and $H_{eq} = 5.9$ cm with a 2 cm contour.

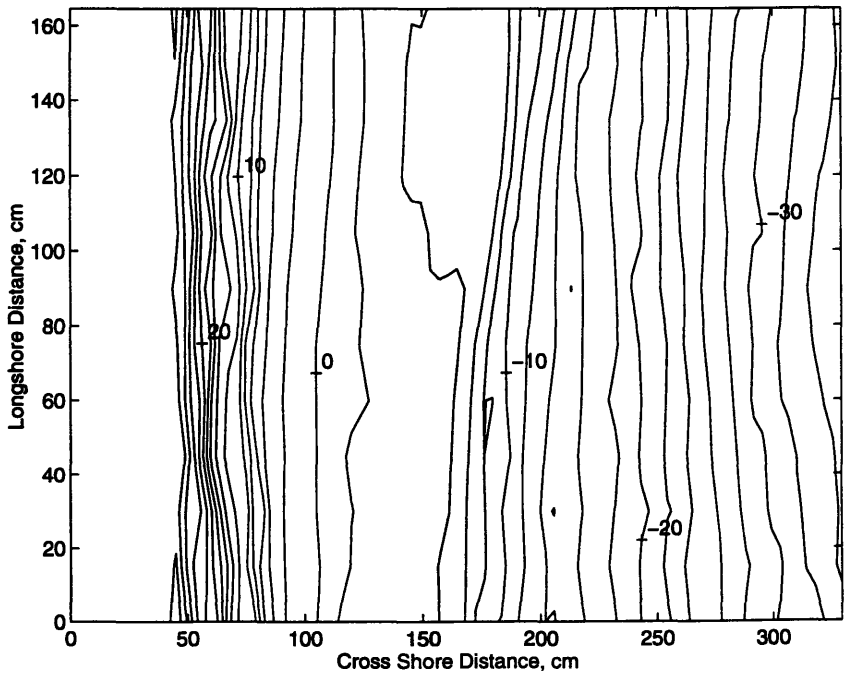


Figure 4-16: Contour plot of sea wall beach after erosion by spectral waves for 25 minutes with $T_{eq} = 1.05$ s and $H_{eq} = 5.9$ cm with a 2 cm contour.

4-11. The beach was eroded for 25 min with $T_{eq}$ = 1.02 s and $H_{eq}$ = 6.7 cm waves. The profile showing the longshore variability is given in Figure 4-17 while the contours of the dune and sea wall beaches are given in Figures 4-18 and 4-19.

The monochromatic erosion caused a sharp, crescent shaped berm to form offshore. The berm was highest at the center of the beach and tapered at the edges. The concentration of wave energy at one frequency caused the waves to hit in exactly the same location with each wave. With the energy focused that way, small local variations led to locally induced currents which in turn caused larger local variation. This process soon resulted in longshore non-uniformity and local circulation currents. The crescent shaped berm focused the wave energy on the center of the beach like a shoal focuses waves in the coastal zone, causing more erosion in the center than on the edges. The return currents were located at the edges of the beaches. The non-uniformity is evident by the standard deviation lines which do not stay close to the average profiles as shown in Figure 4-17. At some points the standard deviation is 2 or 3 cm rather than 2 or 3 mm as it is for the spectral erosion case. The comparatively sharp crested berm is shown in Figure 4-20 which is a single dune transect after spectral wave erosion plotted with a solid line and a single dune transect after monochromatic wave erosion plotted with a dashed line. This figure shows that the erosion caused by the monochromatic wave is more abrupt and that the berm created is sharper than in the spectral wave case.

The recovered beaches are shown in Figure 4-21 for the spectral recovery and in Figure 4-22 for the monochromatic recovery. The beaches that result from the spectral and monochromatic recoveries are much more similar than the beaches following erosion. The monochromatic waves produce a slightly greater variation in the longshore direction than the spectral waves, but it is not as noticeable as after the monochromatic erosion. Also, there is a small area that the monochromatic waves were not able to recover on the dune beach. This can be seen in Figure 4-22 near 55 cm from the back wall, where there is a small, but discernible, dip in the dune profile where the beach has not been brought back completely. This can be contrasted with the spectral recovered beach shown in Figure 4-21 which is fully recovered. To make this recovery deficiency clearer, Figure 4-23 shows the net change after erosion and recovery for both the spectral and monochromatic cases. Clearly, the region between 50 and 170 cm has recovered fully with spectral waves, but not with the equivalent monochromatic wave condition. It is possible that this defficiency could be due

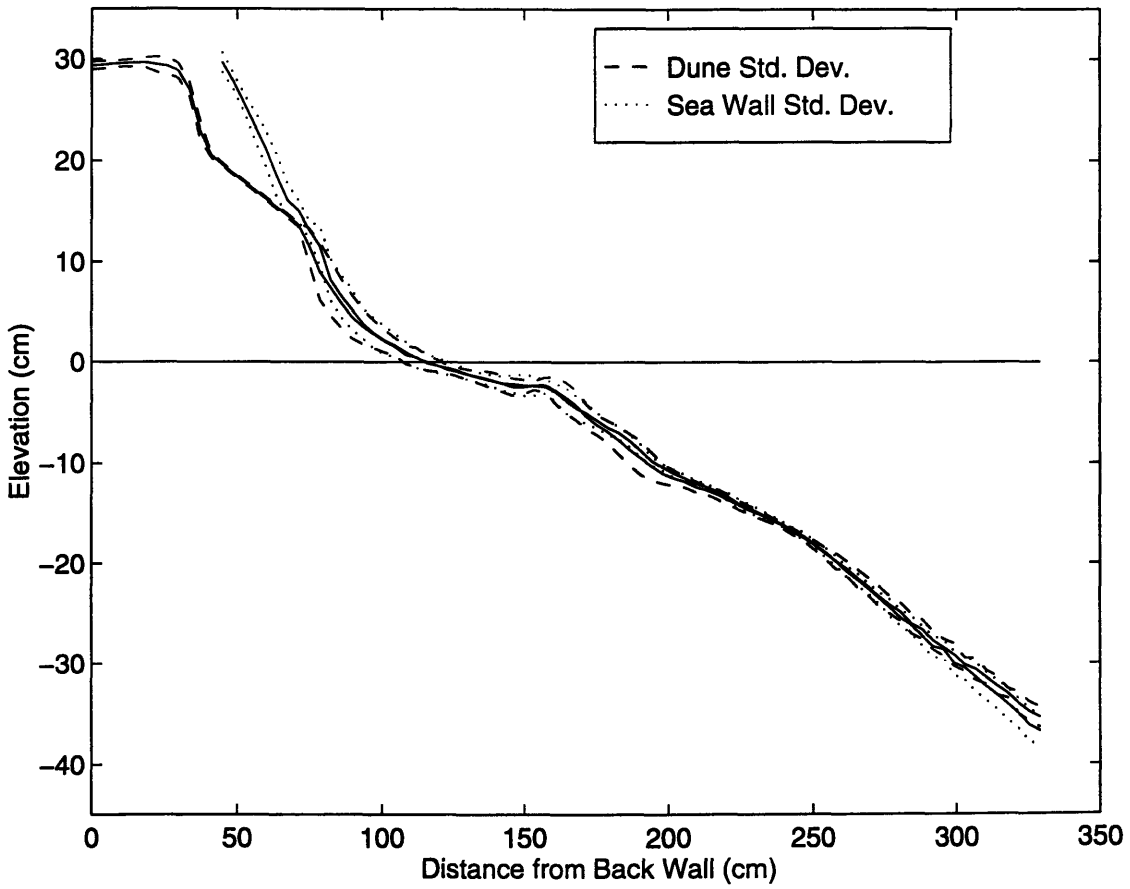


Figure 4-17: Eroded profile after 25 minutes of monochromatic waves with $T_{eq} = 1.02$ s and $H_{eq} = 6.7$ cm, showing longshore variability.

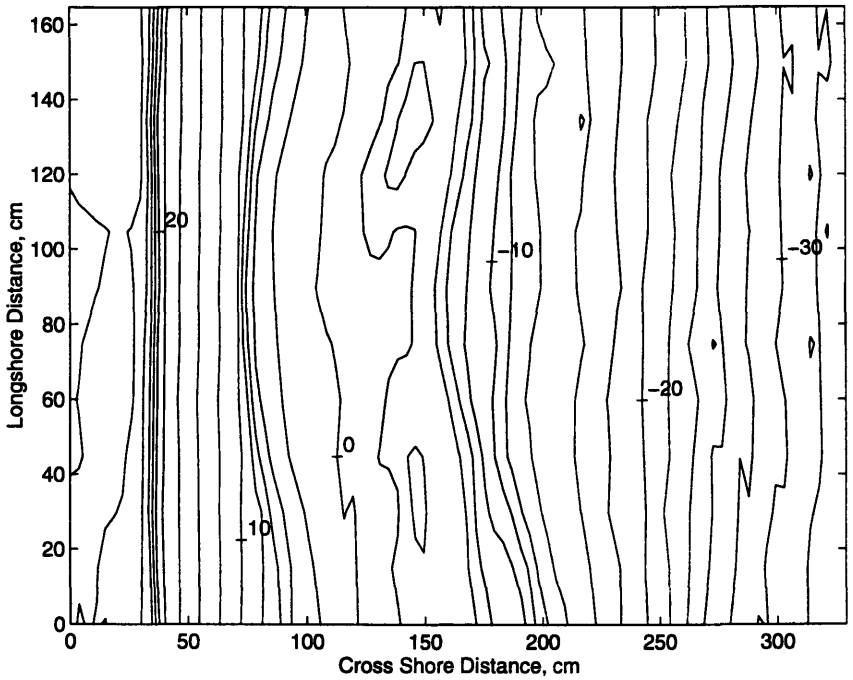


Figure 4-18: Contour plot of dune beach after 25 min of erosion by monochromatic waves with $T_{eq} = 1.02$ s and $H_{eq} = 6.7$ cm with a 2 cm contour.

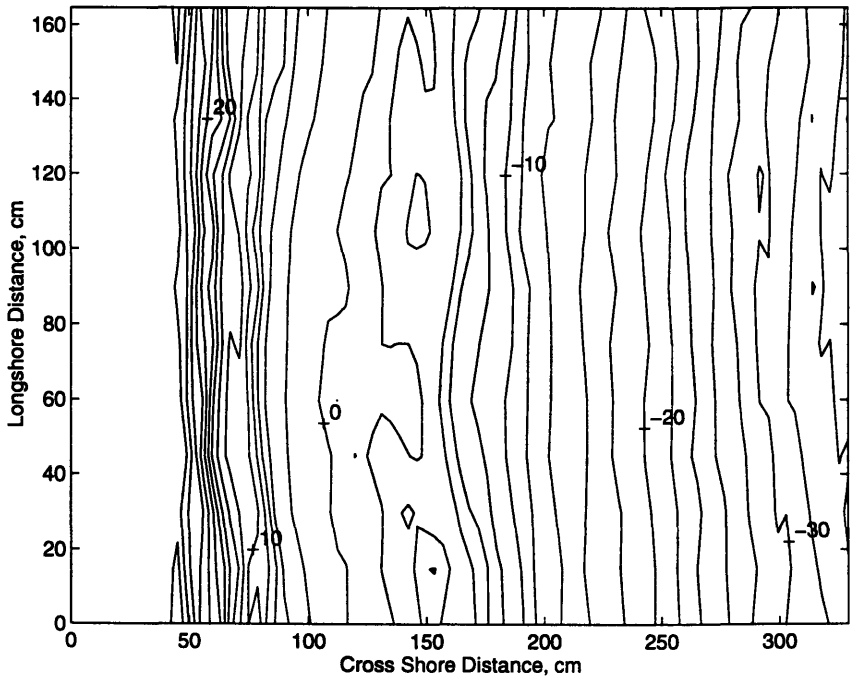


Figure 4-19: Contour plot of sea wall beach after 25 min of erosion by monochromatic waves with $T_{eq} = 1.02$ s and $H_{eq} = 6.7$ cm with a 2 cm contour.

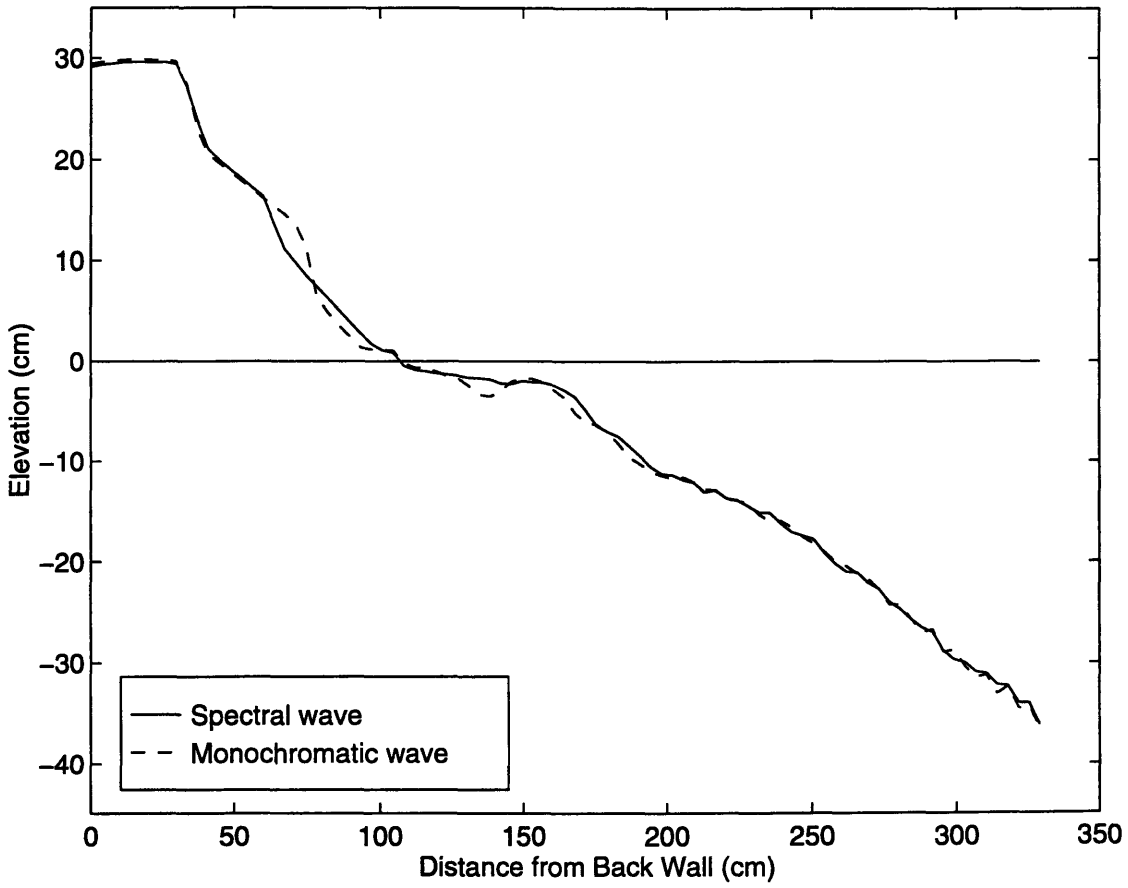


Figure 4-20: Individual transects from the dune beach after spectral erosion, from Figure 4-14 and monochromatic erosion, from Figure 4-17.

Table 4.3: Measured wave conditions during second spectral and monochromatic wave sequence.

| Wave condition | $T_{eq}$, s | $H_{eq}$, cm | Reflection coefficient |
|---|---|---|---|
| Spectral Erosion | 1.39 | 6.7 | 0.21 |
| Monochromatic Erosion | 1.54 | 7.5 | 0.17 |
| Spectral recovery | 2.13 | 5.6 | 0.46 |
| Monochromatic recovery | 2.04 | 6.8 | 0.29 |

in part to the larger incident wave height of the monochromatic wave. With a larger wave, there would be more erosion and it would take longer for the beach to recover.

The change in the beach condition can be plotted as a contour plot of beach change. Contours of the sand movement for spectral erosion on the dune are given in Figure 4-24 showing the reasonably uniform erosion and accretion over the entire beach. The negative contours show equal erosion and the positive contours show equal deposition. The $\Delta z = 0$ cm is not given because it detracts from the clarity of the plot. In contrast, when the change during monochromatic erosion is plotted as contour plots, the results are much less uniform. The dune beach change for the monochromatic erosion is given in Figure 4-25 and shows the focused localized erosion in the center of the beach.

The second spectral versus monochromatic experiment looked at erosion for 16.67 minutes by a nominal wave of 1.5 s and 6.7 cm followed by recovery for 25 minutes by a nominal wave of 2 s and 5.4 cm. The measured wave conditions are given in Table 4.3.

The results from the second sequence are very similar to the results from the first sequence. The eroded profile is worth examining though. Figures 4-26 and 4-27 contain the profile plots for the spectral erosion and monochromatic erosion, respectively. Again, the profiles from the spectral wave erosion are more uniform than the profiles for the monochromatic wave erosion and the berm that forms is more pronounced after the monochromatic erosion. What is interesting is the standard deviations for the 1.5 s, nominal, monochromatic waves are not as large as the standard deviations in the 1 s monochromatic case. As mentioned above, the monochromatic waves concentrate energy at a single frequency. If this frequency happens to be close to a natural frequency of the system, the system can demonstrate non-linear effects. The 2 s and the 1.5 s monochromatic waves do not produce beaches as smooth and uniform as their spectral counterparts, but they do produce beaches

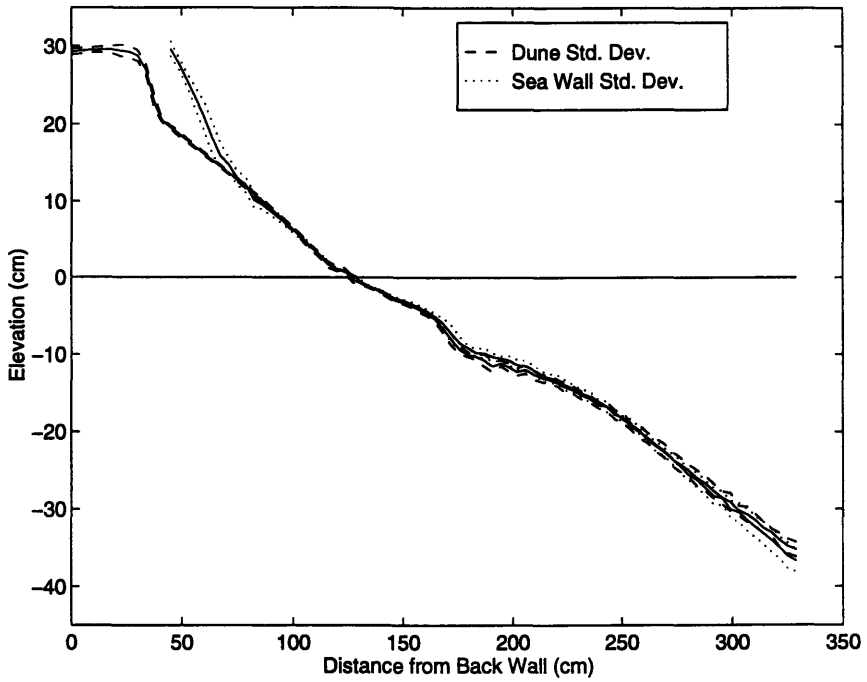


Figure 4-21: Profile after recovery from the condition in Figure 4-14 by spectral waves for 25 minutes with $T_{eq} = 2.08$ s and $H_{eq} = 5.0$ cm.

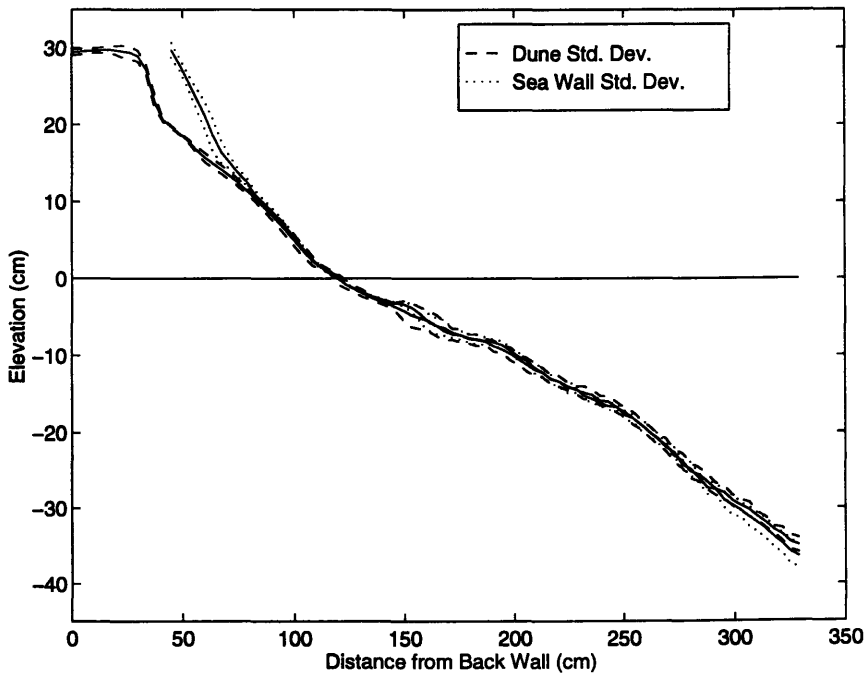


Figure 4-22: Profile after recovery from the condition in Figure 4-17 by monochromatic waves for 25 minutes with $T_{eq} = 2.04$ s and $H_{eq} = 5.4$ cm.

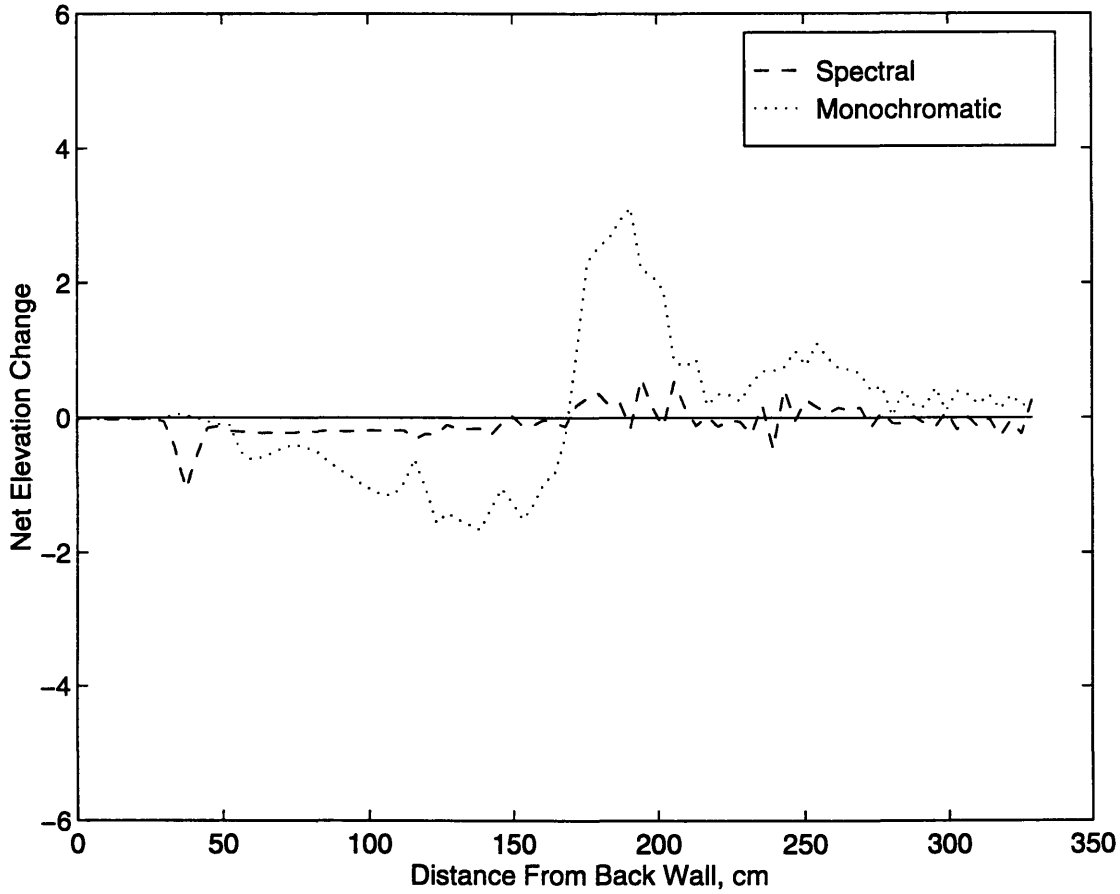


Figure 4-23: Net erosion for spectral waves, Figure 4-21 minus Figure 4-11, and net erosion for monochromatic waves, Figure 4-22 minus Figure 4-21.

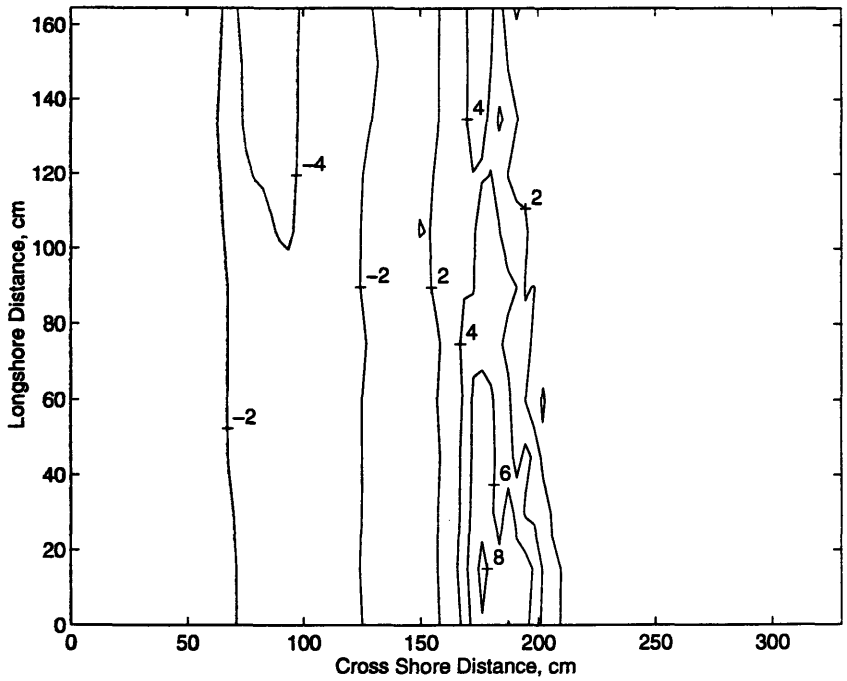


Figure 4-24: Contours of constant deposition, (+), and erosion, (-), on dune beach after spectral erosion for 25 min by $T_{eq} = 1.05$ s, $H_{eq} = 5.9$ cm waves. This is Figure 4-15 minus Figure 4-12 with 2 cm contours.

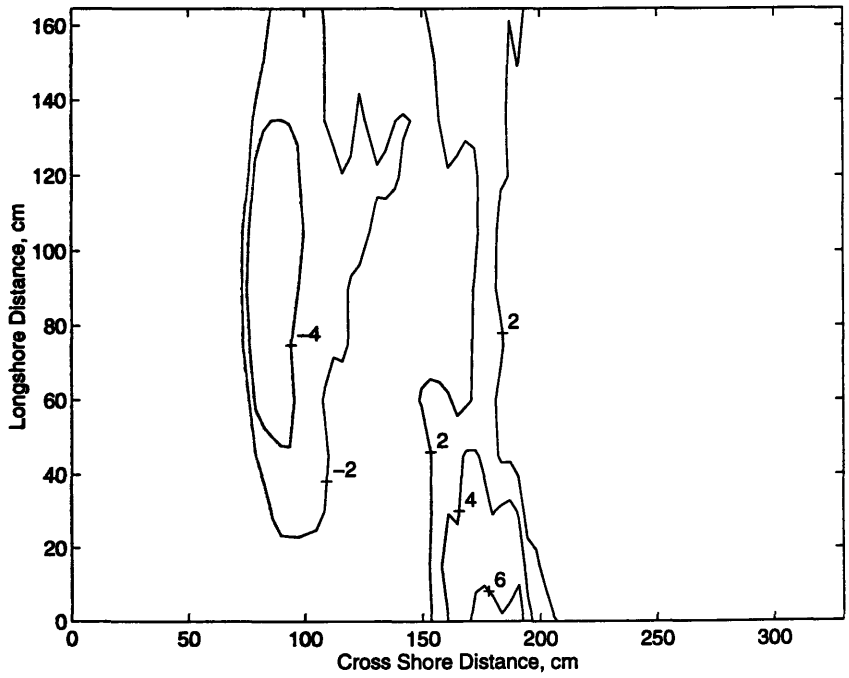


Figure 4-25: Contours of constant deposition, (+), and erosion, (-), on dune beach after monochromatic erosion for 25 min by $T_{eq} = 1.02$ s, $H_{eq} = 6.7$ cm. This is Figure 4-18 minus Figure 4-21.

significantly more uniform than the 1 s monochromatic waves. The 1 s wave probably excites one of the natural frequencies of the beaches. The contour plots after erosion, the profiles after recovery and the contour plots after recovery are not given for the second sequence because they are very similar to the results already presented.

This section clearly demonstrates the desirability of using spectral waves for beach erosion modeling. The energy concentrations that monochromatic waves exhibit cause the waves to hit the same area again and again. Since the waves are repeated, small perturbations in local beach conditions can lead to non-uniformity in the beach. On the other hand, spectral waves spread the energy over several frequencies with no single frequency dominating. Even if one of the spectral components excites a natural frequency of the system, the energy in that component is too small to overcome the smoothing influence from the other frequencies.

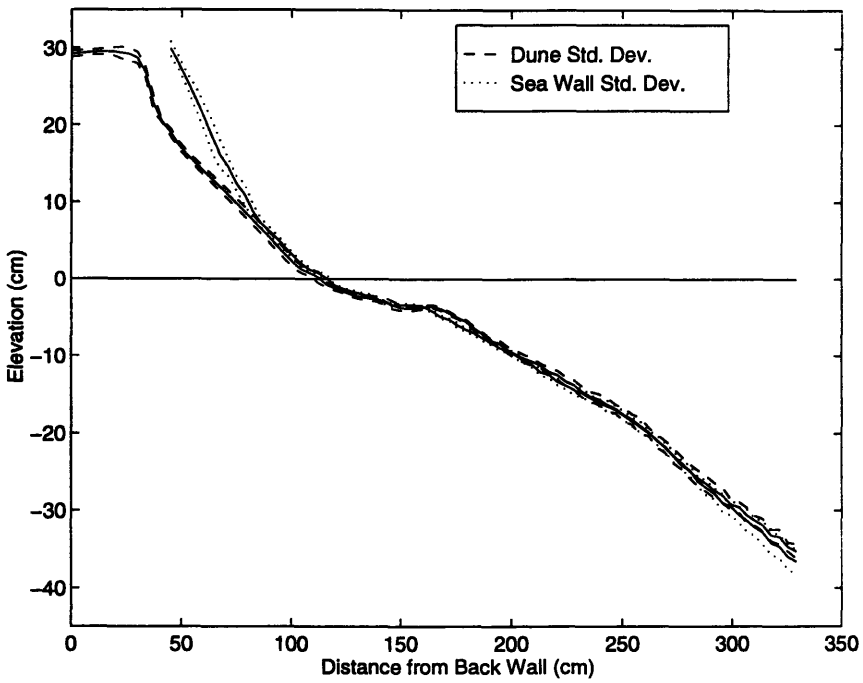


Figure 4-26: Profile after spectral erosion for 16.67 min by $T_{eq} = 1.39$ s, $H_{eq} = 6.7$ cm waves during second spectral and monochromatic wave sequence.

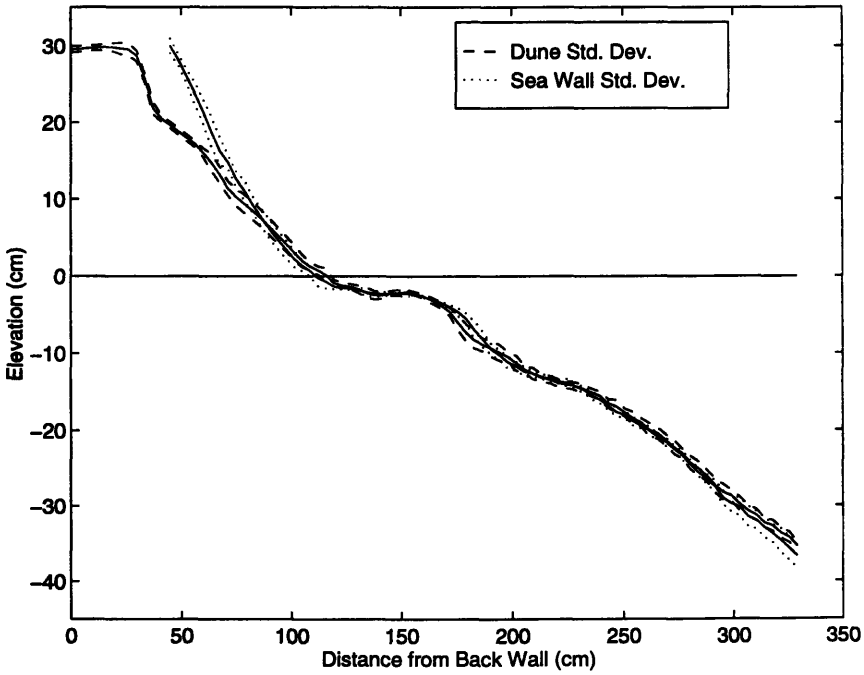


Figure 4-27: Profile after monochromatic erosion for 16.67 min by $T_{eq} = 1.54$ s and $H_{eq} = 7.5$ cm during second spectral and monochromatic wave sequence.

## 4.3 Erosion and Accretion Criteria

When planning the experiments initially, we looked at the erosion criteria presented in Section 2.3 for an estimate of the wave conditions which would cause erosion and accretion. The first wave that we ran was on the erosion-accretion boundary for one of the main criteria but the wave managed to erode nearly all of the beach within the first minute. Obviously, due to scale effects, the criteria determined in large wave tanks and prototype beaches did not hold for a small wave basin experiment like ours.

This experimental study was not designed to determine the erosion and accretion criteria for our wave basin, but we thought it would be useful for future work in the basin to use some of our data to empirically determine criteria that are valid in the basin.

The criteria we look at are the $S_0$ and $N_0$ criteria from Larson and Kraus (1989), the $N_0$ criteria from Kraus et. al. (1991), the $N_0$ and $F_0$ criteria from Kraus et. al. (1991) and the profile parameter criteria, $P_0$, from Dalrymple (1992). The sediment is the same for all experiments and has a fall velocity of $w_f = 2.5$ cm/s determined from the grain size. Table 4.4 presents the limited set of data from our experiments used to calculate the erosion and accretion criteria valid in our basin.

The data that we have obtained are shown in Figures 4-28 and 4-29. Figure 4-28 shows the data plotted on a $\log S_0$ versus $\log N_0$ diagram. Larson and Kraus (1989) propose the criteria

$$S_0 = C{N_0}^3 \tag{4.1}$$

with $C = 0.00070$. With our data set, the criteria is $C = 0.0056$, which is an order of magnitude different than the Larson and Kraus constant. For our data set, the $S_0$ and $N_0$ criteria does not fit particularly well. Kraus et. al. (1991) propose the simple criteria $N_0 = 2.0$. Our data set is better fit by $N_0 = 1.4$, which is a relatively small difference from Kraus' value.

Figure 4-29 is a plot of the data on a $\log N_0$ versus $\log F_0$ diagram. Kraus et. al. propose the criteria

$$N_0 = C{F_0}^2 \tag{4.2}$$

where $C = 8980$. Our data set fits a $N_0$ versus $F_0$ criteria, except with $C = 1000$, which again differs form the published criteria by an order of magnitude.

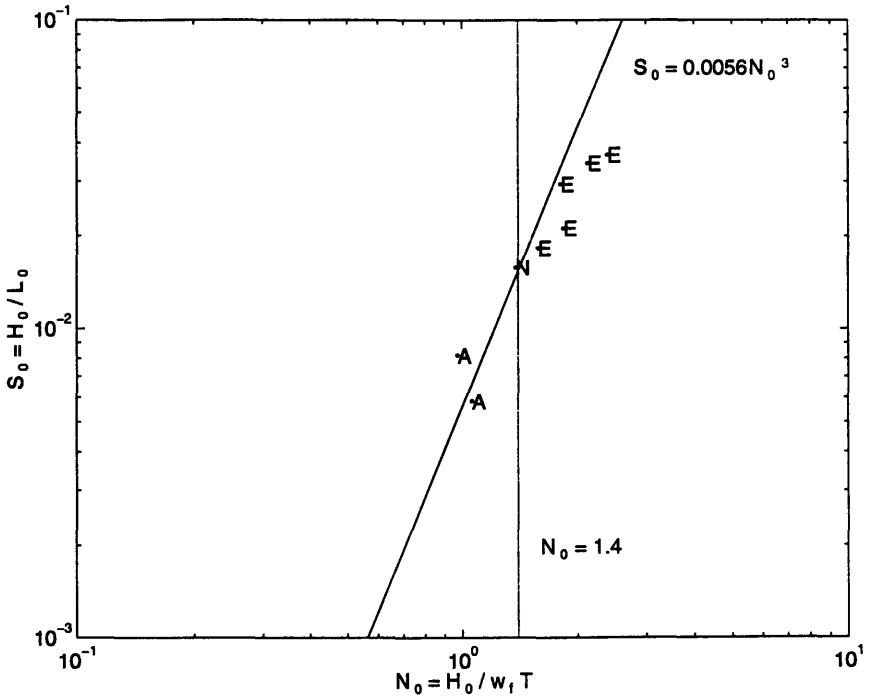


Figure 4-28: Erosion and accretion criteria plotted $\log S_0$ versus $\log N_0$ with Erosion (E), Accretion (A), or Neither (N).

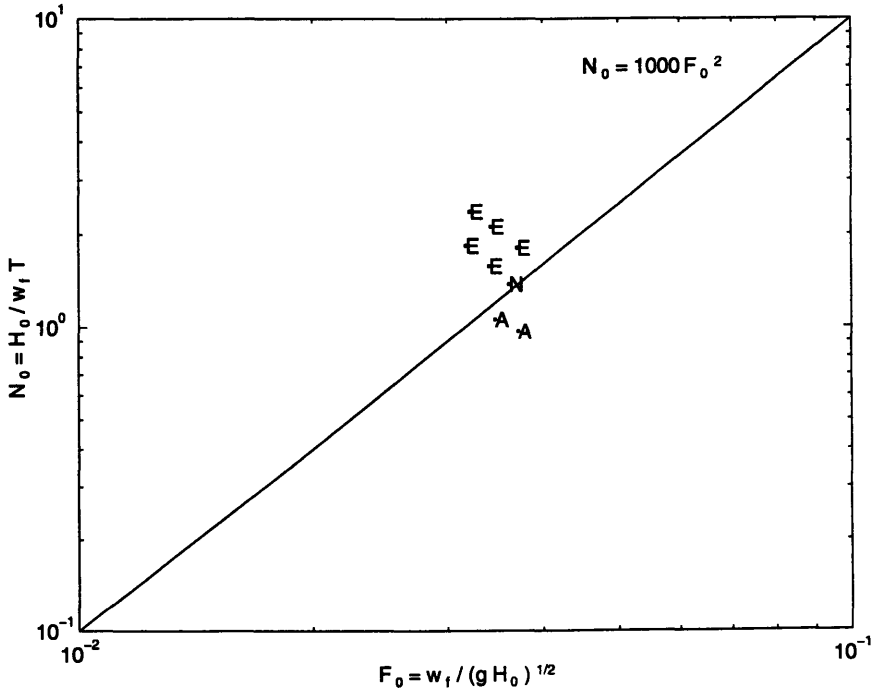


Figure 4-29: Erosion and accretion criteria plotted $\log N_0$ versus $\log F_0$ with Erosion (E), Accretion (A), or Neither (N).

Table 4.4: Data for erosion and accretion criteria determination: Erosion (E), Accretion (A), or Neither (N).

| $T_{mes}, s$ | $H_{mes}, cm$ | $S_0$ | $N_0$ | $F_0$ | $P_0$ | E, A or N |
|---|---|---|---|---|---|---|
| 1.04 | 4.6 | 0.0294 | 1.81 | 0.0370 | 1320 | E |
| 1.04 | 5.4 | 0.0344 | 2.12 | 0.0342 | 1810 | E |
| 1.05 | 6.1 | 0.0366 | 2.38 | 0.0321 | 2310 | E |
| 1.43 | 4.6 | 0.0158 | 1.38 | 0.0361 | 1062 | N |
| 1.41 | 5.2 | 0.0183 | 1.58 | 0.0340 | 1370 | E |
| 1.40 | 6.0 | 0.0212 | 1.84 | 0.0317 | 1830 | E |
| 1.93 | 4.4 | 0.0082 | 0.97 | 0.0371 | 704 | A |
| 2.03 | 5.1 | 0.0085 | 1.06 | 0.0356 | 891 | A |

Finally, the erosion and accretion events are well separated by the profile parameter, $P_0 = gH_0{}^2/w_f{}^3T$, proposed by Dalrymple (1992). Dalrymple suggests the criteria $P_0 = 10,400$ but the data from this experiment is better separated by $P_0 = 1000$, which, again, is different from the published value by an order of magnitude.

The data sets that went into the published criteria were from large wave tanks and from field studies. Due to scale effects, data sets from small wave tanks and basins will not fit criteria based on data from large scale experiments. However, the dimensionless parameters are based on the physical forces moving the sediment, so the criteria should have the same dimensionless parameters in the same equations, but with different constants. For future work in the basin we would recommend the simple criteria $N_0 = 1.4$ or $P_0 = 1000$.

## 4.4 Simulated Storm Surge Response

After the first several experiments which we ran at a constant depth, we noticed that there appeared to be a limit to how far the beach would erode, even during extensive erosional sequences. The water level was low enough that the toe of the sea wall was not in the surf zone. The sea wall was set back on the beach so there was some beach in front of the toe of the wall. Previous experiments by (citations forthcoming) have shown that with the sea wall set back from the beach, the erosion and scour in front of the sea wall are limited, which was our experience also. As the beach in front of the sea wall erodes, the sand is moved into an offshore bar. Then, as the waves pass over this bar, the waves break and their energy is dissipated. When the waves reach the toe of the sea wall, they have lost

most of their energy, and are unable to cause more erosion. Even in our most severe erosion sequence, with the conditions given in Table 4.1, the waves were unable to cause a scour at the toe of the sea wall, as seen in Figure 4-8. With an increase in water depth, the toe of the sea wall would be in the surf zone. If the waves break on the toe of the sea wall with sufficient energy, they could cause a significant scour at the sea wall toe and erosion from the shore area. In this case, there is potential for more erosion in front of the sea wall than on the dune beach.

In order to test this hypothesis, we ran two experiments with the divided beach and a water depth variation. The first experiment involved raising the water depth and eroding the beach then lowering the water depth and recovering the beach. The second experiment involved raising the water depth, eroding, lowering the water depth, eroding again, and then recovering. One possible mechanism for increased erosion is that the storm surge or tidal variation could work as a pumping mechanism. The higher water level would allow the waves to access sand high up on the beach and move it into a bar off shore. This bar would be relatively high compared to the mean water level, so when the water level dropped and erosional waves continued, the bar would be moved further off shore. Following the storm event, when the longer, accretional waves returned, the sand would be further offshore than without the storm surge. If this mechanism were efficient, it could move the sand far enough offshore that it would essentially be lost from the system.

For modeling accuracy, it would be better to vary the water depth while generating waves. That way, the depth would vary gradually during the wave generation. However, the wave basin is not capable of gradually varying the water elevation while running waves since the basin inflow is controlled from the wave maker control panel and cannot be used while waves are being generated. The outflow is located in the basement and is controlled at a manual valve. It could be set at different levels to vary the outflow rate, but it does not offer fine water level control. We used a discrete water level change, changing the depth between wave events and beach measurements.

The first experiment looked at the first step in the mechanism. The initial profiles are shown in Figure 4-30 with $z = 0$ at the still water level (SWL) of $h = 57.4$ cm. the initial profile is not actually an "equilibrium" profile as defined in Section 4.1 because it was formed by a monochromatic recovery after the second spectral wave versus monochromatic wave experiment. This means that the initial profile is not in the fully recovered state and

cannot be used as a true reference for the eroded and recovered conditions. The eroded profiles are shown in Figure 4-31 with an elevated water level of 60.0 cm. This figure shows that, after ersion, the toe of the sea wall was not uncovered. The toe of the sea wall was just covered with sand, so the sea wall was in the swash zone, but not in the surf zone. The beach was eroded for 25 minutes by $T_{eq} = 1.07$ s, $H_{eq} = 6.3$ cm waves. Then the water level was dropped to 57.5 cm, and the beach recovered for 25 minutes by $T_{eq} = 2.12$ s, $H_{eq} = 5.3$ cm waves. The recovered beach shown in Figure 4-32 with SWL at 57.5 cm showing that the beaches recovered fully to their initial profile. For this case, there was not a significant sea wall effect.

In the second sequence, the initial water depth is 57.5 cm and the initial profile is the post-recovery profile after the first storm surge experiment, shown in Figure 4-32. The initial profile for this sequence was formed by the standard spectral recovery and can be considered an equilibrium profile. In the initial profile, the toe of the sea wall was covered with sand and the sea wall was not in the active surf zone. The water level was raised to 60 cm and the beach was eroded for 16.67 minutes by $T_{eq} = 1.37$ s, $H_{eq} = 6.5$ cm waves. The resulting profile is shown in Figure 4-33 with the SWL at 60 cm. There was significant erosion at the toe of the sea wall and into the base of the dune but the toe of the sea wall is still covered by some sand. The water level was returned to 57.5 cm and the beach eroded for an additional 25 minutes by 1.06 s, 6.3 cm waves. The resulting profile is shown in Figure 4-34 with a SWL of 57.5 cm. This second erosion moved the berm and some of the sand in the sruf zone further offshore. In Figure 4-33 the crest of the berm is approximately at $x = 155$ cm, while Figure 4-34 shows the crest of the berm has moved to $x = 175$ cm. The two beaches are still nearly identical in their shape and response.

After the two erosion events, with the SWL still at 57.5 cm, we attempted to recover the beaches with accretional waves. We generated $T_{eq} = 2.08$ s, $H_{eq} = 5.3$ cm waves for 25 minutes. The resulting beach profile is given in Figure 4-35. Both beaches recovered to almost exactly their initial profile. Figure 4-36 is a plot of the maximum erosional change and the net change during the sequence. The recovery was complete showing that a small storm surge erosion does not move the sand sufficiently far offshore so that the beach profile is permanently altered. This may be because the toe of the sea wall was never fully in the surf zone and the dune did not erode significantly. These were the only two experiments run with a water depth variation and a divided beach. Section 4.6 describes an experiment

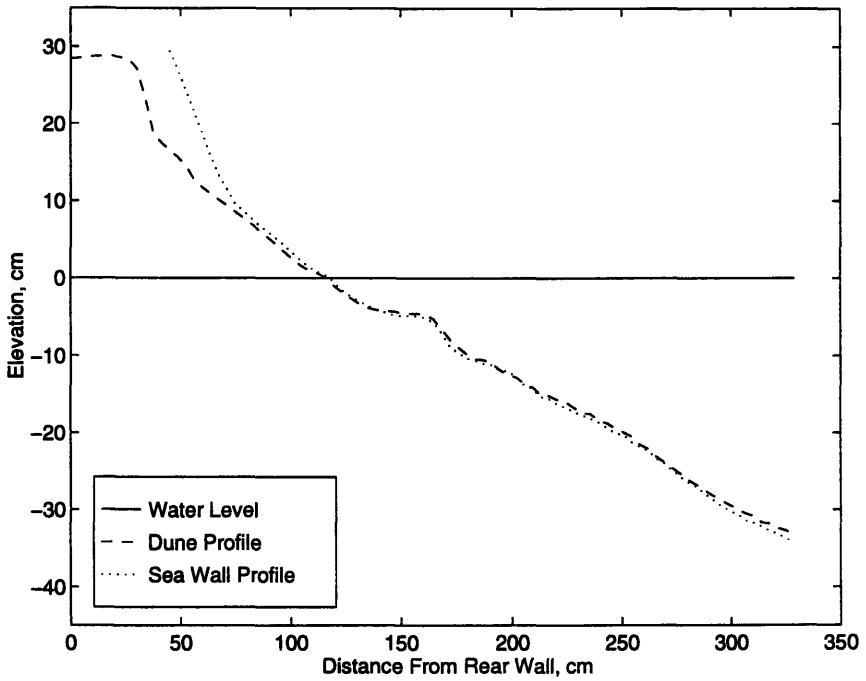


Figure 4-30: Profiles of beaches before first storm surge erosion with the SWL at $h = 57.4$ cm.

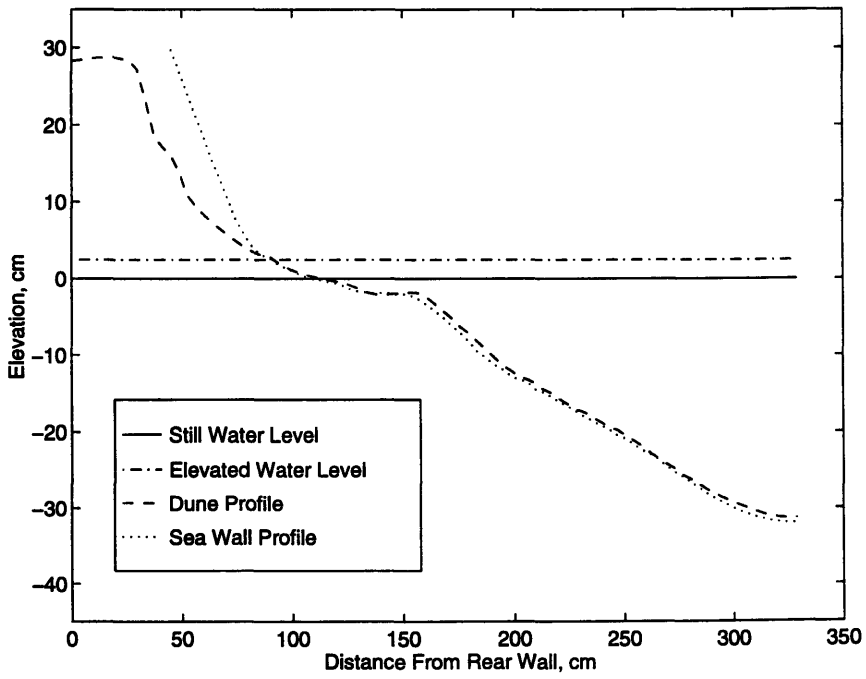


Figure 4-31: Profiles of beaches in Figure 4-30 after erosion for 25 minutes by a $T_{eq} = 1.07$ s, $H_{eq} = 6.3$ cm wave in the first storm surge sequence with an elevated water level of $h = 60$ cm.

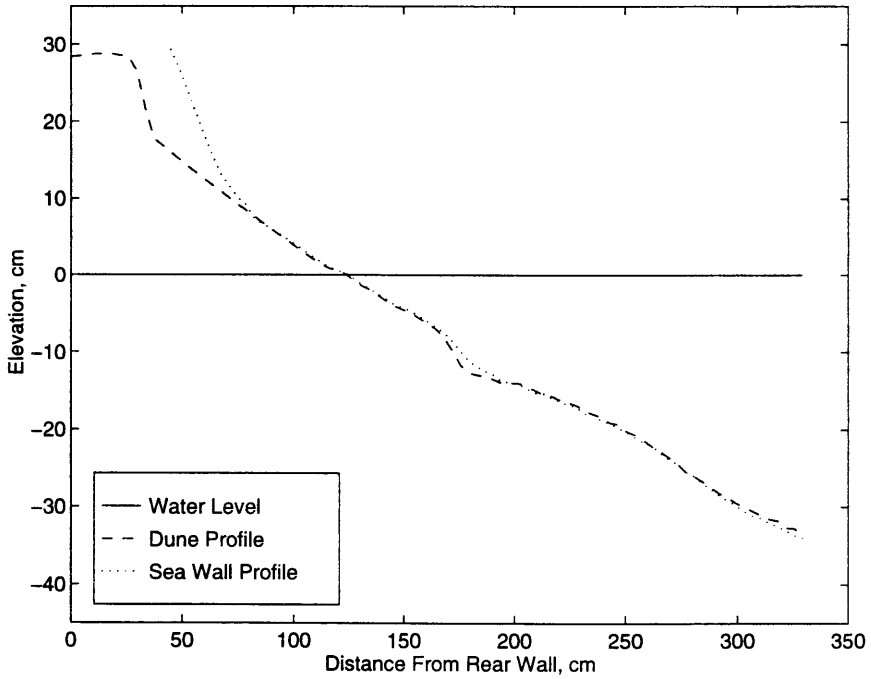


Figure 4-32: Profiles of beaches in Figure 4-31 after recovery for 25 minutes by a $T_{eq} = 2.12$ s, $H_{eq} = 5.3$ cm wave during the first storm surge sequence with the SWL at $h = 57.5$ cm.

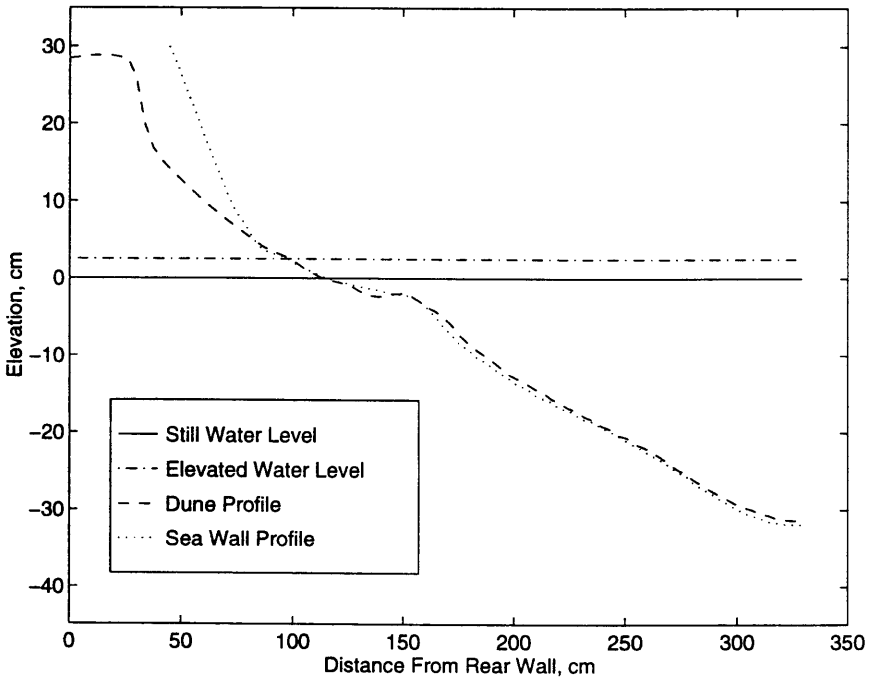


Figure 4-33: Profiles of beaches in Figure 4-32 after erosion for 25 min by 1.37 s, 6.5 cm waves during the second storm surge sequence and with an elevated water level of 60 cm.

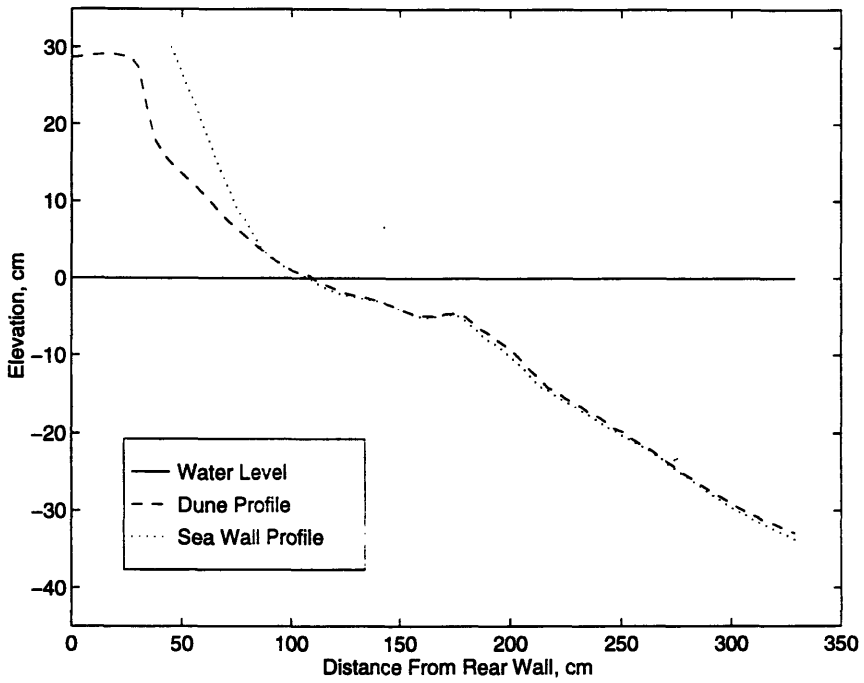


Figure 4-34: Profiles of beaches in Figure 4-33 after erosion for 25 min by 1.06 s, 6.3 cm waves during the second storm surge sequence and with a SWL of 57.5 cm.

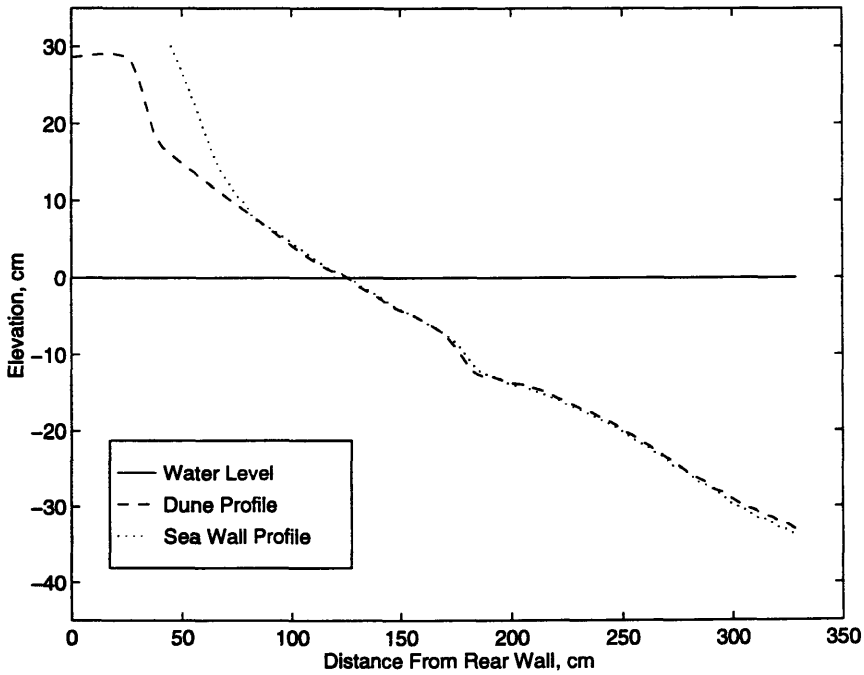


Figure 4-35: Profiles of beaches in Figure 4-34 after recovery for 25 min by $T_{eq} = 2.08$ s, $H_{eq} = 5.3$ cm waves during the second storm surge sequence with the SWL at 57.5 cm.

conducted without the dividing wall with a larger storm surge and a more extensive erosion sequence.

## 4.5 Sea Wall and Dune Interaction

After examining the case of separate beaches, we removed the dividing wall and allowed the beaches to interact in the surf zone. After the wall was removed, the beach was regraded to be smooth and uniform for the next experiment. Accretional waves were generated to bring the beach to the equilibrium profile described in Section 4.1. We ran three experiments without the dividing wall. The first two were single step erosional and recovery events that repeated previous experiments. The third was an extensive erosion and recovery that looked at the longer term effects of waves on the beach.

A profile plot of the initial beach condition for the experiment is given in Figure 4-37 and a contour plot is given in Figure 4-38 with a 2 cm contour. The initial beach is after the conditioning accretional waves mentioned above. Without the dividing wall, the entire beach can be measured at once. There are a total of 25 transects measured with the same longshore and cross shore measurement spacing. There are twelve transects on the dune and thirteen transects on the sea wall, with the thirteenth transect at the edge of the sea wall next to the dune. If the thirteenth transect is considered the center transect, the profiles in this section are constructed by averaging the 6 outside transects for both the sea wall and dune. The thirteen transects around the end of the sea wall are not used for the average due to the longshore variability around the end of the sea wall. Some of the profiles in this section do not appear to conserve sand volume, because the profiles do not take into account nearly half of the beach.

The beach was then eroded for 30 min by $T_{eq} = 1.42$ s, $H_{eq} = 5.6$ cm waves. A profile of the beach is given in Figure 4-39 and a contour plot of the beach after erosion is given in Figure 4-40, with a 2 cm contour, showing the erosion at the toe of the sea wall and the base of the dune. The sand has moved offshore to form a bar near the $z = -4$ contour line.

The beach was recovered for 30 min with $T_{eq} = 2.01$ s, $H_{eq} = 5.1$ cm waves. The resulting beach is shown in a profile plot in Figure 4-41 and in a contour plot in Figure 4-42 with a 2 cm contour. The plots show that there is not enough interaction in the small scale erosion and accretion case to cause a significant longshore variation.

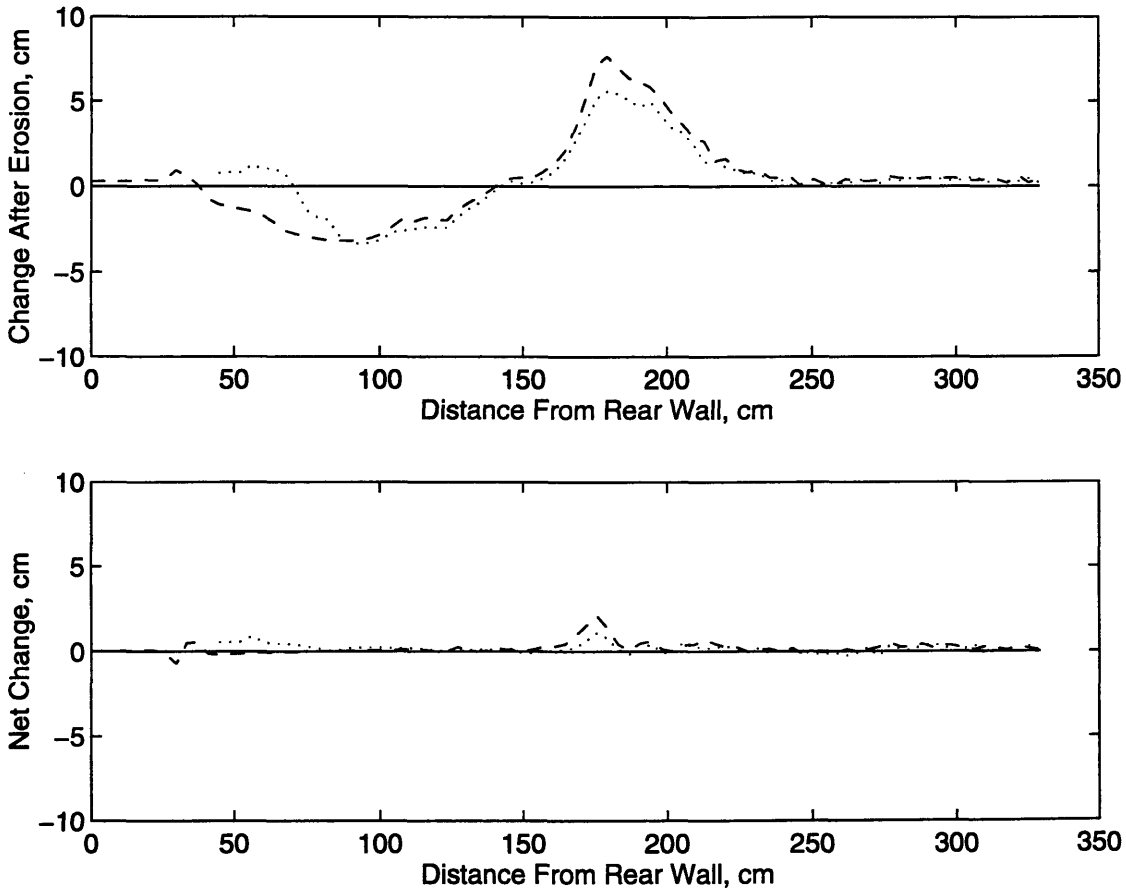


Figure 4-36: Maximum erosion, Figure 4-34 minus Figure 4-32, and net erosion, Figure 4-35 minus Figure 4-32, during the second storm surge sequence. (- - -) Dune, (...) Sea Wall.

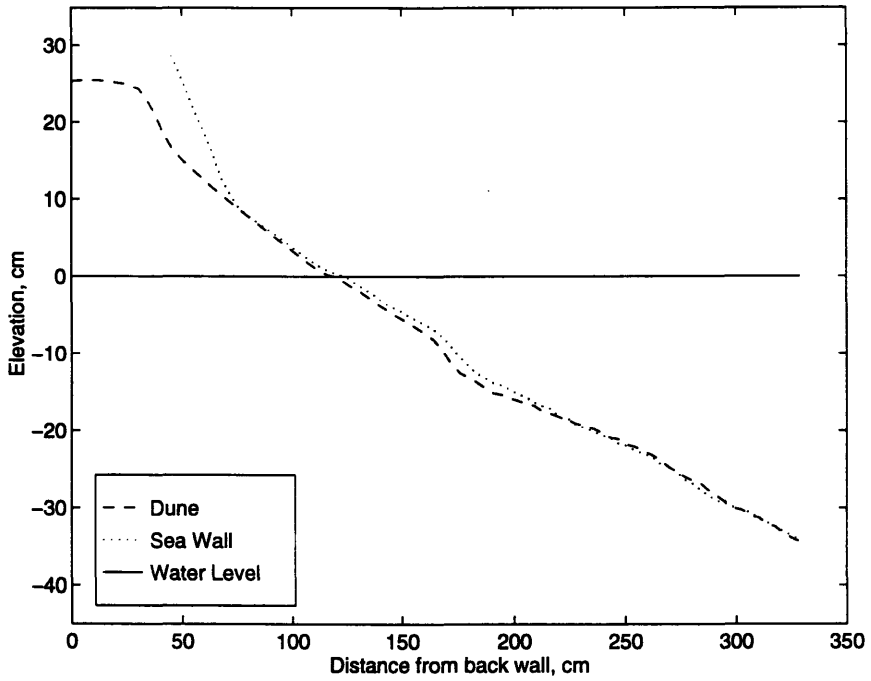


Figure 4-37: Profiles of beaches before erosion during interaction experiment.

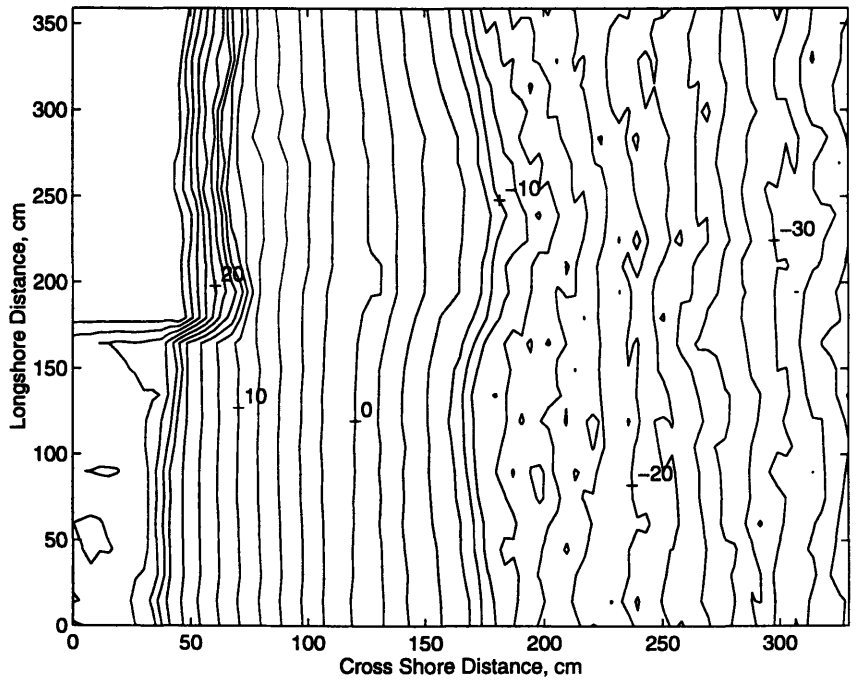


Figure 4-38: Contour plot with 2 cm contours of beach before erosion during interaction experiment.

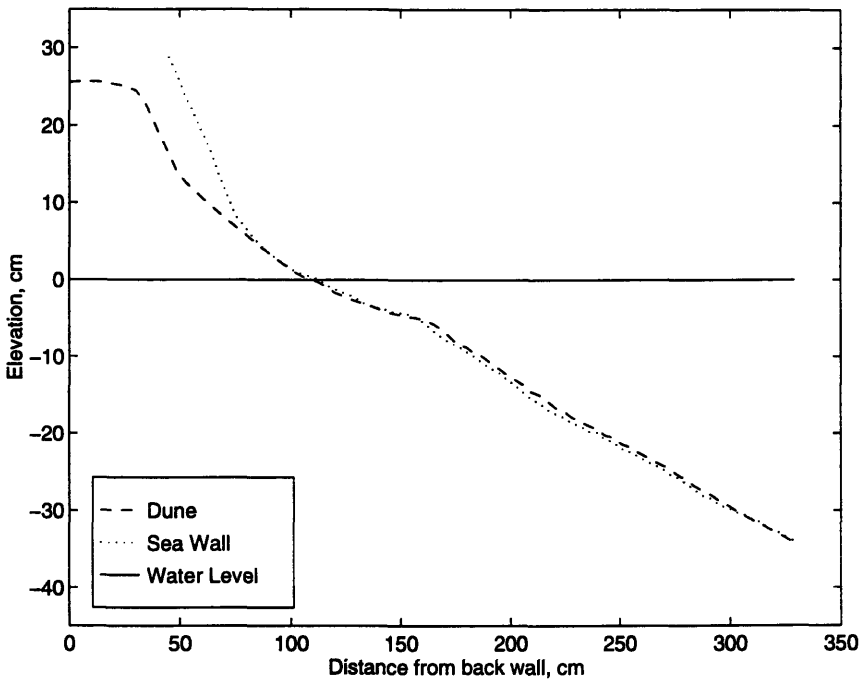


Figure 4-39: Profile of beaches in Figure 4-37 after erosion for 30 min by $T_{eq} = 1.5$ s, $H_{eq} = 5.6$ cm waves.

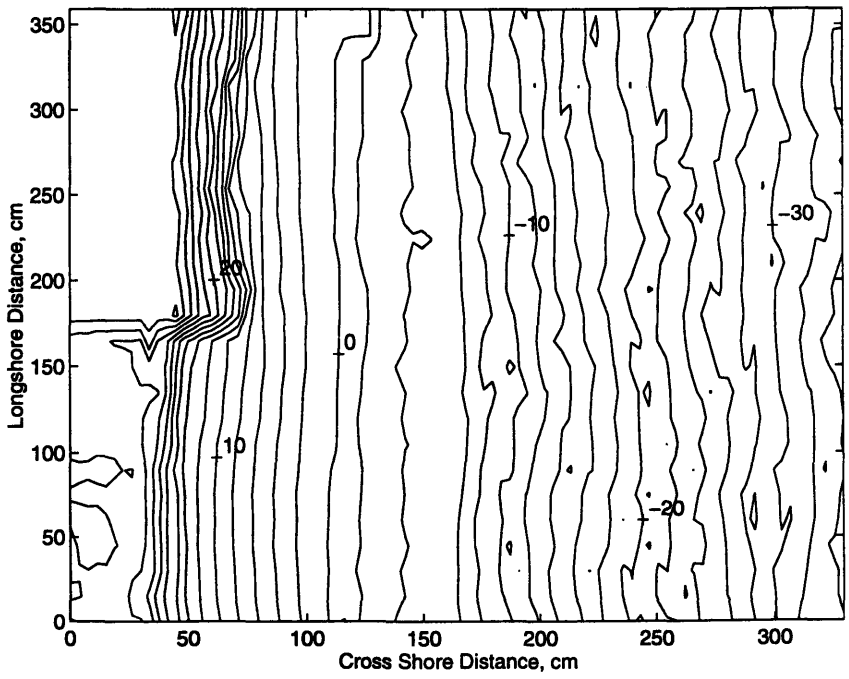


Figure 4-40: Contour plot with 2 cm contours of beach in Figure 4-38 after erosion for 30 min by $T_{eq} = 1.42$ s, $H_{eq} = 5.6$ cm waves.

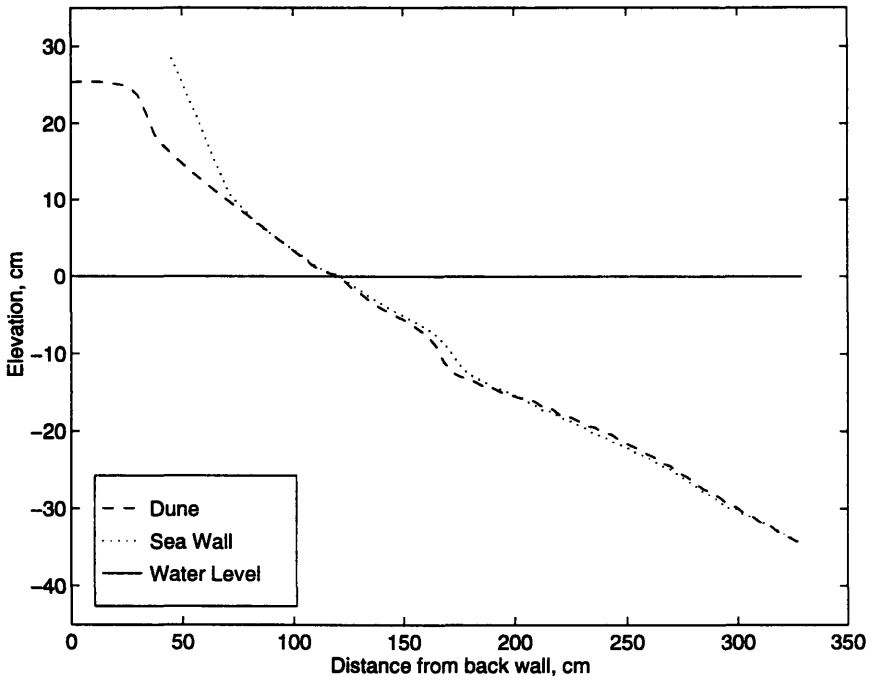


Figure 4-41: Profile of beaches in Figure 4-39 after recovery for 30 min by $T_{eq}$ = 2.01 s, $H_{eq}$ = 5.1 cm waves.

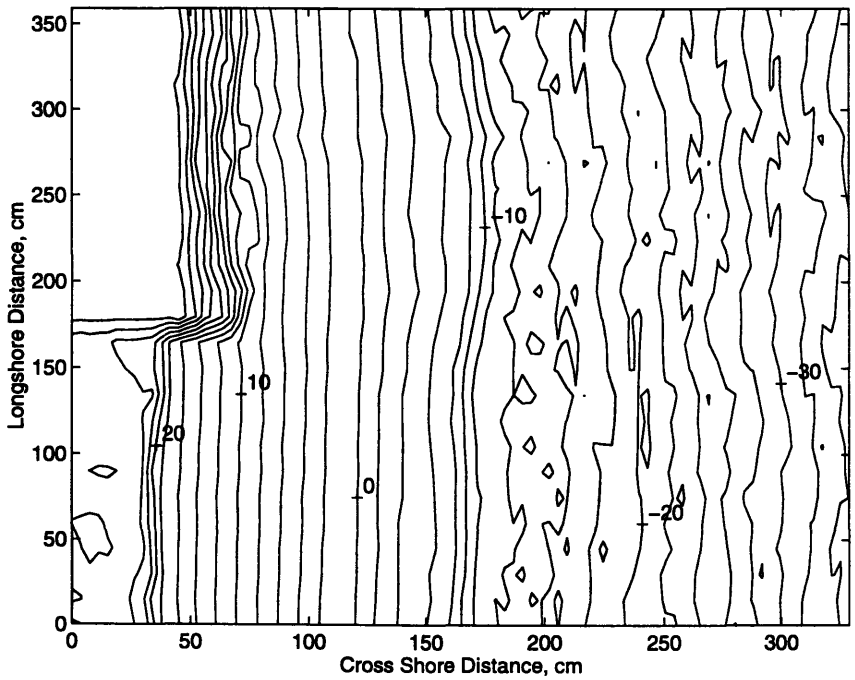


Figure 4-42: Contour plot with 2 cm contours of beach in Figure 4-40 after recovery for 30 min by $T_{eq}$ = 2.01 s, $H_{eq}$ = 5.1 cm waves.

Table 4.5: Equivalent wave conditions for extensive erosion case without divider wall.

| $T_{eq}$, s | $H_{eq}$, cm | Duration, min | E or A |
|---|---|---|---|
| 1.06 | 6.0 | 30 | E |
| 1.95 | 5.0 | 30 | A |
| 1.08 | 6.3 | 15 | E |
| 1.40 | 6.2 | 15 | E |
| 1.40 | 7.2 | 15 | E |
| 1.42 | 8.0 | 15 | E |
| 1.42 | 8.2 | 15 | E |
| 1.84 | 4.9 | 15 | A |
| 1.96 | 5.2 | 15 | A |
| 2.06 | 5.4 | 30 | A |
| 2.00 | 5.3 | 60 | A |
| 1.95 | 5.1 | 120 | A |

To show where the sand was eroded and deposited, a contour plot of the beach change during erosion is given in Figure 4-43. This figure does not appear to conserve volume at first glance, but there was a large area with an erosion of less than 2 cm that does not show on this figure. The deposition is more concentrated than the erosion so it appears there is more deposition than erosion. The difference between the two profiles corresponds to a 0.2 cm sand layer in the measurement area, which is within the measurement error. The net change from the initial beach to after recovery is given in Figure 4-44 showing very little net change.

The second and third experiments are combined in the analysis because there was a problem with one of the beach profile data sets. The data set for the beach measurement between the two experiments is corrupted and cannot be used. Combining the experiments creates a single extensive experiment out of a single step erosion and accretion plus an extensive erosion and accretion sequence. The wave conditions for this long experiment are given in Table 4.5 with an "E" for erosion and an "A" for accretion events. The wave conditions are not equivalent to the conditions presented in Section 4.1 for a different extensive erosion sequence.

The initial beach condition for the second, or extensive, sequence is the final condition from the previous sequence, given in Figure 4-41 as a profile plot and in Figure 4-42 as a contour plot. Figures 4-45 and 4-46 show the beach condition after the $T_{eq} = 1.42$

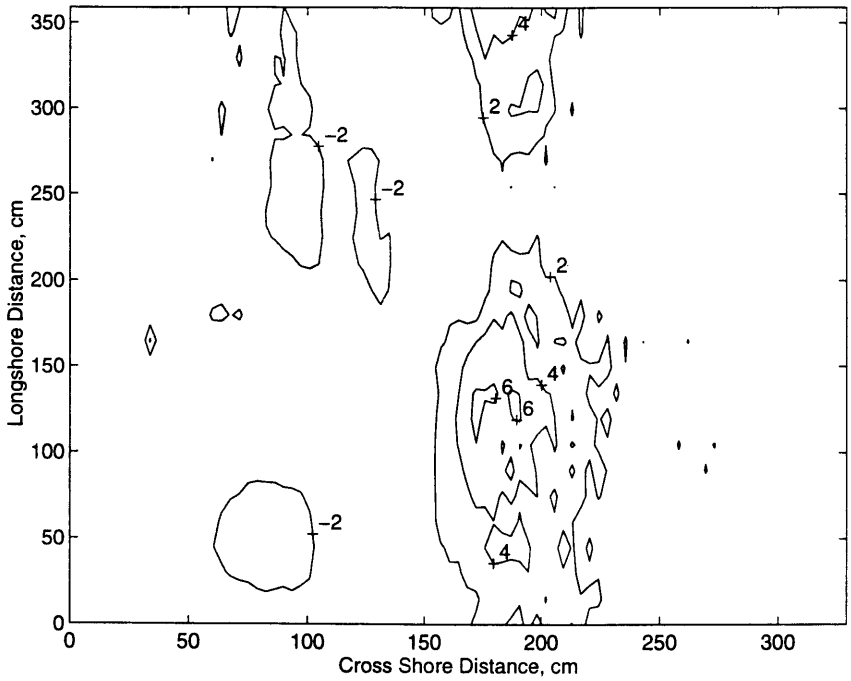


Figure 4-43: Contour plot of beach change during erosion for 30 min by $T_{eq}$ = 1.5 s, $H_{eq}$ = 5.6 cm waves, made by subtracting Figure 4-38 from Figure 4-40.

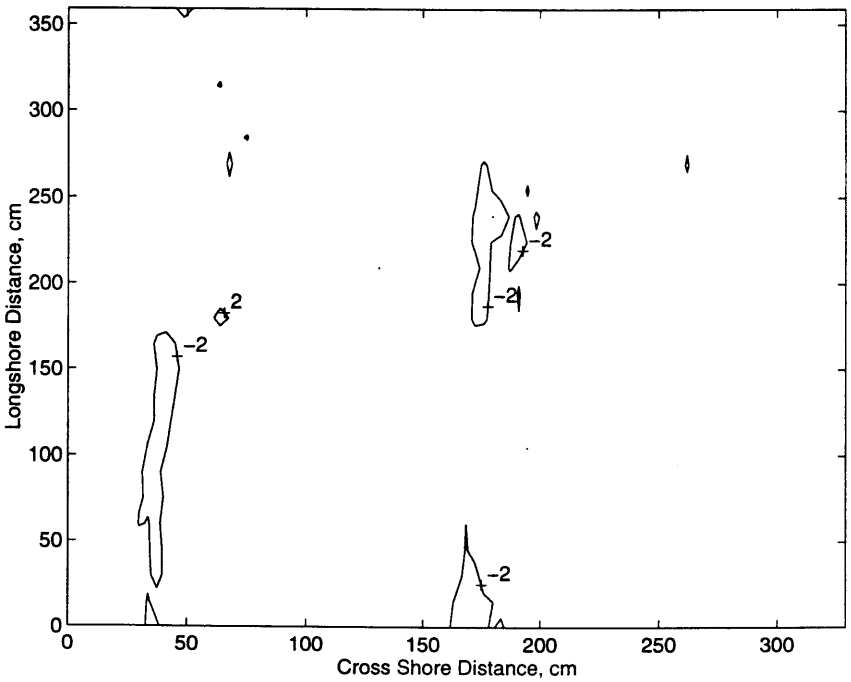


Figure 4-44: Contour plot of net change during first interaction from Figure 4-42 minus Figure 4-38.

s, $H_{eq}$ = 8.2 cm erosion event, see Table 4.5, showing the beach severely eroded. The unprotected beach is noticeably uniform in the longshore direction including near the edge of the sea wall. It does not exhibit the typical end effect, or flanking, associated with sea wall erosion. This is a result of using normally incident waves without an induced longshore current. There is some curvature in the off shore bar formed, but this is not very great. The dune beach eroded more than the sea wall was able to because the sea wall fixes the shoreline. As a result, the shoreline and the offshore bar on the unprotected beach are further shoreward than they are on the protected beach. Figure 4-47 shows the maximum erosion during the second sequence. There is significant sand loss, especially from the dune beach, with the sand being deposited offshore in front of the sea wall. This provides evidence that there is significant longshore redistribution of sand even with normally incident waves.

The recovered beach at the end of the sequence in Table 4.5 is shown as a profile in Figure 4-48 and as a contour plot in Figure 4-49 after four hours of accretional waves. The net change during this extensive erosion and accretion sequence is given as a contour plot in Figure 4-50. The edge of the dune has experienced a permanent 2 to 6 cm erosional loss during this sequence while the net loss in front of the sea wall is negligible. The sand permanantly lost from the dune appears to have been distributed diagonally across the beach and has been deposited offshore from the sea wall.

The recovery sequence lasted for four hours (see Table 4.5) to insure that the profile had reached equilibrium. The majority of the recovery occurred in the first hour as shown in Figure 4-51 which shows profiles of recovery at 30 minutes, 1 hour and 4 hours. The profiles were obtained from the six transects on the dune and sea wall used for the other profiles in this chapter. If we call the beach fully recovered at 4 hours, we can determine the fraction of recovery over time. This is given in Table 4.6. The waves during the last two erosion events were very large and steep, so the beaches were severely eroded and took longer than the usual 30 minutes to recover.

Since this experiment was conducted in the limiting conditions with normally incident waves and with the sea wall set on the beach out of the active surf zone, the conclusions we can make about the beach behavior are limited. In this experiment, the beach behaved almost exactly as it had while the dividing wall was present. There was not a significant longshore current to move sediment along the beach so any longshore sediment transport was due to local circulation and any beach gradient in the the longshore direction. The beach

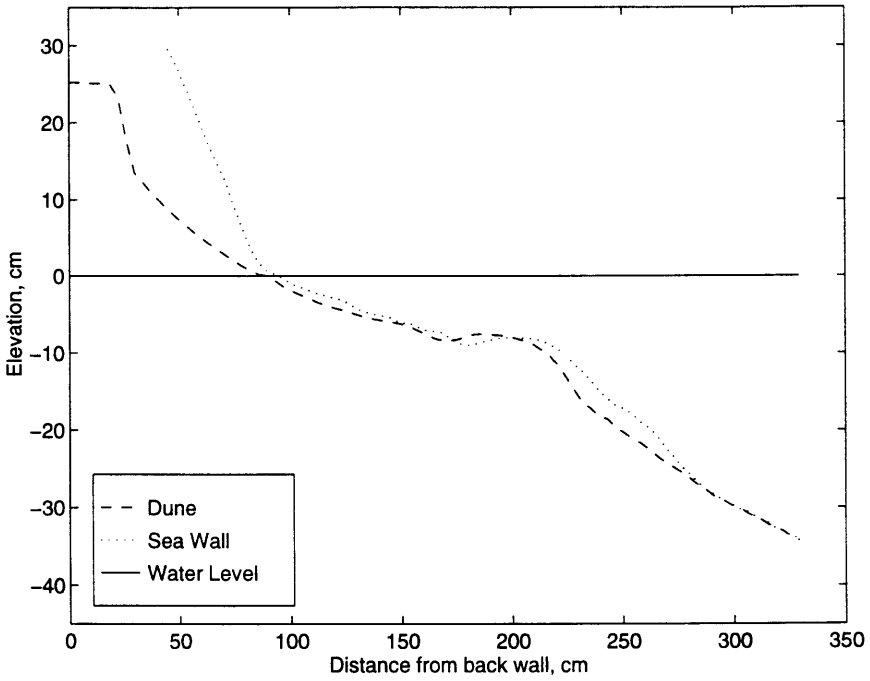


Figure 4-45: Profile plot of beach in Figure 4-41 after extensive erosion under the conditions in Table 4.5.

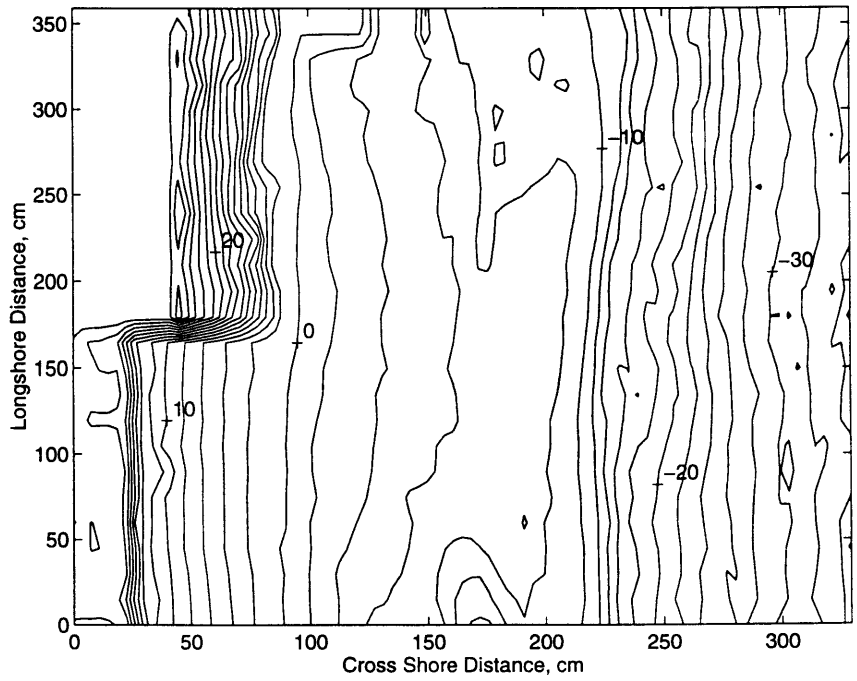


Figure 4-46: Contour plot with a 2 cm contour of the beach in Figure 4-42 after extensive erosion under the conditions in Table 4.5.

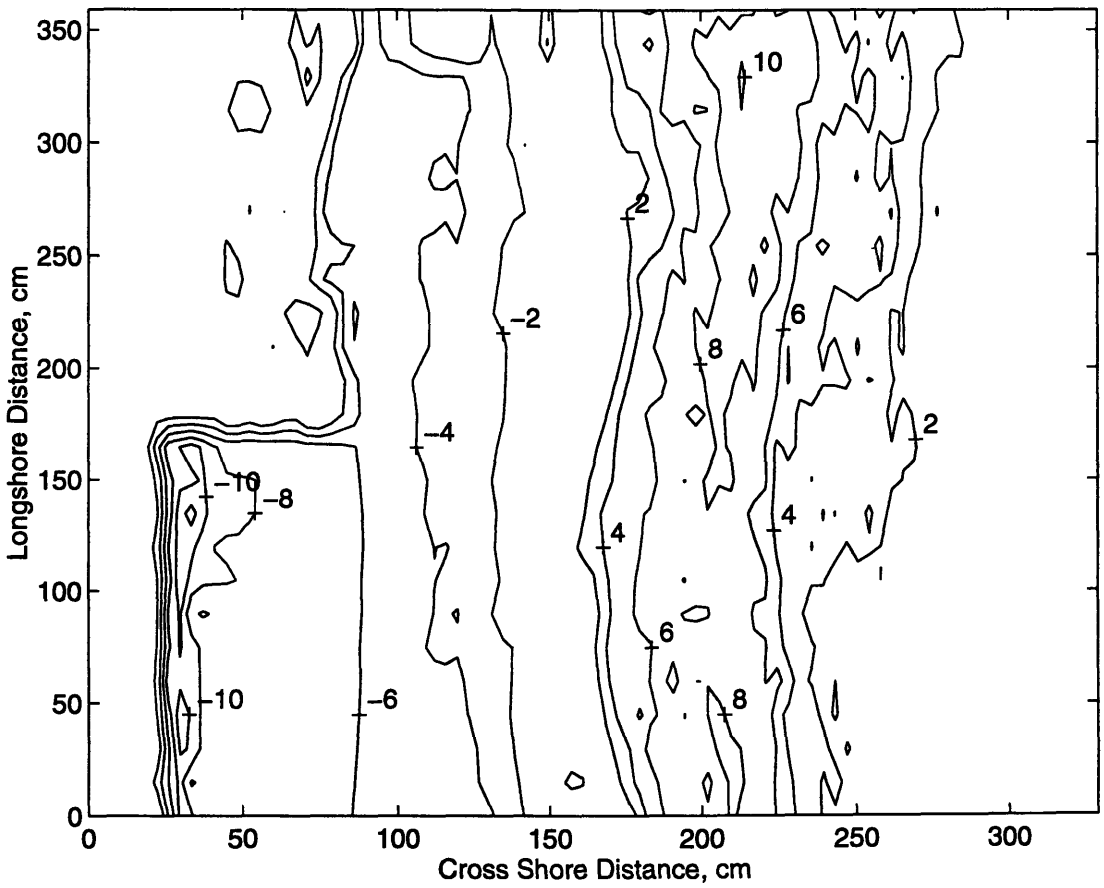


Figure 4-47: Contours of erosion during extensive erosion sequence from Table 4.5, made from Figure 4-46 minus Figure 4-42.

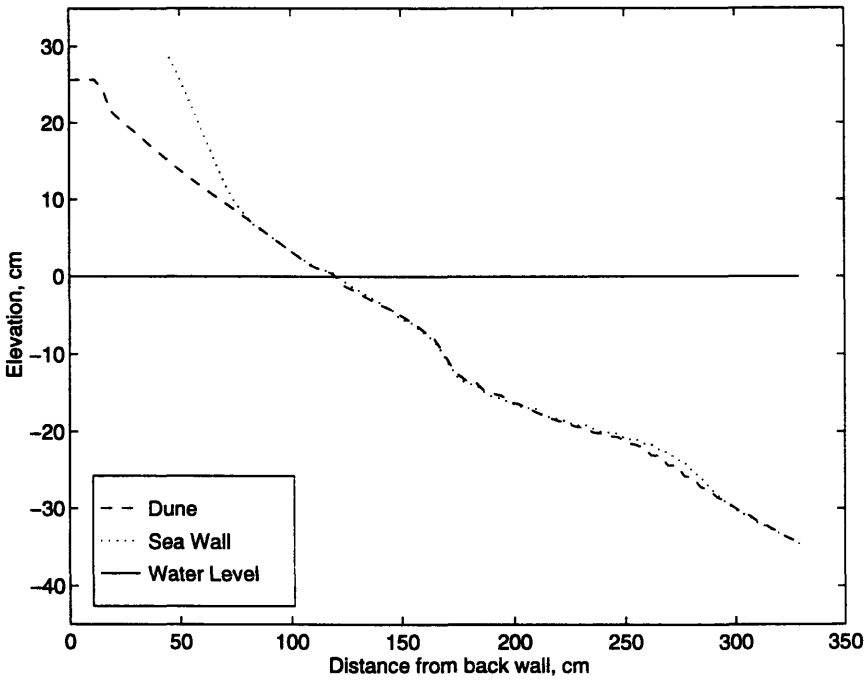


Figure 4-48: Profile of beach in Figure 4-45 after accretional waves in Table 4.5.

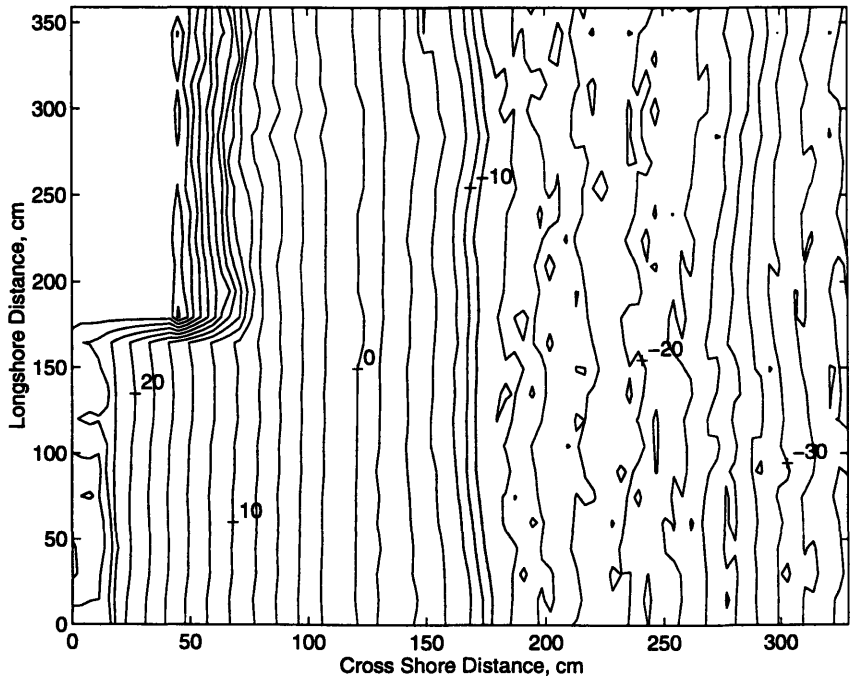


Figure 4-49: Contour plot with a 2 cm contour of beach in Figure 4-46 after accretional waves in Table 4.5.

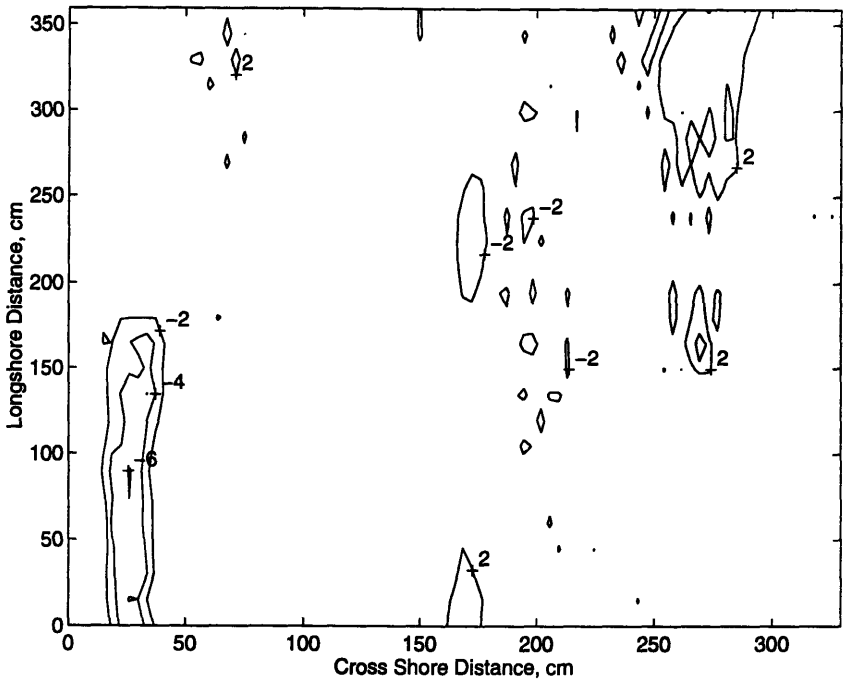


Figure 4-50: Contours of net change during extensive erosion and accretion sequence from Table 4.5, made from Figure 4-49 minus Figure 4-42.

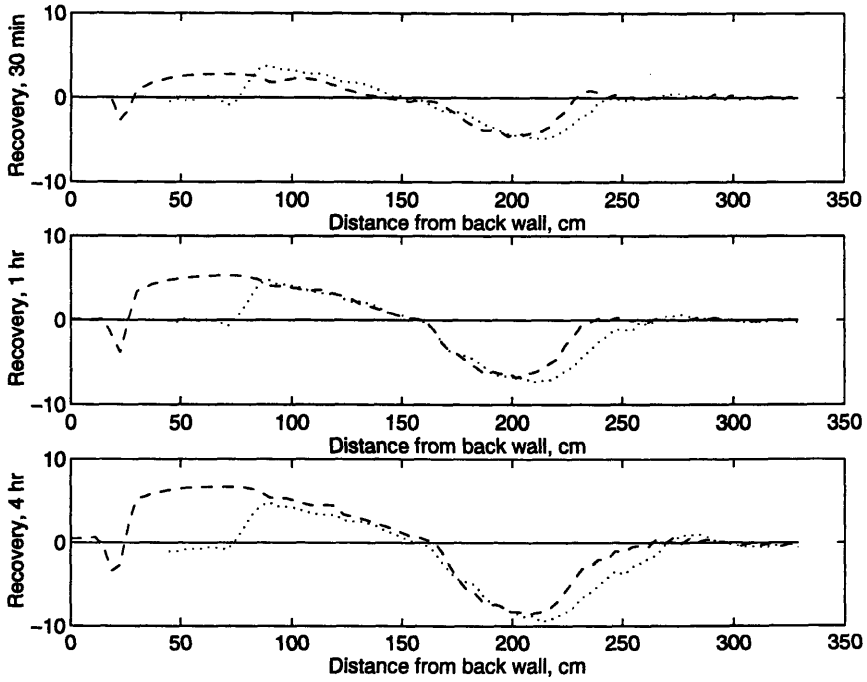


Figure 4-51: Amount of recovery after 30 minutes, 1 hour and 4 hours in extensive erosion with beach interaction experiment. (- - -) Dune, (...) Sea Wall.

Table 4.6: Fraction of recovery over time during the extensive erosion with beach interaction sequence.

| Time, hr | Recovery Fraction |
|---|---|
| 0.25 | 0.42 |
| 0.5 | 0.57 |
| 1.0 | 0.88 |
| 2.0 | 0.98 |
| 4.0 | 1.00 |

gradient was predominately in the cross shore direction, so the longshore redistribution in the extensive erosion case was predominately caused by circulation currents. There were no experiments with oblique waves, but the next experiment, described in Section 4.6, looks at sea wall and dune interaction with the sea wall in the active surf zone during a storm surge experiment.

## 4.6 Sea Wall and Dune Interaction With Storm Surge

This section describes an experiment with sea wall and dune interaction and a storm surge. The storm surge is greater than the surge described in Section 4.4 and the erosion is more extensive. In the previous storm surge experiments, the sea wall was not in the surf zone. During erosion, a berm was formed with the eroded sand. The berm was large enough to cause the incident waves to break, so the waves did not have enough energy to continue to erode at the toe of the sea wall. The increased water depth was not enough to put the sea wall in the surf zone, so there was not a significant scour in front of the sea wall. This experiment consists of erosion at the initial water level of $h = 58$ cm, erosion at an elevated, or storm surge, water level of $h = 62$ cm, erosion with $h = 58$ cm and recovery with $h = 58$ cm. The wave conditions for the experiment are given in Table 4.7.

Before this experiment, the basin had been full without any waves in our section for almost two months. The chlorinator was not working properly, and there was a significant biological layer growing on the sand surface. We did not want this layer interfering with the experiment, by either causing the profiler to malfunction or by affecting the sand grain mobilization. We removed the top layer of sand, and regraded the beach in the manner described earlier. Then we ran the standard conditioning accretional waves to develop our

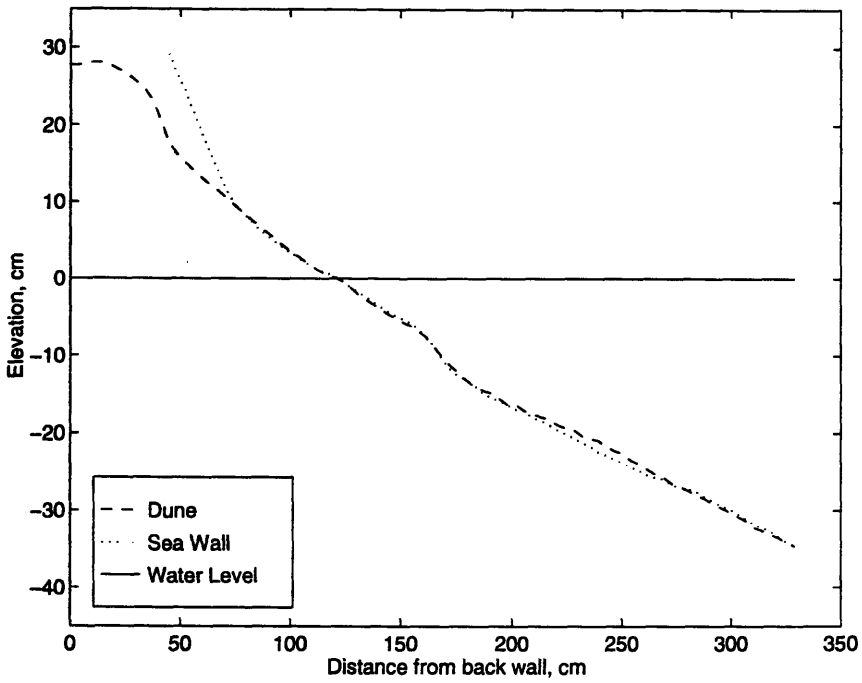


Figure 4-52: Profile plot of the initial beach before the extensive storm surge with beach interaction experiment.

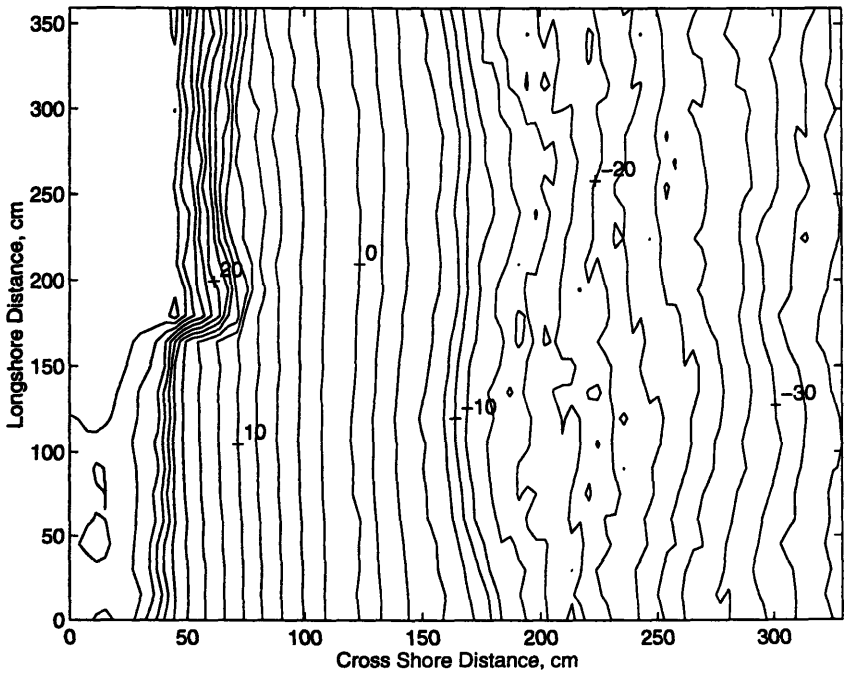


Figure 4-53: Contour plot with 2 cm contours of the beach before the extensive storm surge with interaction experiment.

Table 4.7: Equivalent wave conditions for extensive erosion with storm surge.

| Phase | $h$, (s) | $T_{eq}$, (s) | $H_{eq}$, (cm) | Duration, (min) | E or A |
|---|---|---|---|---|---|
| I | 58 | 1.40 | 6.8 | 30 | E |
| I | 58 | 1.06 | 6.6 | 30 | E |
| I | 58 | 1.39 | 7.5 | 30 | E |
| I | 58 | 1.08 | 7.0 | 30 | E |
| II | 62 | 1.40 | 8.1 | 20 | E |
| III | 58 | 1.41 | 7.8 | 20 | E |
| III | 58 | 1.42 | 7.9 | 20 | E |
| IV | 58 | 1.86 | 5.0 | 30 | A |
| IV | 58 | 2.33 | 3.8 | 30 | A |
| IV | 58 | 2.03 | 5.4 | 60 | A |
| IV | 58 | 2.02 | 5.3 | 60 | A |
| IV | 58 | 1.99 | 5.2 | 120 | A |

initial equilibrium profile. A profile plot of this initial beach condition, after the conditioning waves, is given in Figure 4-52 with a contour plot in Figure 4-53. The profile plots are constructed in the same manner used in in Section 4.5. It should be noted that there is some curvature to the underwater contours in this plot, especially in the $z = -10$ cm region. The below water profile on the sea wall side of the beach extends past the profile of the dune side, almost as if there is a hole or a deficit on the dune side of the experiment. This has consequences when we look at the net change over the duration of the experiment. The experiment began with an initial water depth, $h = 58$ cm.

### Phase I of Storm Surge with Interaction Experiment: Erosion before Storm Surge

The first phase of the sequence was erosion at the $h = 58$ cm water depth. This phase included the first four wave events given in Table 4.7. This sequence was intended to erode the shore area at the ambient water depth and form an off shore bar. The bar is built up until it protects the shore from further erosion during previous experiments. After this new equilibrium, an erosional limit, is reached, there is no more erosion unless the wave conditions or the water depth are changed. The results after the first set of waves and after the fourth set of waves are shown because there is an interesting progression. The eroded profile, after the first set of waves in phase I (i. e. $T_{eq} = 1.40$ s and $H_{eq} = 6.8$ cm for 30

min), is given in Figure 4-54 and the contour plot is given in Figure 4-55. The sand eroded from the dune is moved offshore in front of the dune and creates a larger berm on the dune side than on the sea wall side. The change in the beach is given in profile in Figure 4-56 and with contours in Figure 4-57. The contour plot shows clearly that the sand is moving directly offshore under the erosional wave action.

The results are slightly different by the end of phase I erosion. The profile and contour plots at the end of phase I are shown in Figures 4-58 and 4-59. These figures show significant long shore redistribution of sand from the dune to offshore from the sea wall. The toe of the sea wall at this point is just barely exposed, though this is difficult to see because of the measuring difficulty in the vicinity of the waterline. The berm in front of the sea wall is very pronounced and approximately 20 cm further offshore than the berm in front of the dune. Figure 4-60 is a profile plot and Figure 4-61 is a contour plot of the net change during phase I of the wave sequence. The profile plot does not show conservation of sand mass because the profiles are not averaged over the entire beach region, but only over the regions near the side walls. The contour plot of net change shows that there is significant erosion and deposition in the center region and that there is overall conservation, corresponding to a 0.2 cm sand layer, which is within the experimental error range. It is interesting that the eroded sand moved directly offshore during the first wave set but then moved diagonally offshore and deposited in front of the sea wall during the subsequent wave sets of phase I.

### Phase II of Storm Surge with Interaction Experiment: Erosion with Storm Surge

Phase II of the sequence involved raising the water level to $h = 62$ cm. We used a 4 cm storm surge because the berm restricting erosion was about 4 to 5 cm under water. Since the berm was definitely in the surf zone with $h = 58$ cm, the sea wall should be in the surf zone with $h = 62$ cm. With the raised water depth, some waves still broke on the offshore berm, but the sea wall was definitely in the surf zone. The greater depth allowed the waves to aggressively erode the dune while they pounded the sea wall. We had planned to run the erosional waves for 30 minutes, but decided to stop them after only 20 minutes because the dune was eroding too far. By the time we stopped the erosion, the top of the dune was eroded past where we are able to measure the beach. Figure 4-62 shows a profile of the eroded beach and Figure 4-63 shows a contour plot with a 2 cm contour interval. The beach

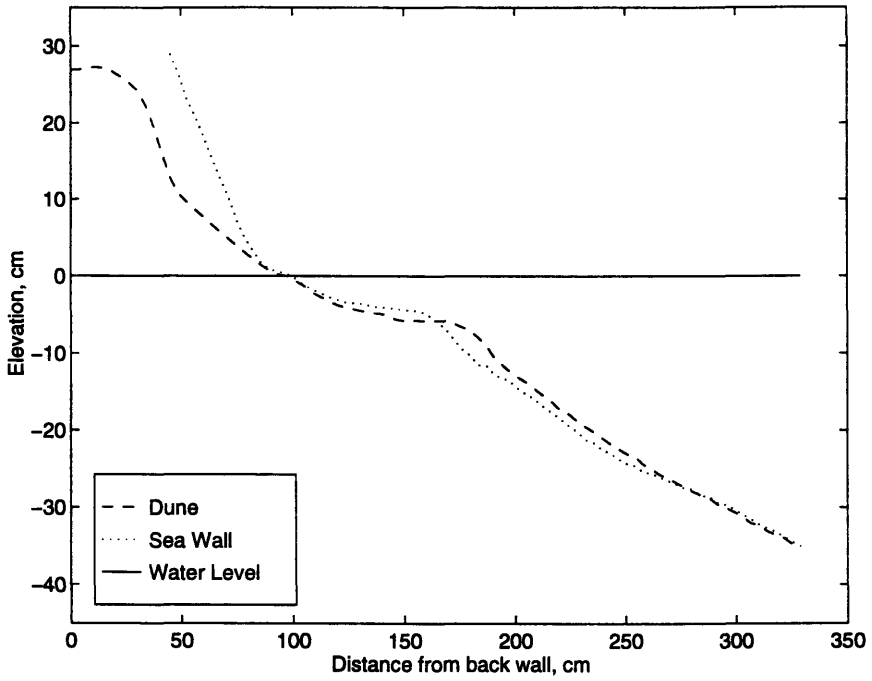


Figure 4-54: Profile plot of the beach in 4-52 after erosion for 30 min by $T_{eq}$ = 1.40 s, $H_{eq}$ = 6.8 cm waves.

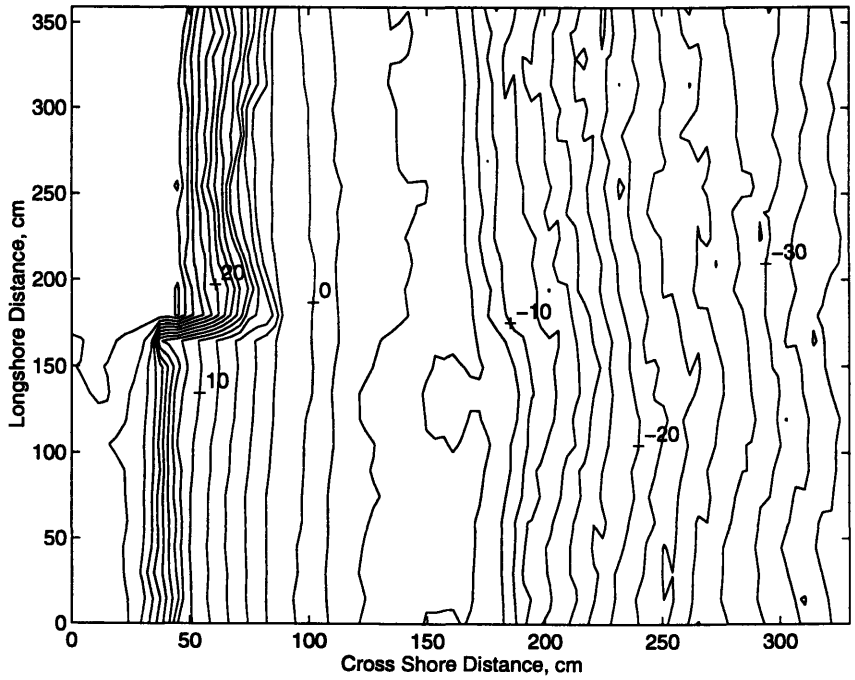


Figure 4-55: Contour plot with 2 cm contours of the beach in 4-53 after erosion for 30 min by $T_{eq}$ = 1.40 s, $H_{eq}$ = 6.8 cm waves.

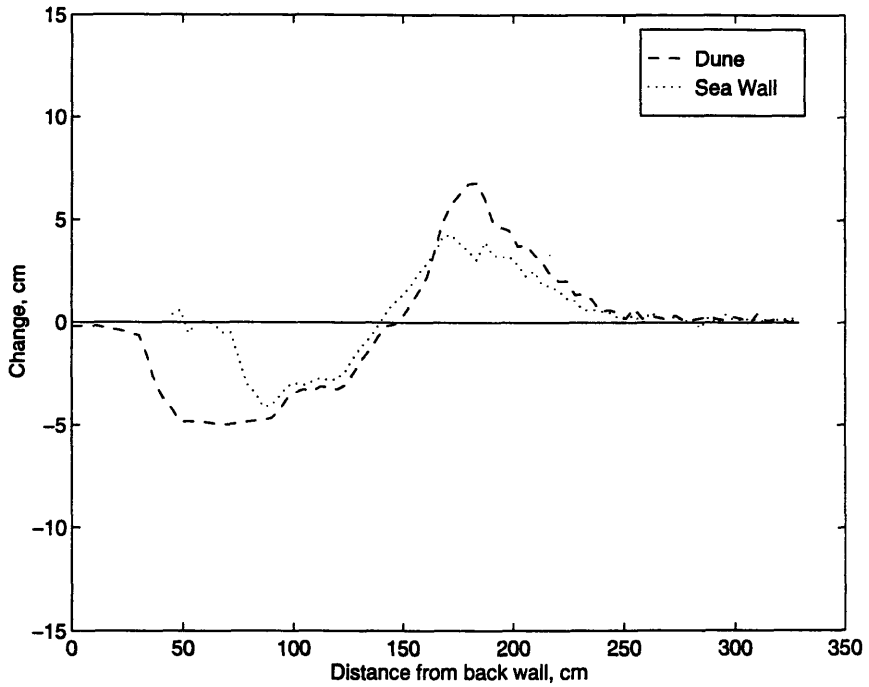


Figure 4-56: Profile plot of the erosion during 30 min of $T_{eq} = 1.40$ s, $H_{eq} = 6.8$ cm waves. Constructed by subtracting Figure 4-52 from 4-54.

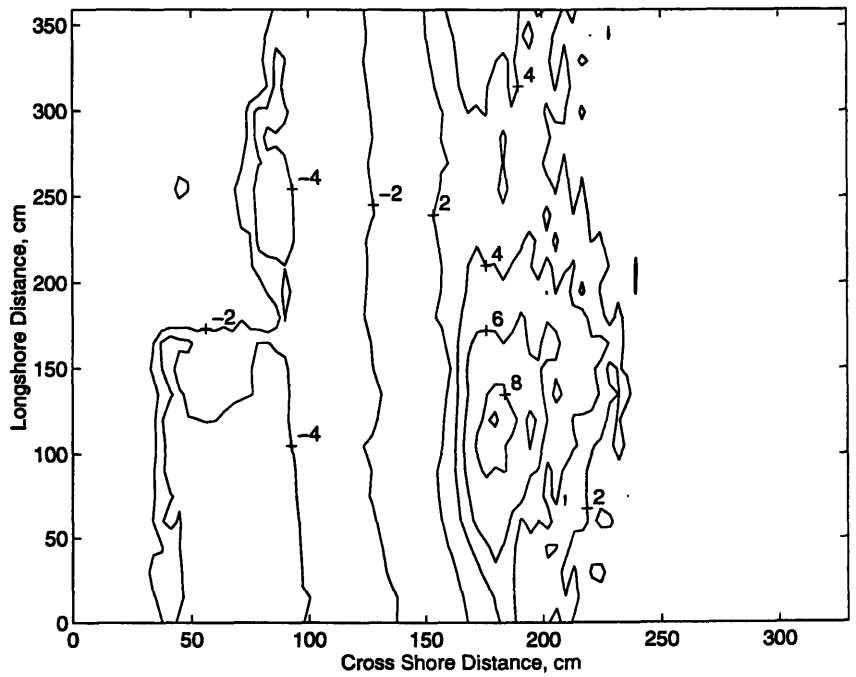


Figure 4-57: Contour plot of erosion during 30 min of $T_{eq} = 1.40$ s, $H_{eq} = 6.8$ cm waves. Constructed by subtracting Figure 4-53 from 4-55.

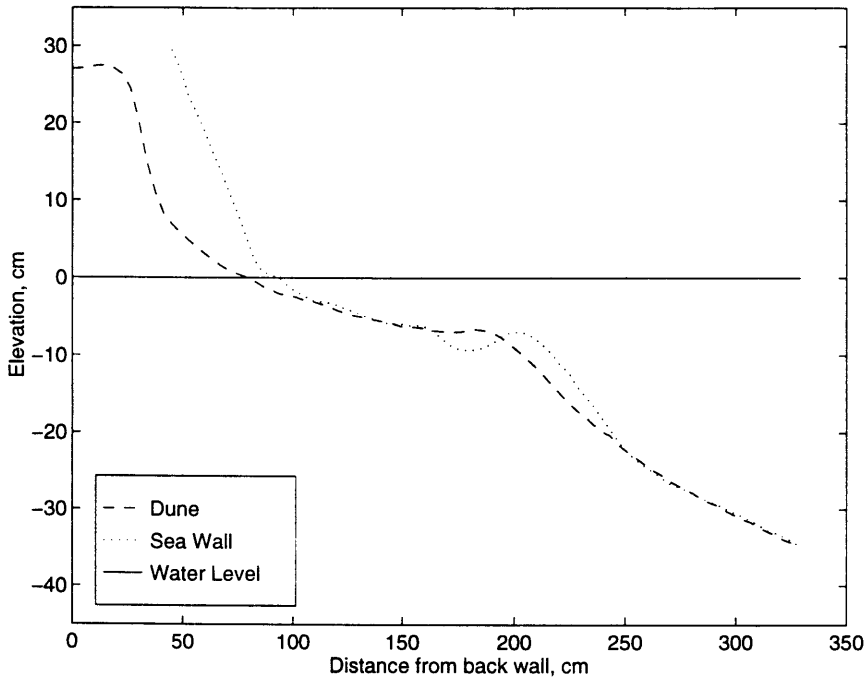


Figure 4-58: Profile plot of the beach in 4-52 after erosion during phase I of the wave sequence in Table 4.7.

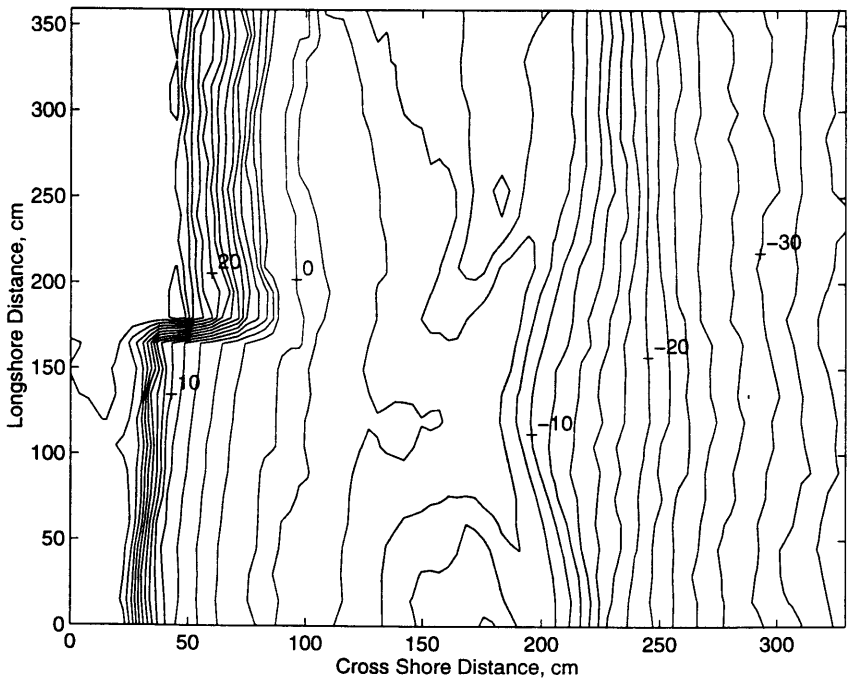


Figure 4-59: Contour plot with 2 cm contours of the beach in 4-53 after erosion during phase I of the wave sequence in Table 4.7.

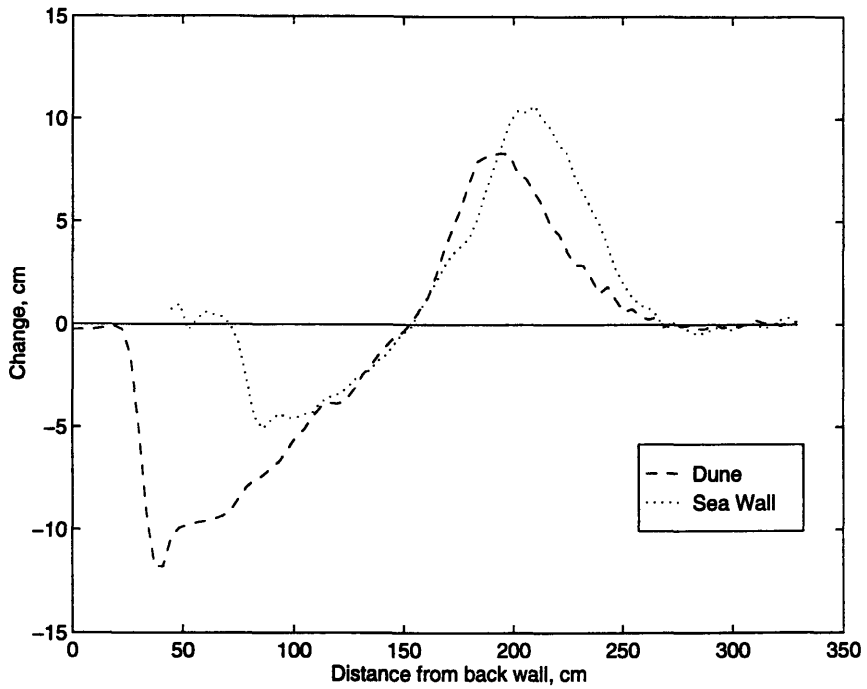


Figure 4-60: Profile plot of the erosion during phase I of the wave sequence in Table 4.7. Constructed by subtracting Figure 4-52 from 4-58.

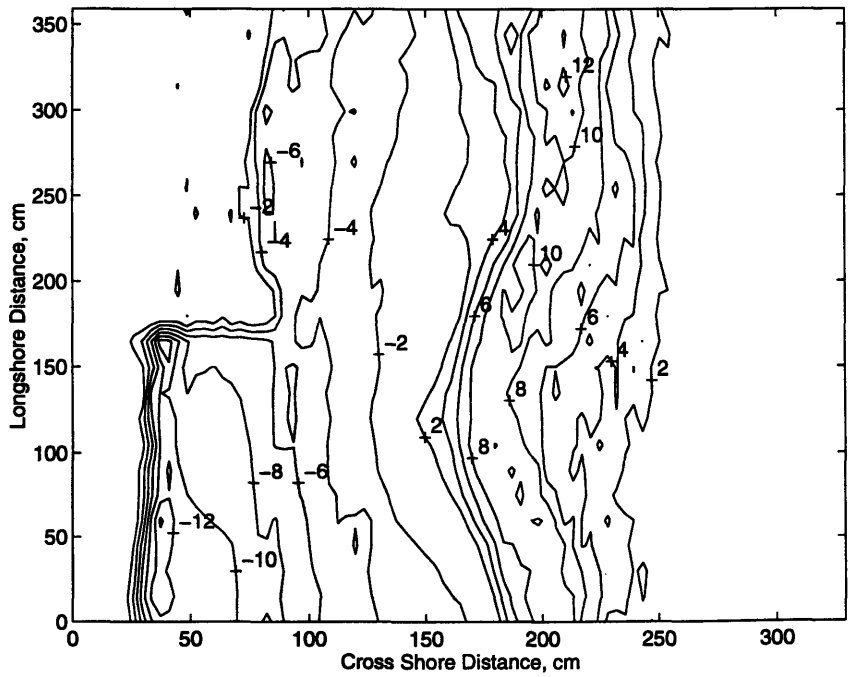


Figure 4-61: Contour plot of erosion during phase I of the wave sequence in Table 4.7. Constructed by subtracting Figure 4-53 from 4-59.

was measured with $h = 62$ as the reference point, but Figures 4-62 and 4-63 are shown with $z = 0$ at $h = 58$ for continuity. Despite the sea wall being in the surf zone with an exposed toe, the erosion at the toe of the sea wall was minor. Figure 4-64 and Figure 4-65 show a profile plot of beach change and a contour plot of beach shnge during phase II ersoion. The figures show that the dune has been seriously eroded while the sea wall beach has not changed greatly. To show this in another perspective, before and after profiles are shown for the dune and the sea wall in Figures 4-66 and 4-67 respectively. The dune has eroded with the sand forming a long, flat berm from $x = 130$ to $x = 170$ cm. The berm is further shoreward after phase II because of the elevated water depth during phase II erosion. The sea wall beach has some similarities in that the berm moved shoreward and was built up during phase II erosion. Dune erosion supplied the sand for the berm on the dune side of the beach, so there was enough sand for the long flat berm to form. The sea wall protected the dune on the sea wall side, so the sand supply for the berm was limited. There was not significant scour at the toe of the sea wall as anticipated. There merely a resdistribution of sediment in the surf zone. With continued erosion at the original SWL, one would expect the berm formed during phase II to move further offshore as an adjustment to the changing water depth.

### Phase III of Storm Surge with Interaction Experiment: Erosion at Original Water Depth

Figure 4-68 shows the beach in a profile plot and Figure 4-69 in a contour plot after phase III erosion with the wave conditions given in Table 4.7. At the lower water depth, the berm formed during the storm surge moved further offshore with very little change in the nearshore area. To illustrate this, Figure 4-70 shows the net beach change during phase III as a profile plot and Figure 4-71 shows this change with a contour plot. The region near $x = 150$ cm has eroded and the sediment has moved offshore past $x = 200$ cm. Figure 4-62, before phase III, shows the berm to be located at $x = 150$ cm. The erosion in phase III removed the sand from the berm, not from the base of the dune. The base of the dune and the base of the sea wall are essentially unchanged.

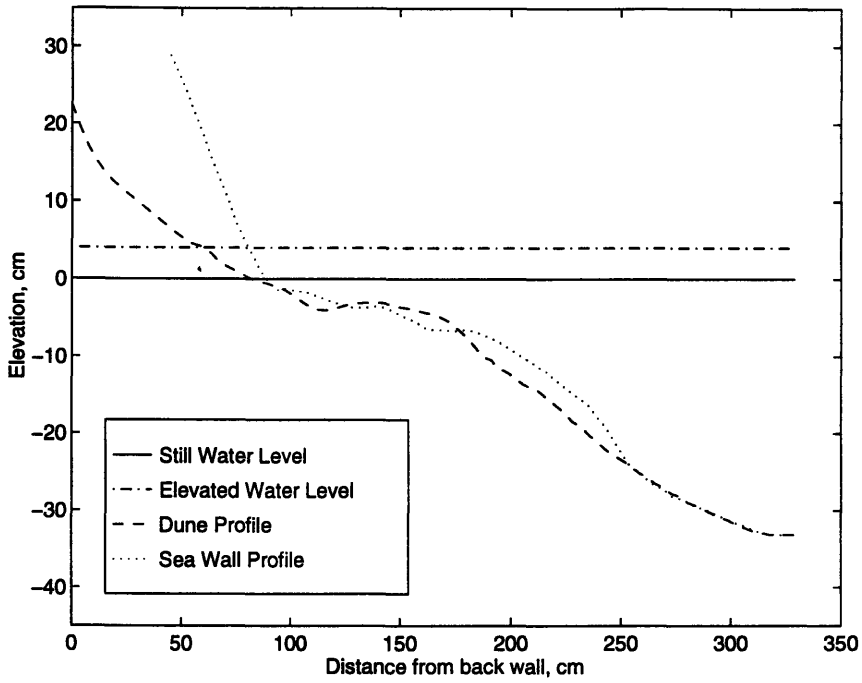


Figure 4-62: Profile plot of beach after erosion during phase II of the wave sequence in Table 4.7.

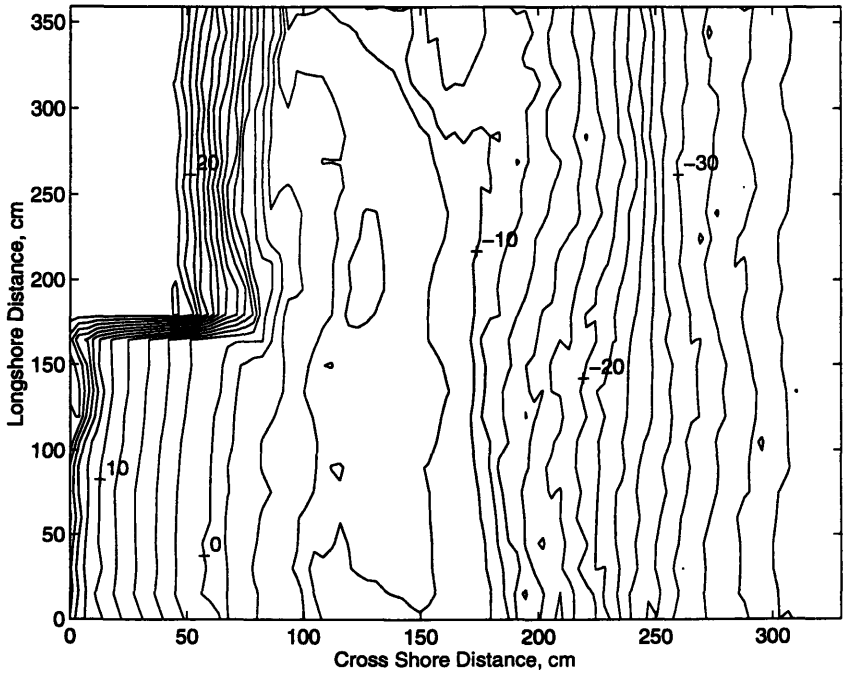


Figure 4-63: Contour plot of beach after erosion during phase II of the wave sequence in Table 4.7.

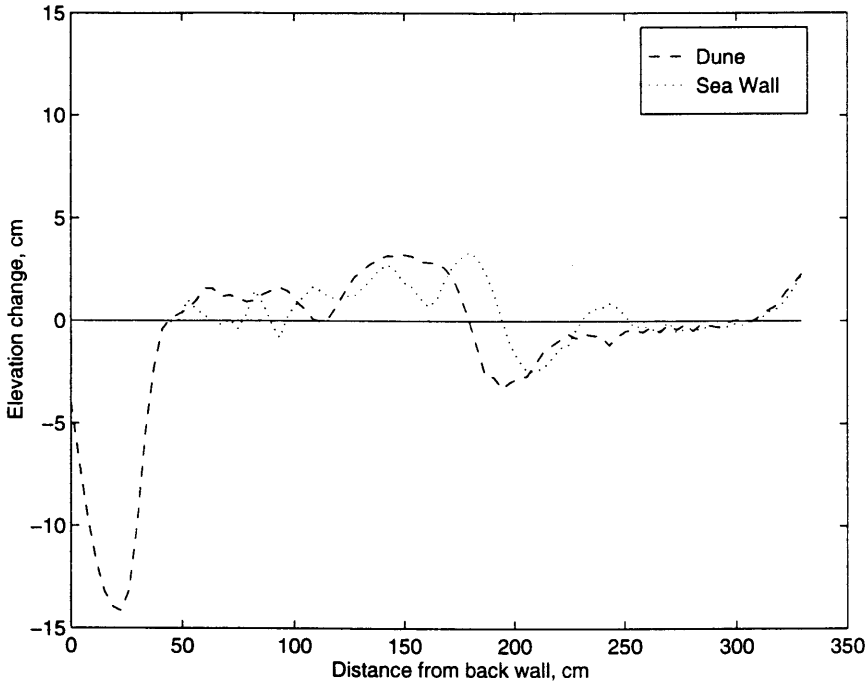


Figure 4-64: Profile Plot of erosion during phase II of the wave sequence in Table 4.7, constructed from 4-62 minus 4-58.

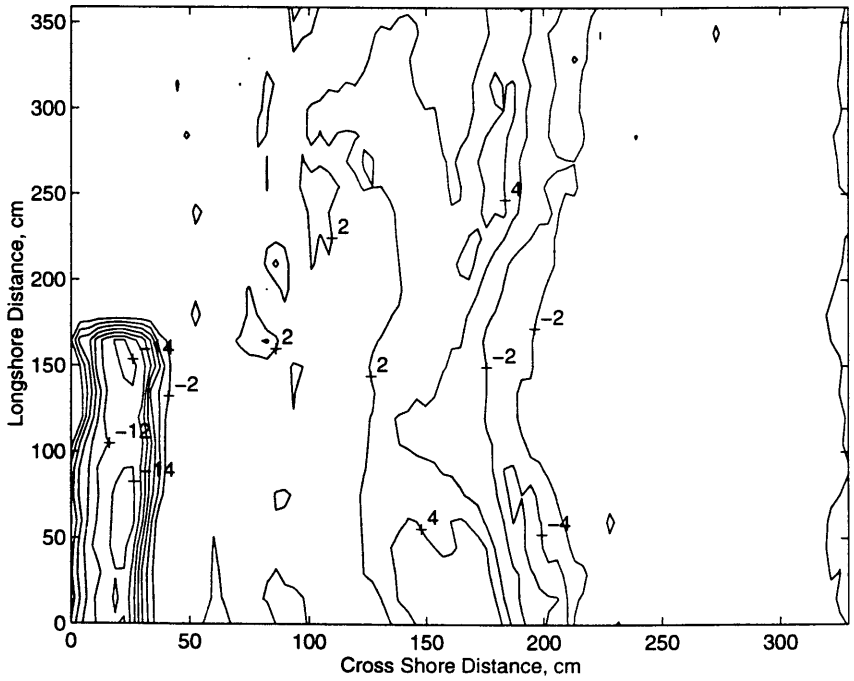


Figure 4-65: Contour plot of erosion during phase II of the wave sequence in Table 4.7, constructed from 4-63 minus 4-59.

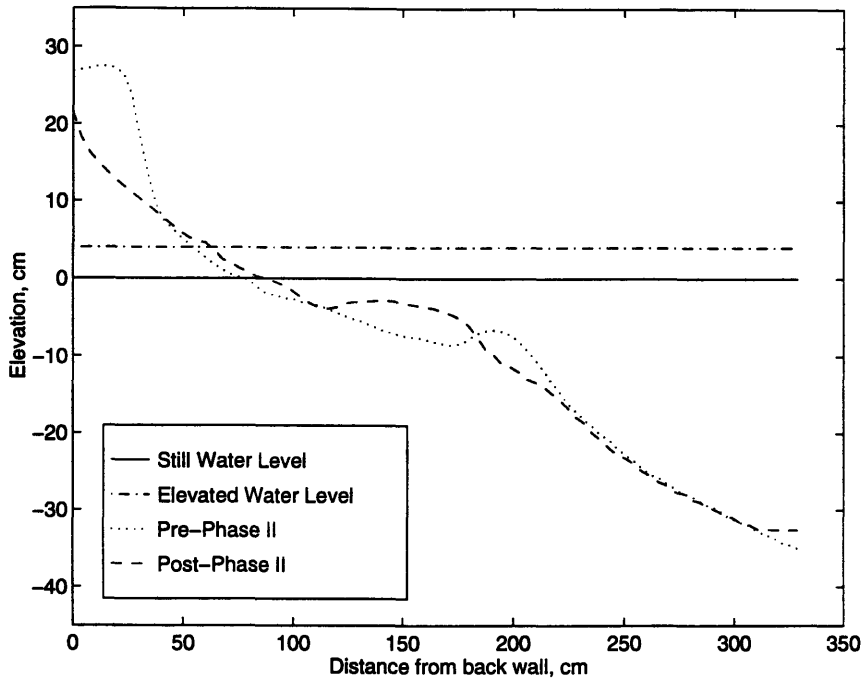


Figure 4-66: Averaged dune profiles before and after phase II of the wave sequence in Table 4.7, from Figures 4-62 and 4-58.

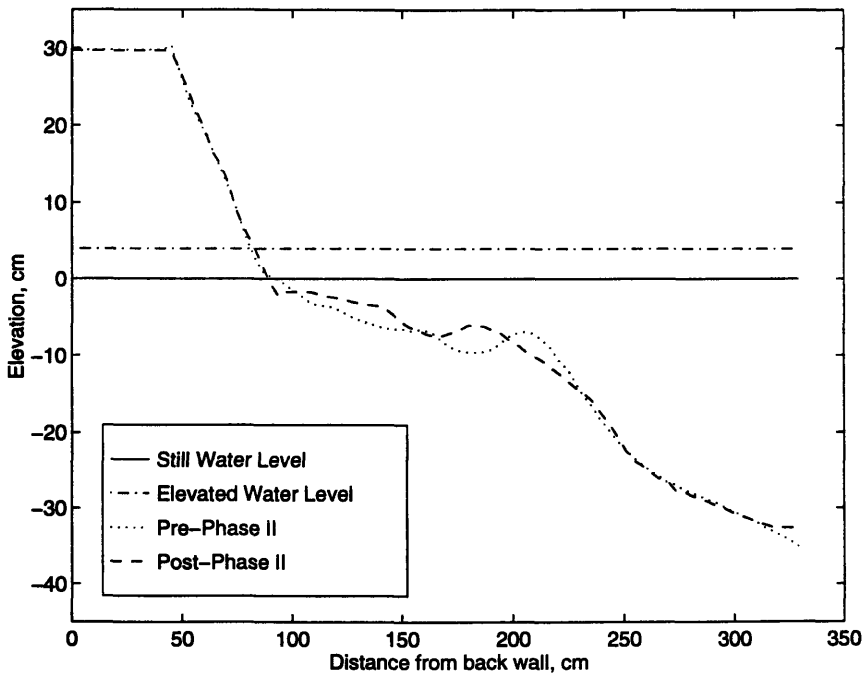


Figure 4-67: Averaged sea wall profiles before and after phase II of the wave sequence in Table 4.7, from Figures 4-62 and 4-58.

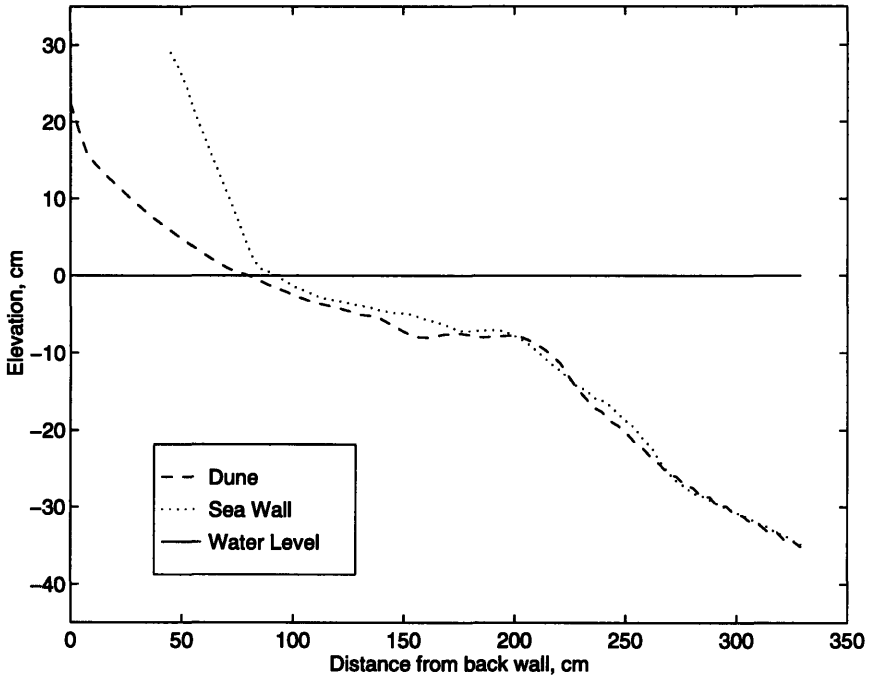


Figure 4-68: Profile plot after erosion during phase III of the wave sequence in Table 4.7.

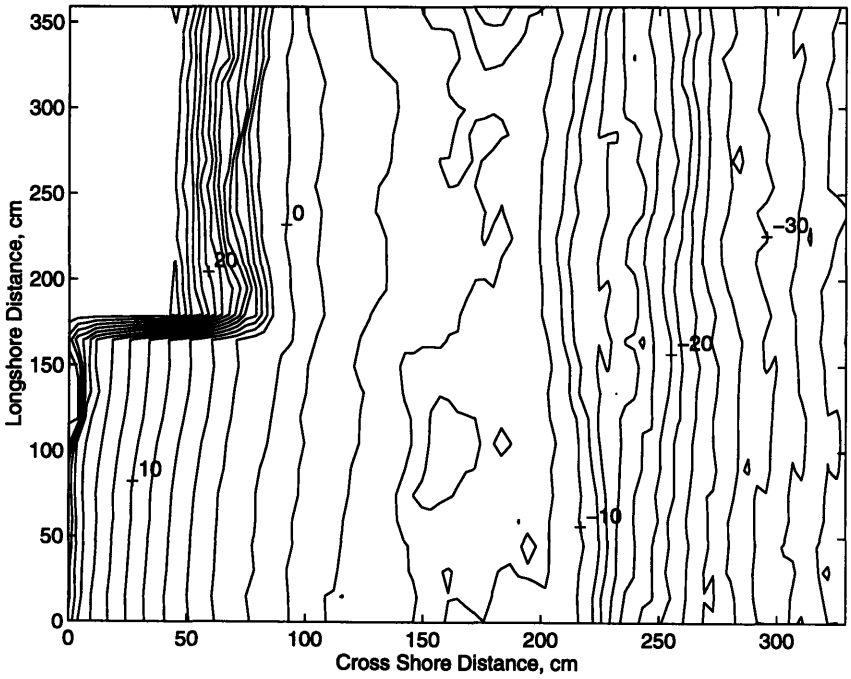


Figure 4-69: Contour plot with 2 cm contour interval after erosion during phase III of the wave sequence in Table 4.7.

### Phase IV of Storm Surge Erosion with Interaction Experiment: Recovery

After the beach was eroded in the first three phases, it was recovered with the standard recovery waves at the original water depth of $h = 58$ cm. The wave conditions for the recovery are given in phase IV of Table 4.7. One of the wave packets has a equivalent wave of $T_{eq} = 2.33$ s and $H_{eq} = 3.8$ cm, which is significantly different from the other wave events during phase IV. A software feature caused us to run the wrong waves during this wave event. The conditions were accretional, so the waves would have helped the recovery. The standard accretional waves were generated long enough before and after this set of waves that the effects of this rouge set of waves can be neglected.

The beach, after accretion during phase IV, is shown in a profile plot in Figure 4-72 and in a contour plot in Figure 4-73. There was a net erosion offshore on both beaches. From the contour plot in Figure 4-73, it appears as if the nearshore region, in the vicinity of the $z = -10$ cm contour line, that the dune beach has been able to recover further than the sea wall beach. The reason for this can be seen in Figure 4-74, which shows the net change of the beach profile during the entire experiment, and in Figure 4-75, which shows a contour plot of the net change. These plots were made by subtracting the initial beach surface, in Figure 4-53, from the final beach surface, in Figure 4-73. Both the dune and sea wall had a net erosion offshore. With the sea wall to fix the sea wall beach, the erosion and deposition on the sea wall beach occurred offshore. The erosion took place from approximately $x = 110$ cm to $x = 200$ cm with deposition between $x = 200$ cm and $x = 280$ cm. The dune profile looks similar to the sea wall beach for $x > 220$ cm or for $z < -20$ cm, but looks very different otherwise. The dune has a net deposition from $x = 110$ cm to $x = 200$ cm, where the sea wall beach experiences erosion. The excess sand deposited came from the large amount of sand eroded from the dune. The fact that the dune beach looks like it has recovered better than the sea wall beach is due to the large loss of sediment from the dune.

Before running this experiment with a storm surge and extensive erosion, we expected that there would be significant scour at the toe of the sea wall. We expected erosion with a water depth change would transport the sand far enough offshore that the sand would be lost to the system and the beaches would not recover. To some extent, this did happen. As shown in Figure 4-74 as a profile and in Figure 4-75 as a contour plot, there was a net

transport offshore for both beaches. The nearshore region in front of the sea wall was eroded by the severe storm simulation, but then was able to recover eventually with a relatively small net change. The dune beach experienced a much more drastic net change, with much of the dune being transported offshore and lost. The nearshore region in front of the dune appears to have recovered better than the nearshore region in front of the dune, but the recovery is largely due to the large erosional loss experienced by the dune. The net result is that the severe storm simulation moved sand from the dune to fill in the beach profile in the surf zone.

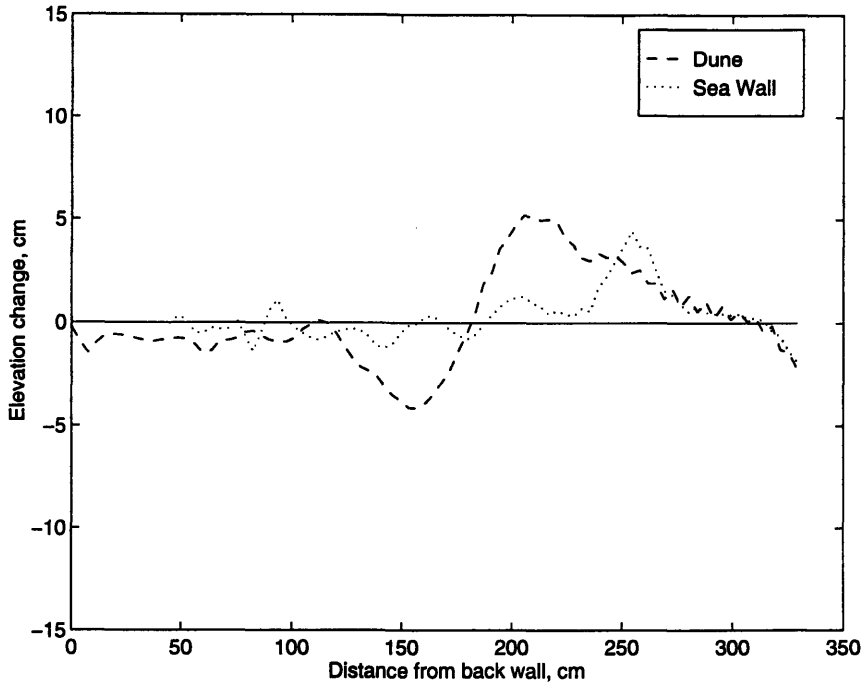


Figure 4-70: Profile plot of change during phase III: erosion at $h = 58$ cm with the wave conditions in Table 4.7. Plot obtained by subtracting Figure 4-62 from 4-68.

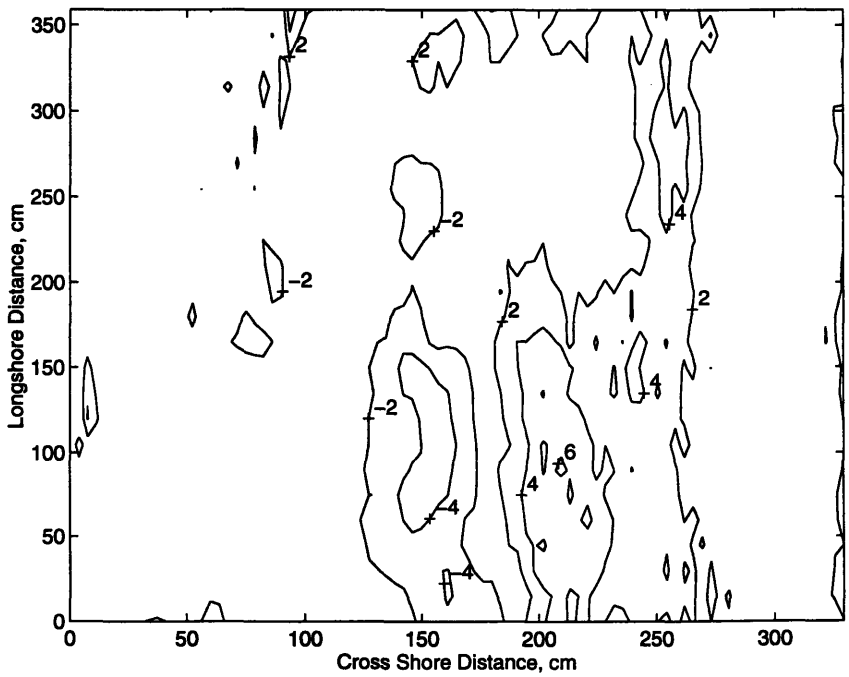


Figure 4-71: Contour plot of change during phase III: erosion at $h = 58$ cm with the wave conditions in Table 4.7. Plot obtained by subtracting Figure 4-63 from 4-69.

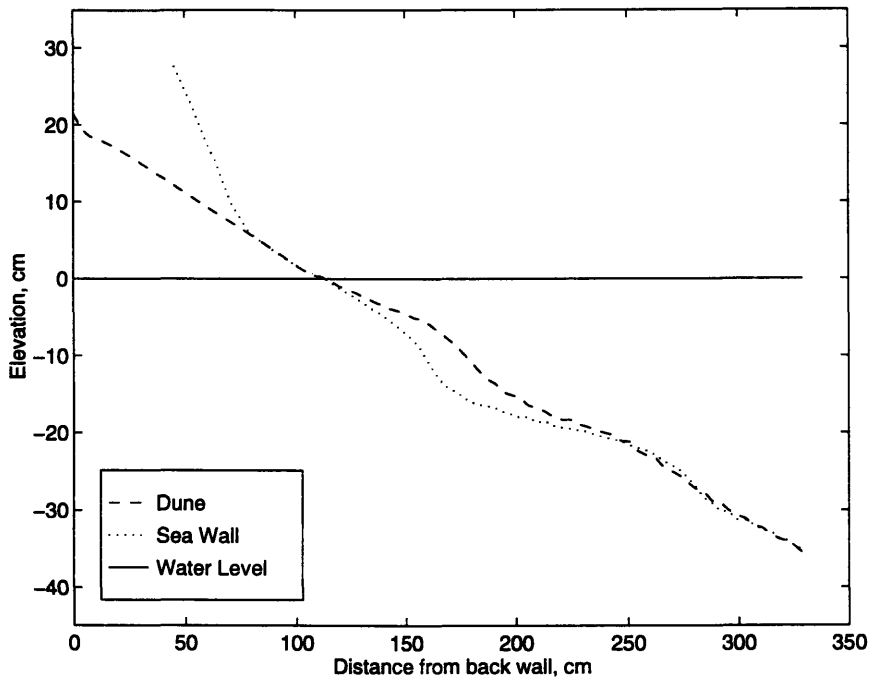


Figure 4-72: Profile plot of beach after recovery during phase IV of waves listed in Table 4.7.

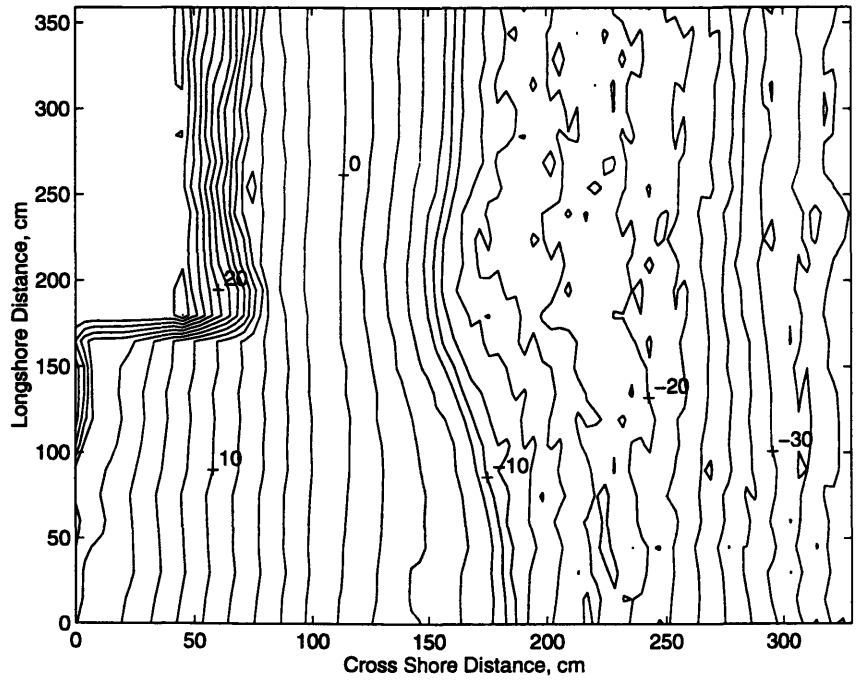


Figure 4-73: Contour plot with a 2 cm contour interval of beach after recovery during phase IV of waves listed in Table 4.7.

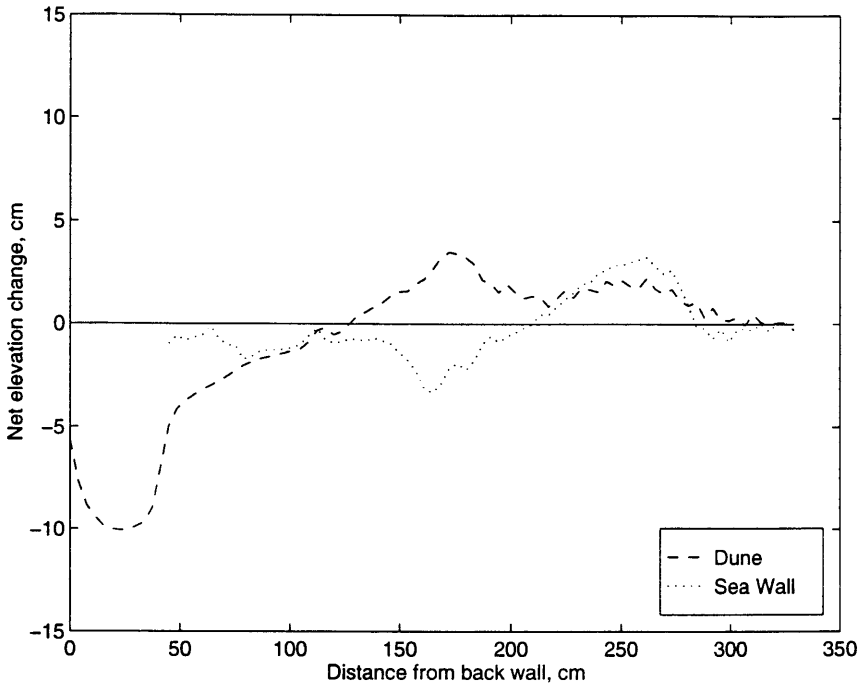


Figure 4-74: Profile plot of the net beach change during the storm surge with interaction experiment. Figure generated by subtracting Figure 4-52 from 4-72.

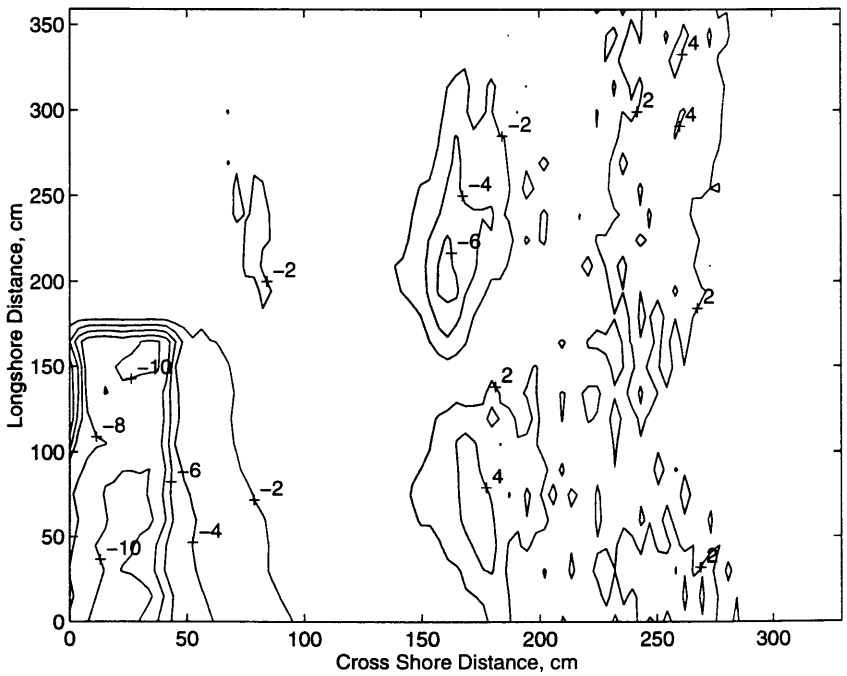


Figure 4-75: Contour plot of the net beach change during the storm surge with interaction experiment. Figure generated by subtracting Figure 4-53 from 4-73.

# Chapter 5

# Conclusions

Within the field of coastal engineering, there has been much interest in how sea walls interact with beaches. As coastal property is developed and threatened by storms, there is an increasing pressure to armor the shoreline against erosion. There is an opposing faction that says armoring beaches disrupts natural beach cycles and fluxes and disturbs the coastal environment. While conducting this experiment, we were asked whether we found sea walls to be good or bad, but there is no definitive answer to that question. Sea walls are designed to protect shoreline property. When designed properly, they are very effective at preventing erosion. They have potential for adversely affecting the immediate and adjacent beaches by interrupting longshore sand transport and cutting off sand supply for the beach, so they could be good or bad depending on ones perspective. This study was designed to explore the interactions between sea walls and the beaches in a small-scale laboratory setting in order to better understand how beaches with sea walls behave.

This study was a series of wave sequences involving erosion and accretion with different wave conditions and water depths to explore how the beaches reacted to varying wave conditions. All of the experiments were conducted with normally incident waves. This was a simplification, so that there was one less variable in this initial study into sea wall and beach interaction. It was also an externally applied restriction based on the fact that we were sharing the basin with two other research groups, hence we had limited space. Also, the capability to generate directional, multi-component waves is still under development. Limiting the study to normally incident waves allowed us to isolate the cross shore effects. Later investigations in the basin will be able to add the longshore dimension.

Several wave sequences were conducted with the sea wall and dune beaches separated with a dividing wall so that the two beaches would be subjected to the the same wave conditions to see how they reacted differently. For relatively small erosion and accretion events, the two beaches behaved nearly identically. The only difference was that the sea wall successfully trapped the sediment so the beach on the sea wall side did not erode as much, on a volume basis, as the unprotected beach. This has been seen before and is recognized as Dean's approximate principle, which says that the volume eroded in front of a sea wall is less than or equal to the volume eroded from a dune subject to the same conditions under two dimensional conditions. Based on the Dean's principle, we were expecting the beach in front of the sea wall to be significantly eroded with the eroded volume the same order of magnitude as the volume eroded from the dune, but this was not the case. The two beaches were nearly identical seaward of the sea wall; there was no additional or excess erosion in the sea wall profile to match the erosion from the dune. Also, it is interesting that the erosion and recovery rates for the two beaches were almost identical. For smaller events, both beaches recovered nearly completely to their original profiles.

During more extensive erosion and accretion sequences with longer erosional durations and larger waves, there was permanent beach change. During the sequences where waves were able to erode past the foreshore and start eroding into the dune, there was some permanent loss from the dune to the offshore region. For the dune beach, the subaerial profile experienced profile deflation with the eroded sand being deposited in the subaqueous region. Since this laboratory model does not include wind erosion or deposition, there is no way to rebuild the dune after it is eroded. On the sea wall side, there was significant erosion in the nearshore region, with the waterline eroding back to the toe of the sea wall. For several experiments, the sea wall was far enough back from the surf zone that there was erosion, but there was no significant scour, at the toe of the sea wall. Again, the profiles seaward of the base of the sea wall were nearly identical, showing no excess erosion due to the presence of the sea wall. This could partially be due to the relatively "soft" rubble mound sea wall. The sea wall beach exhibited a consistently lower reflection coefficient than the dune beach throughout the experiment. Kraus (1988) says that there is some evidence that softer structures, i. e. with lower reflection coefficients, tend to behave better in that they have less scour during erosion and recover faster during accretion. Kraus and McDougal (1995) question this conclusion, but there still is no definitive answer. During

erosion, the sediment moved from the toe of the sea wall to form an offshore berm in the surf zone. In the extensive erosion experiments, some of this sediment was not recovered on the sea wall side, but the amount of recovery on the sea wall side was greater than it was on the dune side.

After several experiments with the sea wall and dune beaches isolated with a dividing wall, the wall was removed and the interactions between the two beaches were examined. Longshore sediment transport is caused by longshore currents, which are driven by non-normally incident waves. Since the waves were normally incident and there was no longshore current, the transport was more of a sediment redistribution and was probably influenced by the circulation currents artificially introduced by conducting the experiment in the basin. Therefore, the conclusions that we are able to draw from the interaction experiments are somewhat limited. With this caveat, we can look at the results. During small scale erosion with interaction, the beaches behaved nearly identically to the way they they did without interaction. Erosion caused the nearshore sediment to move offshore and form a protective berm with nearly identical eroded profiles seaward of the base of the sea wall for both beaches. The beach remained relatively uniform across. The beaches recovered at the same rate and both returned to their initial profiles, which are identical.

For the extensive erosion sequence, the results are a little more interesting. When the beach eroded, the erosion was uniform in the longshore direction until the waves started eroding past the sea wall. The sea wall prevented erosion on half of the beach, while the waves continued to erode the nearshore region and eventually the dune on the other half of the beach. The offshore berm built up on both sides with some curvature along the beach. There was no evidence of flanking, which is usually attributed to longshore transport. Looking at the sediment redistribution, given in Figure 4-47, it is noticed that part of the sediment eroded from the dune was deposited directly offshore in front of the dune but there was a significant longshore redistribution that deposited some of the dune sand in front of the sea wall. During recovery, the sediment on both sides was brought back onshore with full recovery on the sea wall half of the beach and partial recovery on the dune half. The nearshore region recovered fully to the same initial beach width, but there was a permanent loss from the dune to the offshore region.

The last experiment combined the large waves and extensive erosion described in the experiment above with a 4 cm storm surge for the heaviest erosion of the entire study.

During the erosion, the dune was eroded back severely with the sediment initially being deposited directly offshore. The beach was eroded before the storm surge, so when the surge was added, the sea wall was actively in the surf zone. Despite the sea wall being fully in the surf zone, we still did not notice a significant scour at the base of the sea wall. The sediment from the dune was partially redistributed in front of the sea wall as erosion continued. After the storm surge subsided, we continued to generate erosional waves which moved the sediment in the offshore berm further offshore, so that some sediment was permanently lost from the nearshore system. Most of the sand that was eroded from the nearshore region was successfully recovered but the sediment eroded from the dune was deposited far enough offshore that it was unrecoverable. The simulated storm had the unexpected effect of making the dune half of the beach appear to recover better than the sea wall half, but this is a deceptive result. The extreme storm eroded a major portion of the dune that backed the beach, which was eventually deposited in the nearshore and offshore regions. The region in front of the dune was recovered better than in front of the sea wall because of the sediment supplied by the dune. The sea wall side did not have this large supply of sediment, hence it appeared not to have recovered as well. In reality, the protected beach fared remarkably well. The beach in front of the sea wall was not permanently lost, compared to a large permanent dune erosion of the unprotected beach.

There has been a flurry of laboratory research and field monitoring studies into sea walls recently as documented by Kraus (1988) and Kraus and McDougal (1995). However, there is still much work to be done to understand how sea walls interact with the immediate and adjacent beaches. An area of research that needs to be expanded upon is three dimensional laboratory experiments. The J. Robert Gunther Family Ocean Wave Facility located in the Parsons Laboratory at MIT is well equipped to perform in depth three dimensional studies into sea wall and beach interaction experiments or other similar studies.

Currently, the basin is shared between three research groups with each group using a section of the basin for one or two months at a time. Since the facility has only recently come on line, the experiments in the basin currently are initial studies that are relatively small and simple. As these studies yield results, the basin usage paradigm needs to change. Relatively small two dimensional studies should lead to larger three-dimensional studies that utilize the entire basin. This would require the basin to be used by a single research group for six months to a year at a time to take advantage of the size and flexibility of the

basin.

The operating system for the wavemaker is adequate for the experiments that we have done, but it is insufficient for the projects that we foresee. The IBM PS2 running the wavemaker is inadequate in both speed and memory to generate anything more complicated than a plane directional wave or a normally incident spectral wave. We are currently in the process of upgrading the operating system to a Pentium 100 based computer which has the speed and memory required to generate directional spectral waves. This is in conjunction with software development by Hoang Tran to develop a data collection. Together, the two programs will enable wave generation and data collection on one computer. There is still more development work required before the wave maker is able to generate multi-component, multi-directional waves, but the potential is there.

A significant part of the research on this project was the design, construction and development of the beach measurement system, consisting of the X-Y plotter and the Masatoyo bed profiler. The combination provided the ability to obtain beach surveys with great precision, allowing us to perform detailed analysis on the beach morphology.

The system is highly accurate and very versatile, making it an excellent tool for further experiments in the basin. The X-Y plotter can be positioned anywhere within its measurement area with a precision better than 1 mm. The instrument table is designed to hold the bed profiler, but it could be used to hold wave gauges, cameras, lasers or any other instrument that one would want to position and move precisely. The measurement area currently is 3.8 m by 3.8 m, but this could be expanded very easily in one direction by extending the beams, rails and gear racks that support the cross beam to any length desired without forfeiting accuracy or performance. To extend the plotter in the other direction would require rebuilding most of the plotter, which would not be as feasible. Also, the bed profiler is an excellent measurement tool for almost any movable bed experiments.

This small-scale laboratory investigation showed that beaches protected with sea walls behave as well as unprotected beaches under the limiting conditions of normally incident spectral waves. When the beaches were allowed to interact, there was some interaction, but this can partially be attributed to artificial circulation currents in the basin. This study provided some interesting results which are worth exploring further using non-normally incident waves in a larger portion of the wave basin. By isolating the cross shore behavior, we can say, with some certainty, that the cross shore behavior of protected and unprotected

beaches is very similar, except under the most extreme storm conditions where the unprotected beach can be severely and permanently eroded. The effect of adding longshore transport due to longshore currents still needs to be researched.

This study does not attempt to conclude that sea walls are "good" or "bad", but does state that they can be beneficial when used properly as part of a coastal zone management plan. We have found that the beaches in front of sea walls behave nearly identically to unprotected beaches in anything but the most severe storms. Under extreme conditions, the sea walls protect the headland from major erosional loss, which is a significant benefit. Erecting a sea wall on a beach does not condemn the immediate or adjacent beaches. Sea walls are not the answer to every shore erosion problem, but they are effective at protecting coastal property.

# Bibliography

**Dalrymple, R.A. 1992.** Prediction of Storm/Normal Beach Profiles. *J. Waterway, Port, Coastal, Ocean Engrg.*, Vol. 118, No. 2, 193-201.

**Dean, R.G. 1973.** Heuristic Models of Sand Transport in the Surf Zone. *Proc. Conf. on Engrg. Dynamics in Surf Zone,* Sydney, Autrailia, 208-214.

**Dean, R.G. 1986.** Coastal Armoring: Effects, Principles, and Mitigation. *Proc. 20th Coastal Engrg. Conf.,* ASCE, 1843-1857.

*DMC-1000 Technical Reference Guide.* **1994.** Version 1.3, Galil Motion Control, Inc.

**Griggs, G.B., Tait, J.F., and Scott, K. 1990.** The Impacts of Shoreline Protection Structures on Beaches Along Monterey Bay, California. *Proc. 22nd Coastal Engrg. Conf.,* ASCE, 2810-2823.

**Griggs, G.B., Tait, J.F., Scott, K., and Plant, N. 1991.** The Interaction of Seawalls and Beaches: Four Years of Field Monitoring, Monterey Bay, California. *Proc. Coastal Sediments, '91,* ASCE, 1871-1885.

**Hasselmann, K. et. al 1973.** Measurements of Wind-Wave Growth and Swell Decay During the Joint North Sea Wave Project (JONSWAP). *Deutsche Hydrographische Zeitschrift,* Ergänzungsheft Reihe A(8°), Nr. 12, 1-95.

**Irie, I. and Nadaoka, K. 1985.** Laboratory Reproduction of Seabed Scour in Front of Breakwaters. *Proc. 19th Coastal Engrg. Conf.,* ASCE, 1715-1731.

**Ito, M. and Tsuchiya, Y. 1984.** Scale-Model Relationship of Beach Profile. *Proc. 19th Coastal Engrg. Conf.,* ASCE, 1386-1402.

**Ito, M. and Tsuchiya, Y. 1986.** Time Scale for Modelling Beach Change. *Proc. 20th Coastal Engrg. Conf.,* ASCE, 1196-1209.

**Iwagaki, Y. and Noda, H. 1962.** Laboratory Studies of Scale Effects in Two-Dimensional Beach Processes. *Proc. 8th Coastal Engrg. Conf.,* ASCE, 194-210.

**Jonsson, I.G. 1966.** Wave Boundary Layers and Friction Factors. *Proc. 10th Int. Coastal Engrg. Conf.,* ASCE, Vol. 1, 127-148.

**Kinsman, B. 1965** *Wind Waves, Their Generation and Propagation on the Ocean Surface.* Prentice-Hall, NJ.

**Kitaigorodskii, S.A., Krasitskii, V.P. and Zaslavskii, M.M. 1975.** On Phillip's Theory of the Equilibrium Range in the Spectra of Wind-Generated Waves. *J. Phys. Oceanogr.,* Vol. 5, 410-420.

**Kraus, N.C. 1987.** The Effects of Seawalls on the Beach: A Literature Review. *Proc. Coastal Sediments '87,* ASCE, 945-960.

**Kraus, N.C. 1988.** The Effects of Seawalls on the Beach: An Extended Literature Review. *J. Coastal Res.,* SI 4: 1-29.

**Kraus, N.C. and Larson, M. 1988.** Beach Profile Change Measured in the Tank for Large Waves, 1956-1957 and 1962. Tech. Rep. CERC-88-6, U.S. Army Coastal Engrg. Res. Cen., Vicksburg, Miss.

**Kraus, N.C. et. al 1991.** Evaluation of Beach erosion and Accretion Predictors. *Proc. Coastal Sediments '91,* ASCE, 572-587.

**Kraus, N.C. and McDougal, W.G. 1995.** The Effects of Seawalls on the Beach: Part I, An Updated Literature Review. *J. Coastal Res.,* (To appear in a special issue).

**Larson, M. and Kraus, N.C. 1989.** SBEACH: Numerical Model for Simulating Storm-Induced Beach Change. Report 1: Empirical Foundation and Model Development, Tech. Rep. CERC-89-9, U.S. Army Coastal Engrg. Res. Cen., Vicksburg, Miss.

**McDougal, W.G., Sturtevant, M.A., and Komar, P.D. 1987.** Laboratory and Field Investigations of the Impact of Shoreline Stabilization Stuctures on Adjacent Properties. *Proc. Coastal Sediments '87,* ASCE, 961-973.

**Madsen, O.S. 1971.** On the Generation of Long Waves. *J. Geophys. Res.*, Vol. 76, No. 36, 8672-8683.

**Madsen, O.S. and Grant, W.D. 1976.** Quantitative Description of Sediment Transport by Waves. *Proc. 15th Int. Coastal Engrg. Conf.* ASCE, Vol. 2, 1093-1112.

**Madsen, O.S. and Wikramanayake, P.N. 1991.** Simple Models for Turbulent Wave-Current Bottom Boundary Layer Flow. Contract Report No. DRP-91-1, U.S. Army Corps of Engineers, CERC.

**Madsen, O.S. 1994.** Spectral Wave-Current Bottom Boundary Layer Flows. *Proc. 24th Coastal Engrg. Conf.,* ASCE, 384-398.

**Mathisen, P.P. and Madsen, O.S. 1993** Bottom Roughness for Wave and Current Boundary Layer Flows Over a Rippled Bed. MIT Sea Grant, MITSG 93-27.

**Mei, C.C. 1989.** *The Applied Dynamics of Ocean Surface Waves.* World Scientific, Singapore.

**Oppenheim, A.V. 1975.** *Digital Signal Processing.* John Wiley and Sons, NY.

**Pierson, W.J. and Moskowitz, L. 1964.** A Proposed Spectral Form for Fully-Developed Wind Seas Based on the Theory of S.A. Kitaigorodskii. *J. Geophys. Res.*, Vol. 69, 5181-5190.

**Rosengaus, M. 1987.** *Experimental Study on Wave Generated Bedforms and Resulting Wave Attenuation.* Ph.D. Thesis, MIT.

**Sato, S., Tanake, N. and Irie, I. 1969.** Study on Scouring at the Foot of Coastal Structures. *Proc. 11th Coastal Engrg. Conf.,* ASCE, 579-598.

**Shields, A. 1936.** Application of Simmilarity Principles and Turbulent Research to Bed-Load Movement. (Translated of original German by W.P. Ott and J.C. van Uchelen, Cal. Tech.) *Mitteilungen der Preussischen Versuchsanstalt für Wasserbau und Schiffbau.*

*Shore Protection Manual.* **1984.** 4th ed., 2 vols, U. S. Army Engineer Waterways Experiment Station, Coastal Engrg. Res. Ctr., U. S. Government Printing Office, Washington, DC.

**Skovgaard, O. et. al 1974.** *Sinusoidal and Cnoidal Gravity Waves: Tables and Formulae.* Inst. Hydrodyn. and Hydraulic Engrg., Tech. Univ. Denmark.

**Tait, J.F. and Griggs, G.B. 1990.** Beach Response to the Presence of a Seawall. *Shore and Beach,* 58(2): 11-28.

**Tran, H.H. 1994** *Software Development for the Gunther Wave Basin.* S.B. Thesis, MIT.

**Trowbridge, J.H. and Madsen, O.S. 1984.** Turbulent Boundary Layers. *J. Geophys. Res.,* Vol. 89, No. C5, 7989-8007.

**Whitham, G.B. 1974.** *Linear and Nonlinear Waves.* John Wiley and Sons, NY.

# Appendix A

# Design of X-Y Plotter

This section is included to document the design and construction of the X-Y plotter. The plotter is a unique and powerful research tool that will be useful for many different projects. The design and construction of the plotter was complex enough that it required the help of two outside consultants, Bruce Parks to help with the design and Jack Crocker to help with the construction. For clarity, dimensions in this section are in English units.

Bruce Parks, of Eastern Bearings, helped with much of the preliminary work of getting the design headed in the right direction. Initially, Bruce Parks supplied parts catalogs and a basic design. Using this, the design was finalized and parts ordered through Bruce Parks. This was not the ideal way to order the parts because of the delays associated with ordering through a third party. Direct ordering, where possible, is quicker and more reliable. Bruce Parks was helpful in a few critical areas of design, especially in motion control. He supplied the stepper motors and the motion control card and software to run the plotter from a PC. The motor controller is made by Galil. It has two axis independent motion control, 8 analog inputs, 8 digital outputs, and 7 digital inputs. It is programmable in its own programming language with libraries to interface with C and other programming languages.

A second consultant, Jack Crocker, was hired to build the plotter. Jack Crocker was the Parson's Lab machinist for several years and was closely involved in the wavemaker construction. Jack Crocker is a highly skilled machinist and proved indispensable in building the plotter. His insight and experience enabled the actual construction to proceed rapidly and efficiently.

A plan view of the plotter is given in Figure 3-4 showing the basic design. Essentially

the plotter consists of a 16 ft. by 14 ft. rectangular frame with rails and gear racks along the 16 ft. beams. The 14 ft. beams attach at the end of the 16. beams such that the actual plotter size is 14 ft. by 16 ft. 8 in. Across the frame is a 14 ft. cross beam with a pair of rails and another gear rack, which the sensor platform rides on. The motor for the crossbeam is mounted on the crossbeam and the motor for the platform is mounted on the platform.

The beams of the frame are 4 in. square aluminum tubing with 3/8 in. thickness. Tubing was chosen because it is easy to attach components to since it has flat faces on each side. The beams were purchased cut to length from Industrial Aluminum Co.

The corners of the rectangular frame are sandwiched between 1/2 in. thick, triangular, aluminum plates and held in place with bolts. It is not permanently attached so that it can be taken apart and either stored or modified. Bolted to the bottom of the plate at each corner are the supports. The supports are telescoping steel jack posts available commercially from McMaster-Carr Supply Company. The posts are adjustable so that the frame can be leveled by hand.

The gear rack and rails were ordered separately and assembled here. Apparently, there are prefabricated gear rack and rail assemblies available, which could have saved considerable time and labor costs. If the plotter is expanded, this option should be looked into. The rails were bought from a company called INA Linear Technik Inc. We chose the precision hardened and ground shafting for performance and durability. 1/2 in. shafts were used since the applied load is relatively small. For convenience, we used the predrilled and tapped shafts. INA also supplied the predrilled shaft supports that support the rails. The part number for the rails is WZ 1/2 PDT and the number for the rail supports is TSUZ 08 PD.

There were several options available for the drive system, but the one that gave good accuracy for a reasonable price was a spur gear and gear rack drive. This system is relatively inexpensive and requires very little maintenance. The spur gears and gear racks are both available from Browning. Eastern Bearings had the racks drilled and tapped, which contributed to the supply delay. This is one of the reasons that the prefabricated gear rack and rail assemblies are worth considering if the system is expanded. The part number for the gear rack is NSR20x3/8 and the part number for the spur gear is NSS2030. The drive shafts used are 1/2 in. diameter, so the spur gears needed to be bored to 1/2 in. with a hole drilled and tapped for a set screw to hold the gear in place.

Pillow blocks are used to attach the beams to the rails. The pillow blocks were supplied locally by Atlantic Tracy Inc. and manufactured by Thomson. The part number for the single pillow block is SPB-8-OPN and for the twin pillow block is TWN-8-OPN. The bearings occasionally require a light application of machine oil to keep lubricated. With all the dust in the basin, the rails should be cleaned with machine oil periodically to maintain good performance. There are replacement bearings available through Atlantic Tracy in case the bearings inside the pillow blocks wear out.

Figure A-1 shows a side view and Figure A-2 shows a plan view of how the crossbeam is mounted on the frame. The beam is mounted on a twin pillow block which rides on the rail. The drive shaft is held in place with a bearing mounted on the crossbeam, part number VPS-208 from Browning. The rails and the gear rack are mounted on a 1/2 in. thick, 4 in. wide plate. The aluminum plate was purchased at Pierce Aluminum. Both components attach from the bottom, so the plate had to be drilled and the holes had to be countersunk so the plate would lie flat on the beam. Then the plate was attached to the beam with flat head screws with the holes countersunk for clearance.

The crossbeam drive is mounted on the beam as shown in Figure A-3. The motor is mounted near a bearing which holds the drive shaft in place. The gearbelt drive determined the distance between the motor and the drive shaft. A 4:1 drive ratio was selected and the gearbelt drive components were chosen from the Browning catalog. The gearbelt is part number 160XL037 and the two gearbelt pulleys are part numbers 12XLB037 and 48XLB037. The gearbelt drive had to be a minimum of 4.9 in. from centerline to centerline to provide enough teeth between the belt and the pulley to transmit sufficient power to move the beam. The 4.9 in. requirement made it difficult to fit the components below the sensor platform and above the frame.

The sensor platform is mounted on the crossbeam in a similar fashion. The parts for the sensor platform drive are the same as the parts for the crossbeam drive except the pillow blocks are single blocks instead of twin blocks. An end view is given in Figure A-4 and a plan view is given in Figure A-5. Two rails are mounted on a 1/2 in. by 4 in. aluminum plate with a gear rack running down the middle to carry the platform. For drive shaft clearance, the gear rack on the sensor drive requires a 3/8 in. spacer. The drive shaft is held in place by two bearings attached to the sensor platform. The plan called for four pillow blocks to hold the sensor platform on the rails, but only three blocks are used. Aligning both rails and all

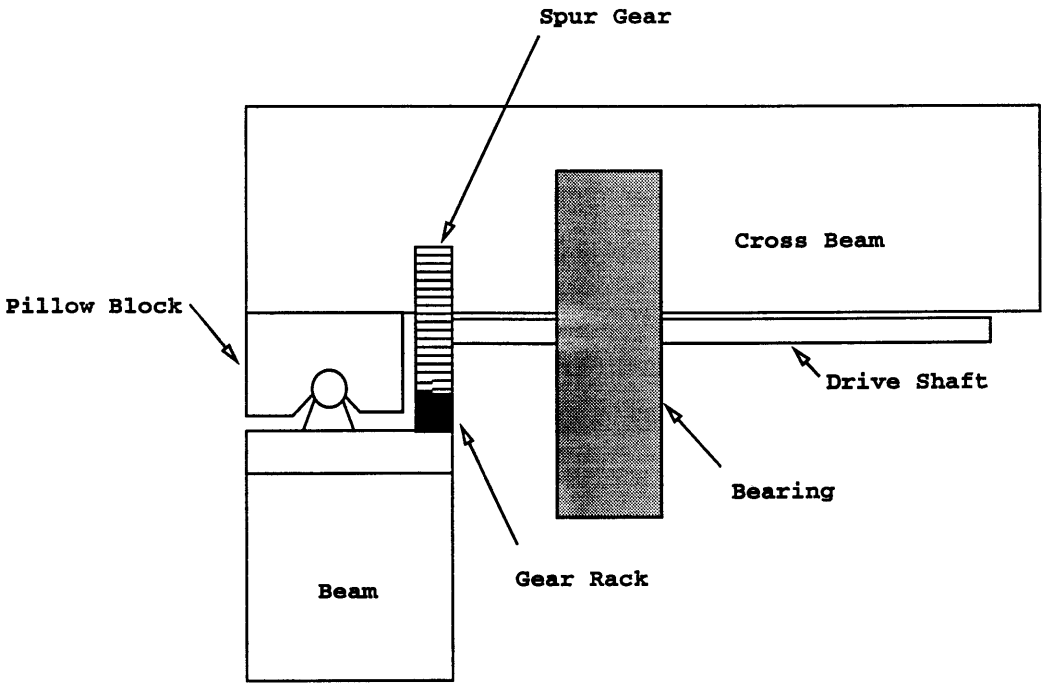


Figure A-1: Side view of crossbeam intersection with plotter frame.

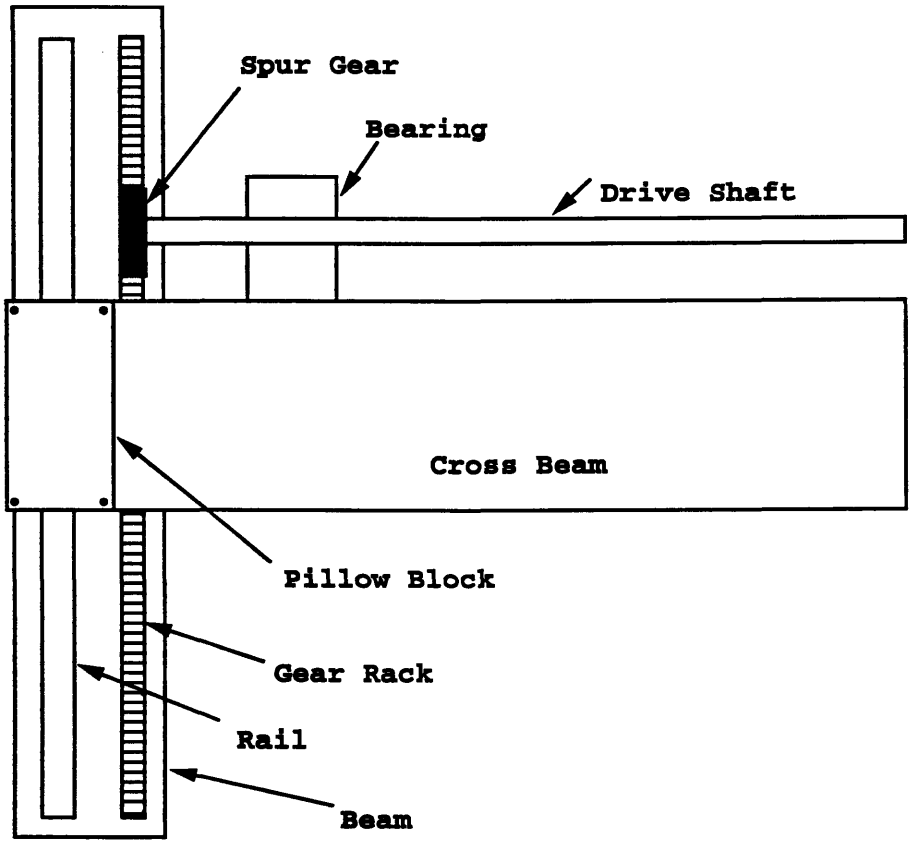


Figure A-2: Plan view of crossbeam intersection with plotter frame.

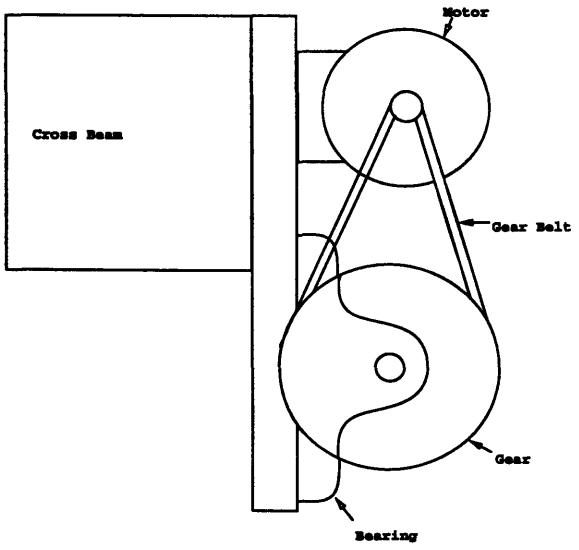


Figure A-3: Detailed view of crossbeam drive.

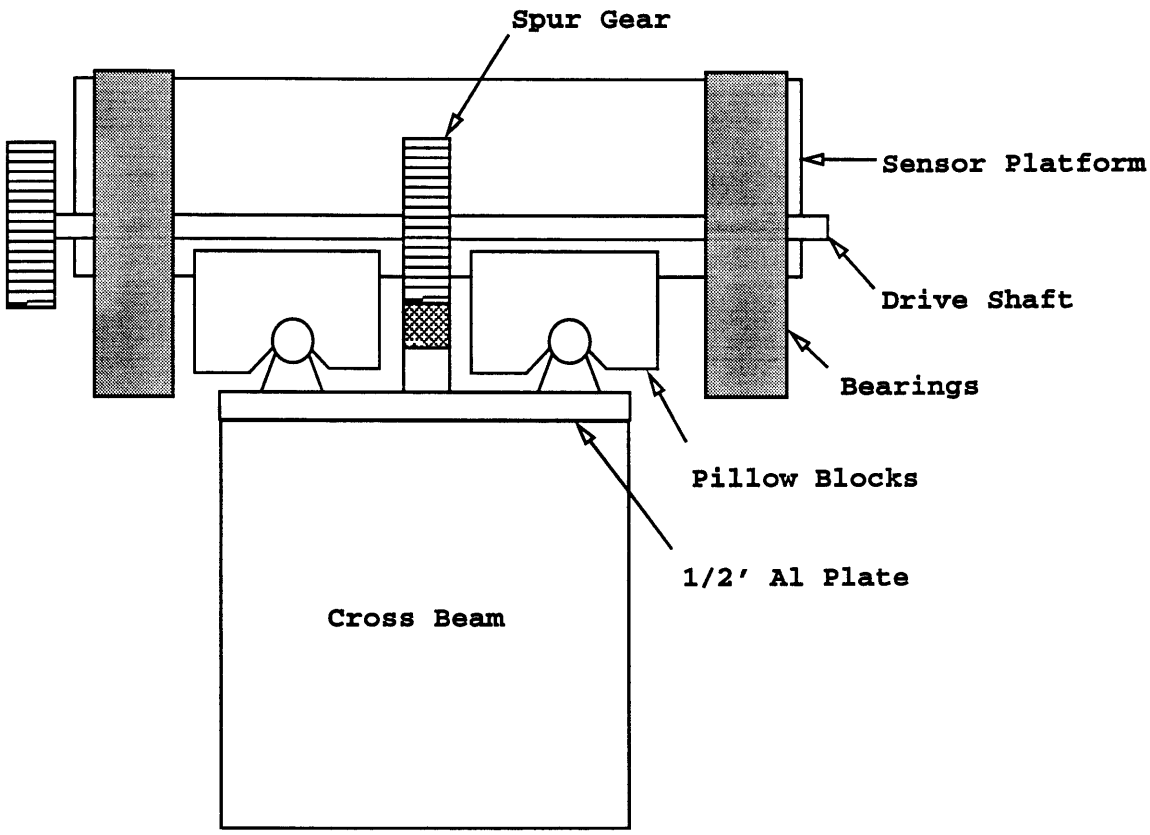


Figure A-4: End view of sensor platform mounted on plotter crossbeam.

four pillow blocks within the running tolerance proved to be nearly impossible. With only three blocks, the alignment tolerance is not quite as small and the platform moves much easier. The motor is mounted onto the sensor platform. The platform is large enough to accommodate a wave gauge or another instrument if needed.

The final touch was to provide the cables needed for the motors and the profiler. A simple system was built to hang the cables so that they would not interfere with the plotter movement. A thin wire is attached between two metal supports. The cables run through links attached to the wire. Since there is approximately 40 m of cable between the plotter and the control room, the cables are shielded. Each motor has a two wire power cable and a six wire cable for the digital encoder feedback. The sensor has a power cable, which is an extension cord, and the analog output, which is a shielded BNC cable. Even with shielded cables, the power cord for the profiler interferes with the power cables for the motors. When

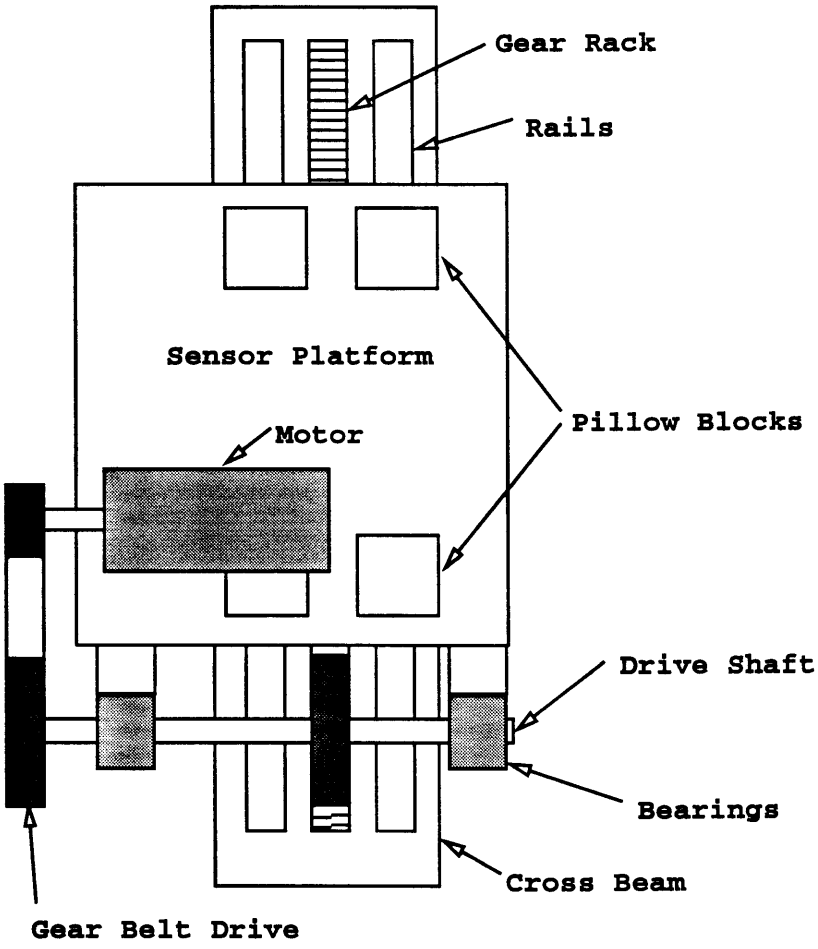


Figure A-5: Plan view of sensor platform.

the motor power cords are in close proximity to the extension cord powering the profiler, the induced noise causes the motors to spin back and forth out of control and corrupts the digital feedback lines. Because of this, the extension cord comes into the sensor platform from the opposite side of the plotter. The power cords for the motors interfere with the signal from the profiler as discussed in Section 3.3, but the added noise can be filtered out by averaging the signal.

# Appendix B

# X-Y Plotter Usage

The X-Y plotter is not very difficult to operate, but there are a lot of components involved. This means that when there is a problem, it can take a while to pinpoint the problem and determine a solution. This appendix is designed to help the user understand the system so it can be maintained and used properly.

## B.1 Programming

The motion controller board came with some software to interface with the DOS and Windows environment as well as the libraries for C, C++ and other programming languages. These are located in the directories C:\COMMDISK and C:\SDK1000 on the Quantex computer in the control room.

The COMMDISK directory contains the DOS commands that we use for beach data acquisition. The command "down2bus" is used to download programs from the computer memory to the motion controller card. The usage is "down2bus <filename>" where <filename> is the name of the file containing the program. Down2bus cannot be used while a program is running. It replaces the program in the controller's memory with the new program. The command to send commands to the motion controller is "send2bus". Its usage is "send2bus THE_STRING <control string>" where the control string could be to turn the motors on, execute a program or ask for the error code. The command to execute a program cannot be used while another program is currently running. The other program that we use is called "blisten" to listen to the output from the motion controller. Without an argument, the data is just sent to the computer screen. To send the output to the file

<datafile>, the usage is "blisten OUTPUT_TO <datafile>".

The board also came with a Galil publication called the "DMC-1000 Technical Reference Guide, Version 1.3" referred to as the reference guide in this text. The reference guide contains wiring diagrams, screw terminal assignments, programming support and programming examples for the motion controller. It is a relatively thorough and helpful book.

The plotter programs are located in the directory COMMDISK directory. The programs written specifically for data collection on the beach are "combo.ttb" for the two beaches without the dividing wall and "test.ttb" for the two beaches with the dividing wall. The programs are downloaded to the motion controller board with a variety of batch files, or files with the format "filename.bat". Batch files execute a sequence of instructions with one command rather than having to type each command each time. The batch files are changed frequently, so one must read through them to determine which files are used for what purpose.

There are three batch files which are very useful to anyone trying to use the plotter. The first is "zero.bat" which runs a small program called "zero.ttb". The purpose of this program is to provide a mechanical zero for the plotter where the counters can be reset to a predetermined and consistent value. This function is executed by typing "zero", manually moving the sensor platform to the corner of the plotter closest to the joystick, and pressing the thumb button on the joystick. The sensor platform has to be pushed to its mechanical limit to insure that it is zeroed consistently. The second useful batch file is "error.bat" which sends the instruction "TC" to the controller. If there is no error, the board will return "000". If there is an error, the returned value indicates what kind of error the board is experiencing. The error codes are listed in the the reference guide under the command reference for "TC". Checking for an error is a good start in locating programming errors. The third useful batch file is "stop.bat" which is used to stop the current program and motion and turn the motors off. The board can only run one program at a time, so the current program has to terminate on its own or be terminated by the stop command before the next program can be run. The stop command is also useful when the plotter is going to cause some damage to itself or to a component mounted on it if it continues on with the current program.

Since the programming commands, or Opcodes, are well documented in the reference guide they will not be covered here. The programs "combo.ttb" and "test.ttb" were written

to run very specific tasks. They may need to be modified to run different tasks. They are not very well commented, but can be deciphered by looking up the commands in the reference guide. The programs are very simple so this should not be difficult.

There is one programming command that is worth mentioning. The command "II" means input interrupt and gives the user a way to interrupt the current program using one of the digital inputs. The programs are set up to use digital input seven as the interrupt channel. Digital input number seven is wired to the index finger or trigger button on the joystick. When this button is pressed, the controller interrupts the current program and jumps to the subroutine #ININT until it reaches the instruction "RI" which means return from the interrupt condition. This special function is added here because it is very difficult to program for every condition that the plotter might experience. One can always stop the program execution while at the computer, but it is difficult to stop it out at the plotter. This routine allows for a "panic button" at the plotter in case the plotter needs to be stopped quickly.

## B.2 Electrical Maintenance

The system is quite complex and requires frequent maintenance. This is not an exhaustive list of problems and solutions, but contains some of the more frequent types of problems encountered using the plotter system.

The components for the plotter system are described briefly in Section 3.2. The motion controller card is in the Quantex computer in a ISA slot. It has a 60 pin ribbon cable and a 26 pin ribbon cable running to the amplifier board.

The amplifier card and the power supply are housed in the "black box", which is the shell of a 15 year old IBM computer. We received the components separately and were supposed to get a black box through Bruce Parks. When this never arrived, we gutted the IBM and installed the components. Inside the black box there are two compartments separated by a metal divider. The divider is a piece of metal foil to shield the board from the power supply. The right side of the black box houses the power supply. A cable coming in from a wall socket via a surge protector provides electricity for the power supply. The power switch for the power supply is the switch on the surge protector. The 24 Volt output from the power supply is connected to the amplifier board and to a small cooling fan. The

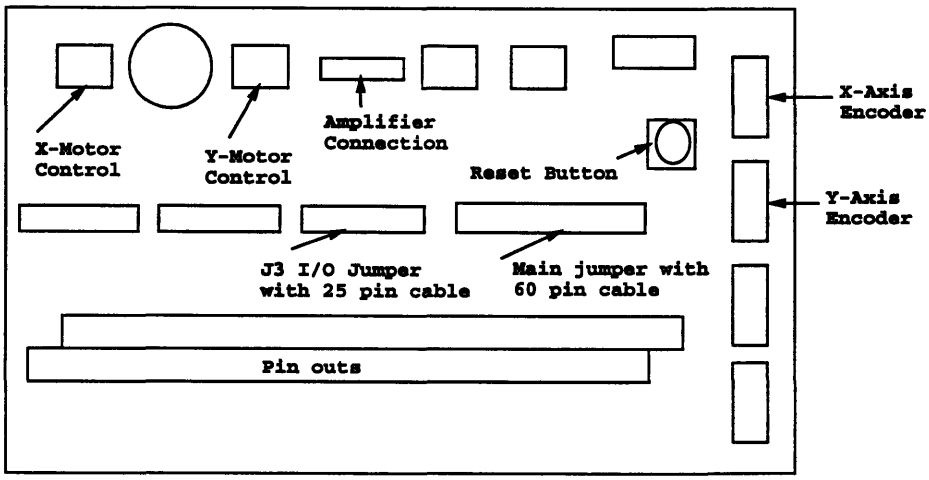


Figure B-1: Wiring diagram for motion controller.

fan only takes 12 Volts so it is connected across a 12 Volt voltage divider. The left side of the black box contains the amplifier card.

The amplifier card has many wires connected to it. A wiring diagram is provided in Figure B-1. The 60 pin ribbon cable is the main cable between the computer and the amplifier. It contains all of the standard communications for the card. The 26 pin ribbon cable is needed for the digital and analog input channels. The power supply cables for the motors are attached near the 24 Volt power supply connection. The digital encoder feedback cables from the motors are the 10 wire ribbon cables connected to the amplifier board. Next to the encoder feedback plugs is the reset button, which is used infrequently. When the board is not responding correctly at all and nothing seems to be working, resetting the board sometimes helps. There is a small hole in the front of the black box labeled "Commdisk reset button" which allows access to the button. The rest of the wires are connected to the screw terminals provided on the amplifier board. Chapter 12.9 in the reference guide provides a brief description of the 104 screw terminals. Most of the terminals we use are for the analog and digital inputs. Table B.1 has the wiring inputs that are being currently used with "AN1" referring to analog input one and "IN1" referring to digital input one. The uncommitted input into channel AN4 is wired to the bottom set of banana plugs on

Table B.1: Analog and digital inputs used on the amplifier card.

| Input number | Usage |
|---|---|
| AN1 | X axis control from joystick |
| AN2 | Y axis control from joystick |
| AN3 | Analog input from profiler |
| AN4 | Uncommitted input |
| IN7 | Trigger button from joystick |
| IN8 | Thumb button from joystick |

the back panel of the black box in case another analog input is needed. Analog inputs five through seven and digital inputs one through six are not being used currently. When gripping the joystick handle, the "thumb button" is the top button, where the thumb rests, and the "trigger button" is the front button where the index finger rests.

If the plotter is not responding, there are a number of problems that could be responsible. If the program is an established and tested program, it may have to be downloaded to the motion controller again. If this does not help, then the board can be reset manually using the reset button described above. To test the motion controller, Galil provided two useful programs. These can be used to test various aspects of the system to pinpoint errors. In most cases, the problem is usually a loose connection in one of the many wires.

The first debugging program is "SDK1000", or the servo design kit for the 1000 series motion controller. This program is located in the SDK1000 directory. It checks the main system elements to insure that they are connected properly. As the program starts, it locates the motion controller card and then has a self explanatory guided tour through the system components. If one of the main components is not wired properly, SDK1000 should discover this quickly. Problems that SDK1000 will uncover include the amplifier not being connected to the controller card, a loose connection in the power supply for the motors, or a loose connection on the digital encoder returns for the motors.

If the problem is not with one of the main components, it may be harder to find. A program called "talk2bus" in the COMMDISK directory is a terminal that allows one to talk to the controller and probe the inputs. The terminator uses the two letter Opcodes used in programming, so it is also a good debugging tool for developing new programs. Usually you will have some idea what is wrong and will be able to focus your analysis, but it is not difficult to check most of the connections using the talk2bus program. If one is

Table B.2: Gain and acceleration values for X-Y plotter.

| Property | Opcode | X axis (platform) | Y axis (beam) |
|---|---|---|---|
| Integral gain | KI | 4 | 1 |
| Proportional gain | KP | 30 | 25 |
| Derivative gain | KD | 300 | 350 |
| Acceleration | AC | 25000 | 20000 |
| Deceleration | DC | 25000 | 20000 |
| Speed | SP | 10000 | 10000 |

uncertain if the problem is electrical or mechanical, then simple move commands can be sent to the controller to see how it responds. The gains and the acceleration values need to be set properly for the system to respond in a controlled manner. If the plotter is not moving smoothly, adjust the gains and acceleration. The values that we have been using are given in Table B.2. They have been determined experimentally using the SDK1000 program and by adjusting the parameters until the plotter ran smoothly.

If the problem is unresolved but electrical, the cover to the black box can be removed. With the cover off, the connections can be checked and the leads tested. We have gotten to this point, opened it up and poked around without determining the error and then had the plotter work normally. Since it is awkward to open up the black box, it is best left as a last resort in trouble shooting. Obviously, if one needs to rewire the inputs, it needs to be opened.

## B.3 Mechanical Maintenance

The plotter requires periodic maintenance to insure that it keeps operating properly. The rails and pillow blocks need an occasional application of light machine oil to keep lubricated and clean. If this does not happen, the pillow blocks will not slide as easily and system performance will decline.

Where the gear racks meet, the gap between the teeth is not the right size, it is a little too long or short. If the spur gear is too low, the teeth catch at this gap and the gear will clank moving over the gap. If the gear is really low, it may even get stuck. If this happens, the spur gear height can be adjusted by moving the bearing next to the spur gear vertically. The spur gear needs to be low enough to engage, but high enough not to get stuck at the

gaps. The frame and the beam are not perfectly square with each other. When the beam is at its mechanical limit, it hits one stop and is about 3 cm from the other. This skewness is structural and cannot really be removed. We unsuccessfully tried removing it several times, with the beam binding during movement and the spur gears skipping teeth in the gear rack due to the excess stress when the beam is straight. The beam is relatively unstressed in the skewed position and resists straightening.

If the motor works, but the crossbeam or platform are not moving, the set screws on the gears may need to be tightened. The set screws that hold the gears on the drive shaft occasionally need to be tightened with an allen wrench.

## B.4 Data Collection

The data collection protocol we used for this experiment is described here. It is given with an emphasis on the procedures; the programs are essentially the same. The steps are as follows:

1. Turn on computer, if not already on.
2. Turn on power supply for the motors. The switch is on the power strip leading to the black box.
3. Measure water depth with a yardstick for a reference elevation.
4. Run the program NC (Norton Commander) and go to the directory C:\COMMDISK\PROGRAMS.
5. Load the sampling program using "down2bus" or a batch file.
6. Zero the plotter if necessary by running the batch file "zero". The message "Ready" says the plotter is ready to be reset. Move the plotter to the corner nearest the joystick and press the thumb button. As a confirmation, the message "Done" will appear on the screen.
7. Prepare the beach for measurement by:
   (a) Clear any debris from the sand or water surface.
   (b) Knock down any vertical scarp that may be present.

(c) Cover the sea wall completely with the white gauze.

(d) Wipe the probe tip to clear it of any water drops.

(e) Move the profiler to the area where it will measure (for the divided beach).

8. Run the measurement program using a batch file to start the program. Once the program is initiated, follow these steps:

   (a) Set the probe in its sleeve at the lower measuring position with the correct orientation, turn the profiler on with the switch built into the cord and engage the profiler's servo motor.

   (b) Press the thumb button on the joystick to measure the water surface and begin sampling.

   (c) The probe scans the above water profile first. As it passes out over the water, press the thumb button at the second or third measurement pause to turn the probe around to measure the next transect.

   (d) When the profiler returns to the reference position, turn the profiler off, adjust the probe to the upper position, turn the profiler on and engage the servo motor so that the probe is measuring the water surface. Press the thumb button once to take a measurement, splash water on the probe tip so the probe goes under water and press the thumb button again to start the measurement.

   (e) While the probe is underwater, make sure that it does not pop out of the water when it comes close to the waterline. If it does, stop the plotter with the trigger button, splash the probe to get it to reenter the water and press the thumb button to re-engage the sampling program.

   (f) Note: the trigger button is a "panic button" allowing the user to stop the plotter at any point during the measurement program. The thumb button returns the plotter to where it was in the program.

9. The data is stored in a temporary file called data.plt by the command "blisten OUTPUT_TO data.plt". Rename this file and store it in a data directory.

4271-71